Time-Frequency Analysis of Lamb Waves using the Morlet Wavelet Transform

by

Karen Paula L. Veroy

Bachelor of Science in Physics
Ateneo de Manila University (1996)

Submitted to the Department of Civil and Environmental Engineering
in partial fulfillment of the requirements for the degree of

Master of Science in Civil and Environmental Engineering

at the

MASSACHUSETTS INSTITUTE OF TECHNOLOGY

February 2000

Author .....
Department of Civil and Environmental Engineering
January 2000

Certified by .....
Shi-Chang Wooh
Associate Professor of Civil and Environmental Engineering
Thesis Supervisor

Accepted by .....
Daniele Veneziano
Chairman, Departmental Committee on Graduate Studies

Time-Frequency Analysis of Lamb Waves using the Morlet Wavelet Transform

by

Karen Paula L. Veroy

Submitted to the Department of Civil and Environmental Engineering
on January 2000, in partial fulfillment of the
requirements for the degree of
Master of Science in Civil and Environmental Engineering

Abstract

The focus of this work is the time-frequency analysis of multimode Rayleigh-Lamb wave signals for nondestructive evaluation. Dispersion curves are extracted from a single broadband signal containing several modes using the Morlet wavelet transform. The method is applied to simulated as well as experimental signals. An Nd:YAG laser and PVDF transducers were used to generate and receive the Rayleigh-Lamb wave signals on an aluminium plate. Direct arrivals and reflections from the edge of the plate, although obscure in the time domain, were easily distinguishable in the time-frequency domain. Results show that within a limited frequency range the time of flight of the direct arrivals and edge reflections may be extracted with good accuracy. The extracted information may then be used to determine the location of the edge of the plate. This work suggests that with the aid of time-frequency analysis, the presence of several modes in a Rayleigh-Lamb wave signal need not be considered detrimental to nondestructive evaluation. It may, on the contrary, provide a means of detecting discontinuities in the specimen.

Thesis Supervisor: Shi-Chang Wooh
Title: Associate Professor of Civil and Environmental Engineering

Acknowledgments

Graduating from MIT is a huge achievement for me, one that would have been impossible without the help and support of so many people.

First and foremost, I offer my love and gratitude to my whole family. I will be eternally grateful to my parents, Bing and Renette. All of my achievements have their roots in the love and support they gave me through all of my life. This work is lovingly dedicated to them. I thank my Ate Lizza, who taught me to stand up for myself; my Kuya Butch, for giving me that much needed job, and my Kuya Bing, for letting me follow him around when I was a kid and never telling me to bug off. I thank Yaya Andring for her patience and devotion in taking care of me and my family all these years, and for all the *ampaw* and Nik Nok comic books she bought for me many years ago. I thank the ever efficient Yaya Ellen, who took care of all the little details, and for those much-needed massages in college. Finally, to the littlest members of my family, Chesca, Nicco, and little Iya for the immeasureable happiness that they give us.

My humblest thanks to my advisor, Prof. Shi-Chang Wooh, for giving me the opportunity to work on this project. Needless to say this work would never have been completed were it not for the invaluable guidance and support he provided.

Next, I must thank those people who played special roles in getting me to MIT: Prof. Reynaldo Vea, for his trust and confidence in me; and Prof. Estrella Alabastro, who made sure I and my fellow scholars are well taken care of. I greatly appreciate the support given me by my sponsors: the Department of Science and Technology and the University of the Philippines. Many thanks to the officers and staff of these institutions for their continued support to Filipino scholars.

I am also indebted to the many individuals who contributed greatly towards the completion of this work: Prof. Kevin Amaratunga and Prof. Gilbert Strang, whose class on wavelets became the impetus of this project; and my colleagues in the NDE Laboratory especially Yijun Shi, Jiyong Wang and Quanlin Zhou.

Next I must thank some special people who helped me keep my sanity and made 1-050 a home away from home: Daniel Dreyer, Sung-June Kim, Joonsang Park, Monica Starnes, Jens Haecker, Satoshi Suzuki, Louie Locsin, Dominic Assimaki and Mike Cusack. I thank many other friends among the faculty, staff, and students in MIT, especially in the CEE

Department. I also thank other friends in Boston and in the Philippines for their support.

Und schliesslich, Dir Martin, all meine Liebe.

Contents

List of Figures

List of Tables

Chapter 1

Introduction

1.1 Problem Statement

The merits of Lamb wave testing for the nondestructive evaluation (NDE) of plates have been reiterated in the many works published on the subject. For instance, the advantages of Lamb wave testing over conventional C-scanning have often been emphasized. When large areas of a structure are to be inspected, Lamb waves are more attractive than bulk waves since they can propagate over long distances to inspect a wider area [1].

It is a great misfortune, then, most authors lament, that Lamb waves are multimode by nature. That is, there exist at least two wave modes at any given frequency, thus making the signals complicated and difficult to interpret.

In general, there are two approaches taken to address this unfavorable circumstance. The first deals with it at the experimental level by coaxing a single mode into dominance (see for instance Alleyne and Cawley (1992) [2]). The other less established approach accepts the multimode nature of the signal and treats it at the signal analysis level [3, 4, 5]. It is the latter that is explored in this study.

Among the many methods in signal processing, time-frequency analysis lends itself quite naturally to the analysis of multimode, broadband signals. In the analysis of dispersion, the wavelet transform seems to be an excellent alternative to other more conventional methods such as the short-time Fourier transform [3, 6, 7]. Due to its similarity to the STFT, the Morlet wavelet in particular serves as a gateway towards the use of wavelets in this area.

Thus, the problem addressed in this study is this: To use the Morlet wavelet transform to extract the Lamb wave dispersion characteristics from a multimode, broadband signal

for the purposes of nondestructive evaluation.

1.2 Historical Perspective

The formal solution to the problem of two-dimensional waves in a solid bounded by parallel planes was first given by Rayleigh (1889) and Lamb (1889) [8]. It was only in the 1960s, however, that Mindlin [9] and other authors achieved a fuller understanding of the implications of the frequency equation. The physical aspects and applications of the theory was discussed in 1967 by Viktorov [10] in his classic text.

1.2.1 Lamb waves for NDE

Since then, many developments to the theory and application of Rayleigh-Lamb waves – or simply Lamb waves – have been achieved. One notable development was the discovery of leaky Lamb waves which have since been studied extensively by Bar-Cohen, Mal, *et al.* [11, 12, 13, 14, 15], and Chimenti, *et al.* [16, 17, 18] and used for the NDE of cohesive bonds, composite laminates and bonded plates.

Many authors have also applied the more classical Lamb waves towards the NDE of materials and structures. For instance, Guo and Cawley [19, 20, 21] investigated the interaction of Lamb waves with delaminations in composite laminates . Castaings and Cawley explored the use of air coupled transducers in generating a single Lamb mode and used to method to detect defects [22]. Rogers determined elastic constants of isotropic plates from measurements of phase velocities of individual modes [23].

1.2.2 Experimental Approach

Most authors have directed their efforts towards developing techniques to generate a single Lamb mode over a controlled frequency bandwidth. Alleyne and Cawley have published extensively on the subject and provided an excellent review of possible methods of excitation, response measurement and signal processing, as well as guidelines for the selection of the appropriate mode and frequency range for different inspection requirements [2, 24, 25].

A common thread in all these studies is the use of angle-wedge transducers and narrowband signals in order to transmit and receive a pre-determined Lamb mode at a given frequency. In theory, a particular incident angle will generate only Lamb waves having

the corresponding phase velocity determined by Snell's law [10, 26]. In practice, however, single-mode excitation is hampered by finite transducer width and beam divergence which cause a finite range of frequencies and phase velocities to be excited [23]. This method also requires sweeping in frequency or scanning in space in order to construct significant sections of the Lamb wave dispersion curves.

The experimental setups often require great accuracy in alignment and, when scanning in space, maintaining this accuracy in all tests. Nevertheless, this method remains attractive due to the ease with which the received signals may be interpreted.

The use of array transducers has been explored as an alternative to angle-wedge transducers in single Lamb mode excitation [10]. Rose et al. [27, 28] has explored the use of comb transducers for NDE and smart structures. Monkhouse et al. [1], for instance, developed flexible interdigital transducers to be imbedded in the structure designed to excite a particular mode. Perhaps an even better alternative, and one that is still being explored, is the use of array transducers capable of dynamically tuning to a preferred mode without realigning the transducer configurations [29, 30].

1.2.3 Signal Analysis Approach

Another approach addresses the multimode nature of Lamb wave signals at the signal processing stage. In exchange for greater ease in experimental implementation, broadband, multimode signals are tolerated at the expense of an increase in computation.

Pierce et al. [31] analyzed broadband Lamb wave signals in aluminum and composite samples. They used the two-dimensional Fourier transform [32] on a set of waveforms obtained using non-contacting laser generation and reception. Although they successfully extracted dispersion curves by this method, one drawback in using the two dimensional Fourier transform is that it still requires the acquisition of several signals at different locations.

Time frequency analysis methods, on the other hand, lend themselves quite naturally to the analysis of dispersed waves by simultaneously analyzing the temporal and spectral characteristics of signals. The advantage of time-frequency analysis over the two dimensional Fourier transform is that the dispersion curves may in theory be extracted from a single signal, as opposed to several signals.

One such scheme that has received quite a bit of attention is the wavelet transform.

Inoue *et al.* [7] performed a wavelet analysis of broadband albeit single-mode flexural waves in beams. Abbate *et al.* [3, 6] describe how the wavelet transform may be used in analyzing Lamb wave signals, but lacked more extensive results. Veroy and Wooh [4, 5] performed numerical simulations in which the wavelet transform was used to construct two-mode dispersion curves from a single signal.

1.3 Scope and Limitations

The goal of this study is to extract the Lamb wave dispersion characteristics from broadband multimode signals using the wavelet transform. To achieve this, both numerical and experimental investigations are performed.

1.3.1 Numerical Investigation

The feasibility of the method is first evaluated through a numerical investigation. Broadband signals are simulated and the entire frequency spectrum (from near zero to the Nyquist frequency) is analyzed. Both single-mode and multimode signals are used in the numerical tests. The results of this investigation is an algorithm capable of extracting group delay from a multimode signal.

1.3.2 Experimental Verification

This algorithm is then applied to real Lamb wave signals. Broadband signals were obtained using an Nd:YAG laser and polyvinylidene fluoride (PVDF) transducers to excite and detect the Lamb waves in aluminum plates. The results are then analyzed and the algorithm evaluated.

1.3.3 Limitations

The subject of wavelets is a broad and rapidly developing field. There are many different wavelets, but only the Morlet wavelet is used and evaluated in this study. A survey and evaluation of other wavelets is beyond the scope of this thesis.

The experimental investigation is also limited to one aluminum plate sample. Future studies will most certainly involve plates of other thicknesses and materials, and containing different types of defects.

The ultimate goal is to develop a method for the characterization of defects, i.e., to determine the location, size, nature and orientation of the defect. Although much has yet to be done in order to achieve this goal, the method described in this study will be shown capable of detecting a discontinuity in the form of an edge on the plate. Other types of discontinuities are not investigated in this thesis.

1.4 Thesis Organization

Chapters 2 and 3 give a brief review of the principles of dispersion, Lamb waves and time frequency analysis using wavelets. Far from being complete treatises, these chapters were intended to highlight the main ideas essential in the different aspects of the study.

The numerical investigation is discussed in Chapter 4. The implementation of the method, and its application to simulated single mode and multimode signals are discussed.

Chapter 5 describes in detail the experimental set-up used and analyzes the results of the experiments. A summary of the main points of the thesis and an evaluation of the method follow in Chapter 6.

The appendix contains supporting data and calculations as well as a more complete list of specifications of the equipment used.

Chapter 2

Dispersive Systems: Rayleigh-Lamb Waves

2.1 Introduction

This chapter is divided into three major sections. The first gives a brief explanation of the phenomenon of dispersion, and the concepts of phase and group velocity are defined. The second section deals with the characterization of dispersive systems in general. In particular, the relationship between the phase response of a system and dispersion is explained. The last section deals with Rayleigh-Lamb waves.

2.2 Dispersion

The phenomenon of dispersion was observed and investigated as early as the mid-1800's. A simple analytical explanation for the phenomenon, first given by Stokes, begins by considering two propagating harmonic waves with equal amplitude but different angular frequencies ω_1 and ω_2

$$u(x,t) = A[e^{i(k_1 x - \omega_1 t)} + e^{i(k_2 x - \omega_2 t)}] \tag{2.1}$$

where k_1 and k_2 are the wavenumbers and $i = \sqrt{(-1)}$. Assume further that ω_1 and ω_2 are only slightly different, and let

$$\omega = \frac{1}{2}(\omega_1 + \omega 2) \qquad k = \frac{1}{2}(k_1 + k_2) \tag{2.2}$$

$$\Delta\omega = \frac{1}{2}(\omega_1 - \omega 2) \qquad \Delta k = \frac{1}{2}(k_1 - k_2) \tag{2.3}$$

Eqn. (2.1) may then be written as

$$u(x,t) = 2A\cos(\Delta kx - \Delta\omega t)e^{i(kx-\omega t)} \tag{2.4}$$

As shown in Fig. 2-1, the low frequency term envelopes the high frequency signal, thus forming a succession of wave groups. The high frequency term in Eqn. (2.4) propagates at the average velocity c where

$$c = \frac{\omega}{k}\cdot \tag{2.5}$$

Since c is the velocity at which a point of constant phase propagates, it is called the *phase velocity*. The overall wave group defined by the envelope propagates at the *group velocity* c_g given by

$$c_g = \frac{\Delta\omega}{\Delta k}\cdot \tag{2.6}$$

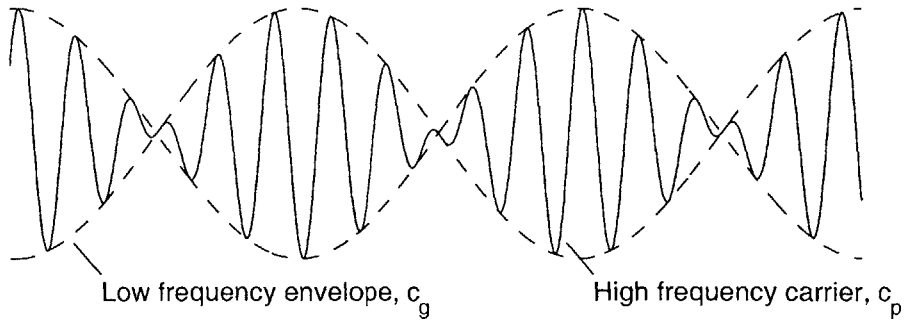

Figure 2-1: A wave group formed by two harmonic waves with slightly varying angular frequencies.

In the limit as $\Delta k \to 0$, the group velocity takes the form

$$c_g = \frac{d\omega}{dk}. \tag{2.7}$$

2.3 Characterization of Dispersive Systems

2.3.1 Characterization in the Time Domain

A linear time-invariant system, schematically depicted in Fig. 2-2, can be fully characterized in the time domain by its impulse response $h(t)$ through the convolution sum

$$g(t) = f(t) * h(t) = \int_{-\infty}^{\infty} f(t)h(t' - t)dt' \tag{2.8}$$

where $g(t)$ is the output due to a given input $f(t)$. The impulse response is the response of the system when the input is a Dirac delta function, $\delta(t)$.

2.3.2 Characterization in the Frequency Domain

The system may likewise be completely characterized in the frequency domain by the frequency response or transfer function, as depicted in Fig. 2-3. The frequency response is defined as the complex gain that the system applies when the input is a complex exponential [33]. That is, if $f(t) = e^{i\omega t}$, then

$$g(t) = H(\omega)e^{i\omega t} \tag{2.9}$$

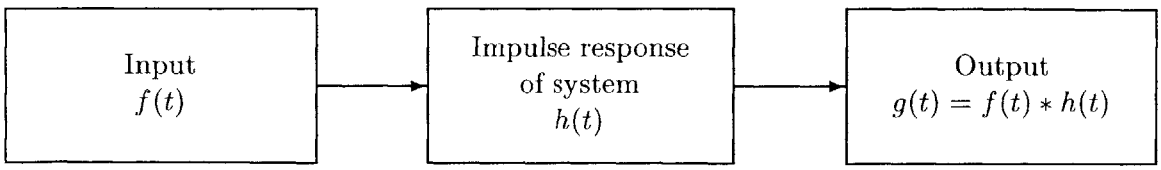

Figure 2-2: Time-domain characterization of a linear time-invariant system.

where

$$H(\omega) = \int_{-\infty}^{\infty} h(t)e^{-i\omega t}dt. \tag{2.10}$$

is the transfer function. If the input is a Dirac delta function,

$$f(t) = \frac{1}{2\pi}\int_{-\infty}^{\infty} e^{i\omega t}d\omega = \delta(t), \tag{2.11}$$

then by superposition and by the definition of the impulse response,

$$h(t) = g(t) = \frac{1}{2\pi}\int_{-\infty}^{\infty} H(\omega)e^{i\omega t}d\omega. \tag{2.12}$$

The Fourier transforms of the input and output, $F(\omega)$ and $G(\omega)$ respectively, are then related by

$$G(\omega) = H(\omega)F(\omega). \tag{2.13}$$

The frequency response may also be expressed in polar form

$$H(\omega) = |H(\omega)|e^{i\phi(\omega)} \tag{2.14}$$

where $|H(\omega)|$ is the *magnitude response*, and $\phi(\omega)$ is the *phase response* of the system. The magnitude response is a measure of the amplification or attenuation introduced by the system as a function of the input frequency. The phase response is a measure of the phase shift that the system applies to an input of frequency ω. The effect of the phase response may be better understood by considering the concept of *group delay.*

2.3.3 Group Delay

The group delay $\tau(\omega)$ is defined as the negative of the slope of the phase response [33]

$$\tau(\omega) = -\frac{d\phi}{d\omega}. \tag{2.15}$$

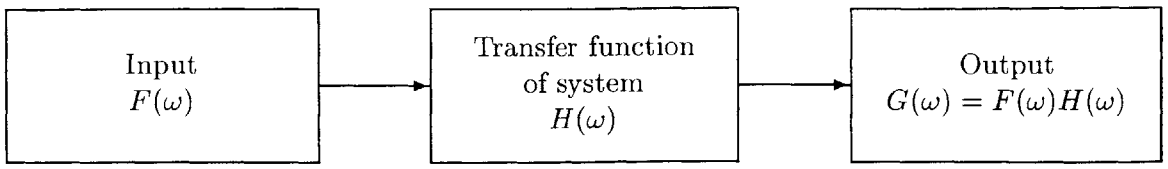

Figure 2-3: Frequency domain characterization of a linear time-invariant system.

To illustrate the effects of group delay on the response of a system, we consider a system with frequency response

$$H(\omega) = e^{i\phi(\omega)}. \tag{2.16}$$

This system introduces no attenuation or amplification; its only effect is a phase shift ϕ. We consider two cases. First, ϕ is linear in ω; and second, ϕ is nonlinear and the input $f(t)$ is narrowband.

Linear Phase

If ϕ is a linear function of ω

$$\phi(\omega) = \phi_o - t_o\omega \tag{2.17}$$

where t_o and ϕ_o are constants, the group delay is given by

$$\tau(\omega) = -\frac{d}{d\omega}(\phi_o - t_o\omega) = t_o. \tag{2.18}$$

For an arbitrary input $f(t)$ with the Fourier transform $F(\omega)$, the Fourier transform of the output is given by

$$G(\omega) = F(\omega)e^{i(\phi_o - \omega t_o)}. \tag{2.19}$$

Taking the inverse Fourier transform

$$g(t) = e^{i\phi_o}\left[\frac{1}{2\pi}\int_{-\infty}^{\infty} F(\omega)e^{i\omega(t-t_o)}d\omega\right] \tag{2.20}$$

which reduces to

$$g(t) = f(t-t_o)e^{i\phi_o}. \tag{2.21}$$

Therefore, a linear phase response given by Eqn. (2.17) causes a constant phase shift ϕ_o and delays the input by t_o. The constant group delay therefore leaves the input undistorted and only shifts it in time.

Nonlinear Phase

Next, we consider a system with frequency response still given by Eqn. (2.16), but with arbitrary nonlinear phase ϕ. We examine its effects on a narrowband input given by

$$f(t) = s(t)e^{i\omega_o t}. \tag{2.22}$$

For instance, Fig. 2-4(a) shows the time characteristics of an oscillatory signal of frequency ω_o within a finite duration wave packet $s(t)$. The frequency spectrum of this pulse, shown in Fig. 2-4(b), has a sharp peak at ω_o. Since the Fourier transform $F(\omega)$ is nonzero only in the vicinity of $\omega = \omega_o$, we are led to consider the Taylor expansion of ϕ around ω_o

$$\phi(\omega) = \phi(\omega_o) + (\omega-\omega_o)\left[\frac{d\phi}{d\omega}\right]_{\omega_o} + \cdots \tag{2.23}$$

By dropping higher order terms and using Eqn. (2.15), the effect of the phase of the system can then be approximated by

$$\phi(\omega) \approx \phi_o - (\omega-\omega_o)\tau_o \tag{2.24}$$

where $\tau_o = \tau(\omega_o)$, $\phi_o = \phi(\omega_o)$. Henceforth, the symbol ζ_o will be used to symbolize the function $\zeta(\omega)$ evaluated at $\omega = \omega_o$.

With this linear approximation, the Fourier transform of the response is

$$G(\omega) \approx F(\omega)e^{i(\phi_o+\omega_o\tau_o-\omega\tau_o)}, \tag{2.25}$$

and the inverse Fourier transform can be expressed as

$$g(t) \approx e^{i(\phi_o+\omega_o\tau_o)}\left[\frac{1}{2\pi}\int_{-\infty}^{\infty} F(\omega)e^{i\omega(t-\tau_o)}d\omega\right] \tag{2.26}$$

which yields

$$g(t) \approx s(t-\tau_o)e^{i(\phi_o+\omega_o t)}. \tag{2.27}$$

Therefore, the effect of the nonlinear phase ϕ on the narrowband signal with center frequency ω_o may be approximated as a constant phase shift $\phi(\omega_o)$ on the oscillatory signal and a delay of $\tau(\omega_o)$ on the envelope.

If we therefore consider an arbitrary signal $f(t)$ as a superposition of narrowband components, then the effect of the system $H(\omega) = e^{i\phi(\omega)}$ on each component centered at ω_o may be approximated in a similar manner. In the case of broadband signals, a nonlinear phase response introduces a group delay that is not constant but may vary significantly with ω. Since each narrowband component is delayed by a different amount, the nonlinearity of the phase causes the signal to be distorted. Components which were in phase initially may no longer be in phase at a later time. The group delay may then also be considered a measure of the distortion or dispersion introduced by the system.

At this point, it may already be clear that the concepts of phase and group velocity are intimately related to those of phase response and group delay respectively. This relationship is explained in greater detail in the next section.

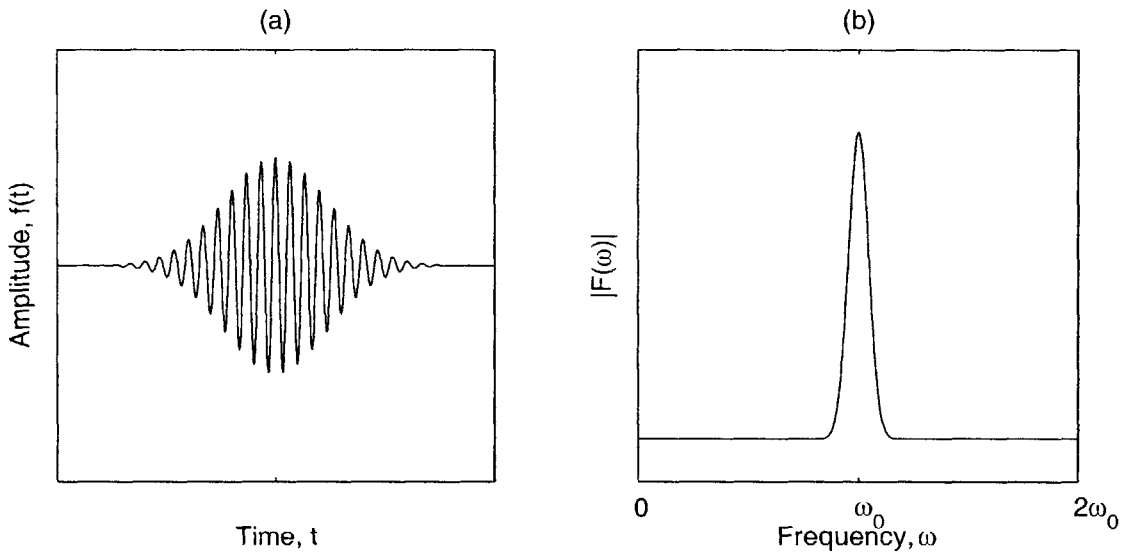

Figure 2-4: (a) A narrowband signal and (b) its corresponding frequency spectrum.

2.4 Wave Motion: Dispersive Systems

The dynamics of wave motion in a physical system may be described in terms of its elements:

- **the problem** - the physical system as described by the governing equation and boundary conditions
- **the forcing function** - the input or forcing applied to the system
- **the solution** - the output or response of the system.

When the system is homogeneous, i.e., when there is no input or forcing applied, the solution corresponds to the free vibration response of the physical system.

In the case of homogeneous 1-D problems, we often seek solutions corresponding to harmonic waves

$$g(x,t) = Ae^{i(\omega t - kx)} \tag{2.28}$$

where A is a constant. These solutions must satisfy the governing equations as well as the boundary conditions. Considering such solutions generally yields an equation of the form

$$f(k,\omega)Ae^{i(\omega t - kx)} = 0 \tag{2.29}$$

which requires that

$$f(k,\omega) = 0 \tag{2.30}$$

for $g(x,t)$ to be nontrivial [34]. This implies that harmonic waves may propagate only when k and ω satisfy the characteristic equation. The correspondence between wavenumber and frequency is also called the *dispersion relation.* Hence, the dispersion relation is a characteristic of the system which stems from either the governing equation or the boundary conditions (or both).

Forced Wave Motion

Considering inputs of the form $x(t) = e^{i\omega t}$, solutions corresponding to propagating waves would then be of the form

$$g(t) = A(\omega)e^{i(\omega t - kx)} \tag{2.31}$$

where k and ω satisfy the dispersion relationship. The frequency response of the system is then

$$H(\omega) = A(\omega)e^{-ikx}. \tag{2.32}$$

The phase response of the system is therefore

$$\phi(\omega) = -kx. \tag{2.33}$$

We consider once again a narrowband input of the form given by Eqn. (2.22). As in the previous section, we approximate the effects of Eqn. (2.32) by expanding $A(\omega)$ and $\phi(\omega)$ around ω_o as follows

$$A(\omega) \approx A_o \tag{2.34}$$

$$\phi(\omega) \approx -x\left\{k_o + (\omega - \omega_o)\left[\frac{dk}{d\omega}\right]_{\omega_o}\right\}. \tag{2.35}$$

The output is then

$$g(t) \approx s\left(t - \frac{x}{c_{g0}}\right)e^{i\omega_o(t - x/c_o)} \tag{2.36}$$

where

$$c_o = \frac{\omega_o}{k_o}, \qquad c_{g0} = \left[\frac{d\omega}{dk}\right]_{\omega_o}. \tag{2.37}$$

Hence, the wave packet travels at velocity c_{g0}, while the high frequency carrier travels within the envelope $s(t)$ at the phase velocity, c_o. The group delay is then simply the time of flight of a wave which traveled a distance x at velocity c_{g0}. The constant phase shift of

the oscillatory signal is similarly related to the phase velocity of the wave.

Multimode Dispersion

Furthermore, it is possible that the relationship between wavenumber and frequency as determined by the characteristic equation (Eqn. (2.30)) is not unique. That is, at a particular frequency ω, there may exist several admissible values of k (or vice versa). The system then supports more than one mode of propagation, where each mode is associated with a dispersion relationship $k_n(\omega)$. Since the system is assumed to be linear, then the frequency response is simply

$$H(\omega) = \sum_n H_n(\omega) \tag{2.38}$$

where $H_n(\omega)$ is the frequency response corresponding to the n^{th} mode and is given by

$$H_n(\omega) = A_n(\omega)e^{-ik_n x}. \tag{2.39}$$

The frequency response of the output, $G(\omega)$, may then be written as

$$G(\omega) = F(\omega)\sum_n H_n(\omega). \tag{2.40}$$

Expanding each term in the same manner as in Eqn. (2.35), the output is then

$$g(t) = \sum_n A_{no} s\left(t - \frac{x}{c_{gno}}\right) e^{-i\omega_o(t-x/c_{no})}. \tag{2.41}$$

Hence, the cumulative effect of multimode dispersion is simply the superposition of each of the modal responses of the system. This is shown schematically in Fig. 2-5.

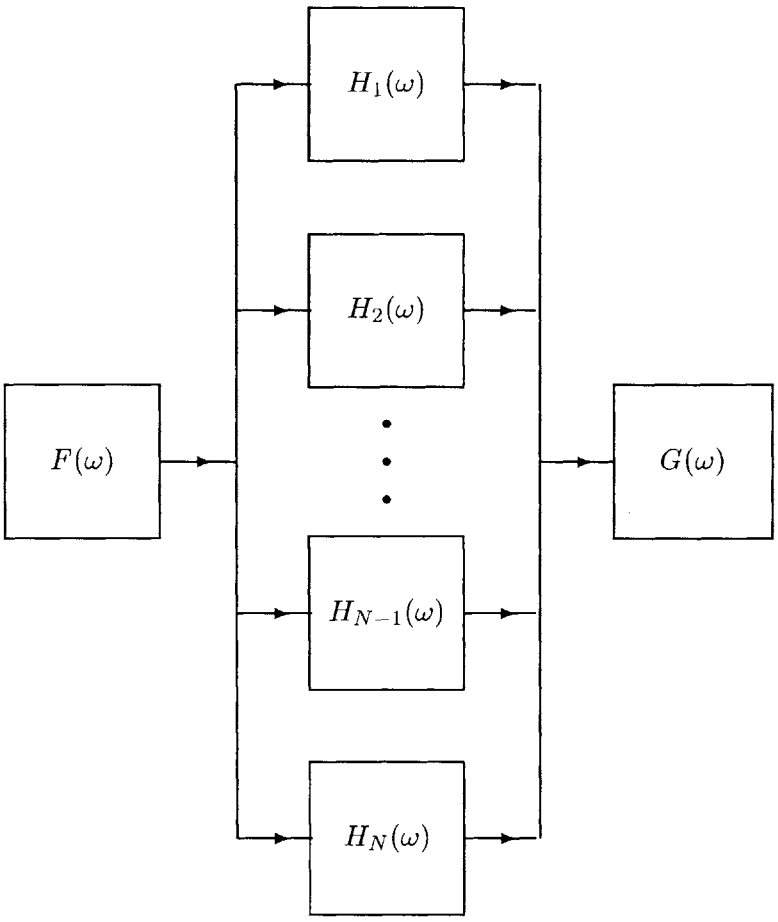

Figure 2-5: Response of a multimode system.

2.5 Rayleigh-Lamb Waves

In this study, we consider in particular the case of waves in a plate having traction-free boundaries, known as *Rayleigh-Lamb waves.* Referring to the coordinate system shown in Fig. 2-6, Rayleigh-Lamb waves propagate in the x-direction and result from multiple reflections of P and SV waves from the boundaries. A comprehensive discussion may be found in the classic text by Graff [8]. The main aspects of the problem and results are briefly outlined here. We define

$$\begin{aligned} u_x, u_y &= \text{displacement in the } x \text{ and } y\text{-direction} \\ c_L &= \text{longitudinal wave velocity} \\ c_T &= \text{transverse wave velocity} \\ k &= x\text{-direction wavenumber} \\ h &= \text{plate thickness} \end{aligned}$$

The frequency, ω, and wavenumber, k, satisfy

$$\omega = kc. \tag{2.42}$$

The vertical and horizontal wavenumbers satisfy

$$\alpha^2 = \frac{\omega^2}{c_L^2} - k^2 \tag{2.43}$$

$$\beta^2 = \frac{\omega^2}{c_T^2} - k^2. \tag{2.44}$$

Considering symmetric solutions of the form [8]

$$u_x = i(Bk\cos\alpha y + C\beta\cos\beta y)e^{i(kx-\omega t)} \tag{2.45}$$

$$u_y = (-B\alpha\sin\alpha y + Ck\sin\beta y)e^{i(kx-\omega t)} \tag{2.46}$$

and applying the boundary conditions on the corresponding stresses leads to the characteristic equation

$$\frac{\tan \beta h}{\tan \alpha h} = -\frac{4\alpha\beta k^2}{(k^2-\beta^2)^2}\,. \tag{2.47}$$

This is the dispersion relation for symmetric modes. Similarly, considering antisymmetric solutions of the form

$$u_x = i(Ak\cos\alpha y - D\beta\cos\beta y)e^{i(kx-\omega t)} \tag{2.48}$$

$$u_y = (A\alpha\sin\alpha y + Dk\sin\beta y)e^{i(kx-\omega t)} \tag{2.49}$$

and applying the stress-free boundary conditions yields

$$\frac{\tan \beta h}{\tan \alpha h} = -\frac{(k^2-\beta^2)^2}{4\alpha\beta k^2}\,. \tag{2.50}$$

This is the dispersion relation for antisymmetric modes.

The dispersion relations (Eqn. (2.47) and (2.50)) may also be written as

$$(k^2-\beta^2)^2\cos\alpha\frac{h}{2}\sin\beta\frac{h}{2} + 4k^2\alpha\beta\sin\alpha\frac{h}{2}\cos\beta\frac{h}{2} = 0 \tag{2.51}$$

$$(k^2-\beta^2)^2\sin\alpha\frac{h}{2}\cos\beta\frac{h}{2} + 4k^2\alpha\beta\cos\alpha\frac{h}{2}\sin\beta\frac{h}{2} = 0 \tag{2.52}$$

for symmetric and antisymmetric modes respectively. These alternative forms of the dispersion relation are better suited to numerical computation [23]. The dispersion curves for aluminum with Poisson's ratio $\nu = 0.35$ and Young's modulus $E = 70$ GPa are shown in Fig. 2-7.

The phase velocity curves were calculated using a root finding algorithm developed in the 1960s by Van Wijngaarden, Dekker et al. and improved by Brent [35]. This method requires an initial estimate of the root. For the fundamental symmetric and antisymmetric modes, S_o and A_o, initial estimates are obtained using the limiting values of the phase velocities for very low frequencies. At low frequencies, the phase velocity of the S_o mode is

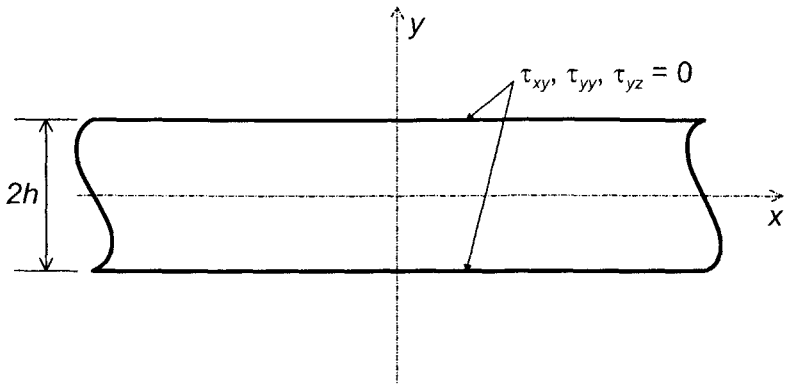

Figure 2-6: Plate of thickness $2h$ with traction free boundaries.

given by [23]

$$\lim_{fh\to 0} c_s = \sqrt{\frac{E}{\rho(1-\nu^2)}} \tag{2.53}$$

while the phase velocity of the A_o mode is

$$\lim_{fh\to 0} c_a = \sqrt[4]{\frac{E}{3\rho(1-\nu^2)}} \quad \sqrt{\omega d}. \tag{2.54}$$

Using these values as initial estimates, the phase velocities at a frequency slightly $\Delta(fh)$ greater than zero are calculated. Successive roots are calculated using previous roots as initial approximations. For instance, after using Brent's algorithm to calculate the phase velocity $c[1]$ where

$$c[n] = c(n\Delta(fh)) \tag{2.55}$$

$c[2]$ is obtained using $c[1]$ as the initial estimate. Generally, the root at c[n] is determined by using the previously calculated root $c[n-1]$ as the initial approximation.

For the higher modes, a less elegant method was used to obtain the initial estimates. First, the frequency-thickness product fh at which the phase velocity is approximately 10 km/s (or any arbitrary maximum value) is first calculated by brute force, i.e., by plotting Eqns. (2.51)-(2.52) versus fh for $c = 10$ km/s and scanning the plot to find the location of the root. Successive roots are then calculated using the same procedure as for the

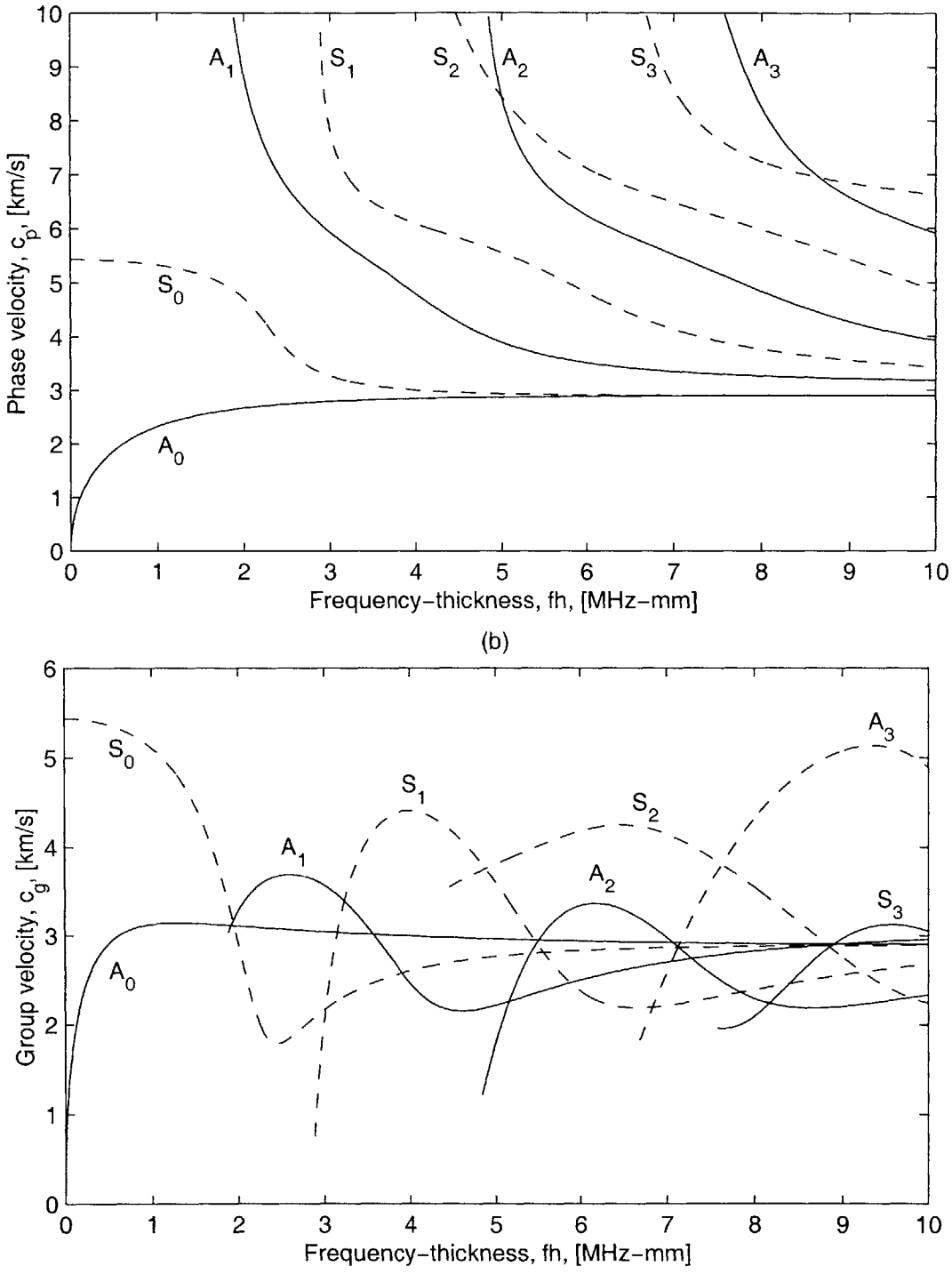

Figure 2-7: Dispersion curves for aluminum plotted against the frequency-thickness product, fh, in terms of (a) phase velocity c and (b) group velocity c_g.

fundamental modes.

For sufficiently small $\Delta(fh)$, the group velocity c_g may be calculated using a simple finite-difference approximation to

$$c_g = \frac{d\omega}{dk}. \tag{2.56}$$

The angular frequency and wavenumber may be calculated from the phase velocity and frequency, and the derivative is approximated by taking

$$\frac{d\omega}{dk} \approx \frac{\omega(k + \Delta k) - \omega(k)}{\Delta k} \tag{2.57}$$

for sufficiently small Δk.

Chapter 3

Time-Frequency Analysis Using Wavelets

3.1 Introduction

Once the multi-mode Lamb wave signals have been obtained, it is then necessary to consider the method by which the velocity information is to be extracted from the signals. In signal processing, transformations are often used to extract certain features of the signal which may otherwise be difficult to observe in its original form. The kind of information that can be extracted depends on the characteristics of the basis functions used in the transformation.

3.1.1 The Classical Fourier Transform

In the classical Fourier transform (FT), a signal $f(t)$ is expressed as the sum of functions $\{e^{i\omega t}\}$ with pure frequency ω. The Fourier transform $\hat{f}(\omega)$ is defined as

$$\hat{f}(\omega) = \int_{-\infty}^{\infty} f(t)e^{-i\omega t}dt \tag{3.1}$$

which provides a measure of the spectral content of the function $f(t)$ over the whole time domain. In the time-frequency plane, the Fourier transform represents information along the line $\omega = \omega'$, as shown in Fig. 3-1a. Hence, evaluating the FT in the entire frequency range maps a signal from the time domain onto the frequency domain.

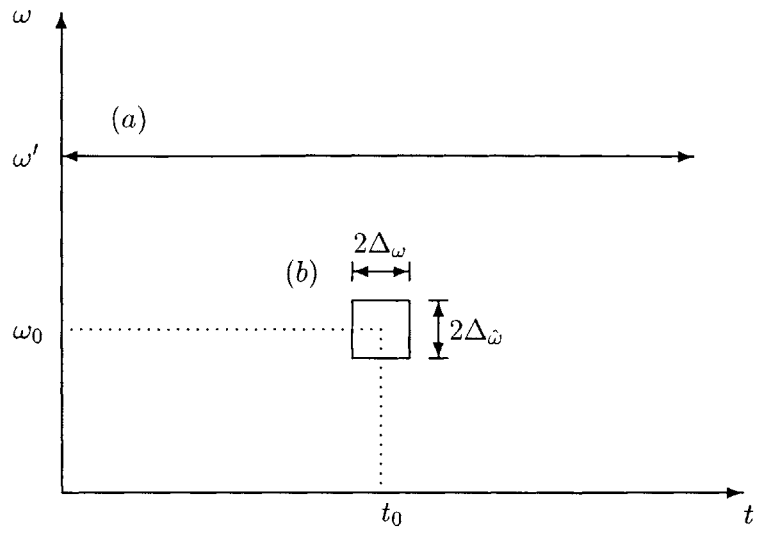

Figure 3-1: Region investigated in the time-frequency plane by (a) the Fourier transform and (b) time-frequency analysis.

3.1.2 Nonstationary Signals and Time Frequency Analysis

There are many instances, however, when one may be interested in measuring the spectral content of a signal over a localized span of time. For instance, Fig. 3-2 shows signals with finite support[1], localized features or time-varying frequency content. When analyzing such signals, it might be desired to localize in both time and frequency so as to capture their local temporal characteristics as well. It is beneficial in these cases to inspect a finite area in the time-frequency plane instead of a line, as shown in Fig. 3-1b. In such a *time-frequency analysis*, the temporal and spectral characteristics are investigated simultaneously, and the transform coefficients measure the average spectral content over a finite interval in time.

3.2 Short-Time Fourier Transform

To address the deficiencies of the Fourier transform in extracting local frequency information, a time-localizing window function is often used [36]. This method is known as the

[1]The support of a function f is defined as "the smallest closed set A for which $f(x)$ is identically zero for all $x \notin A$" [36].

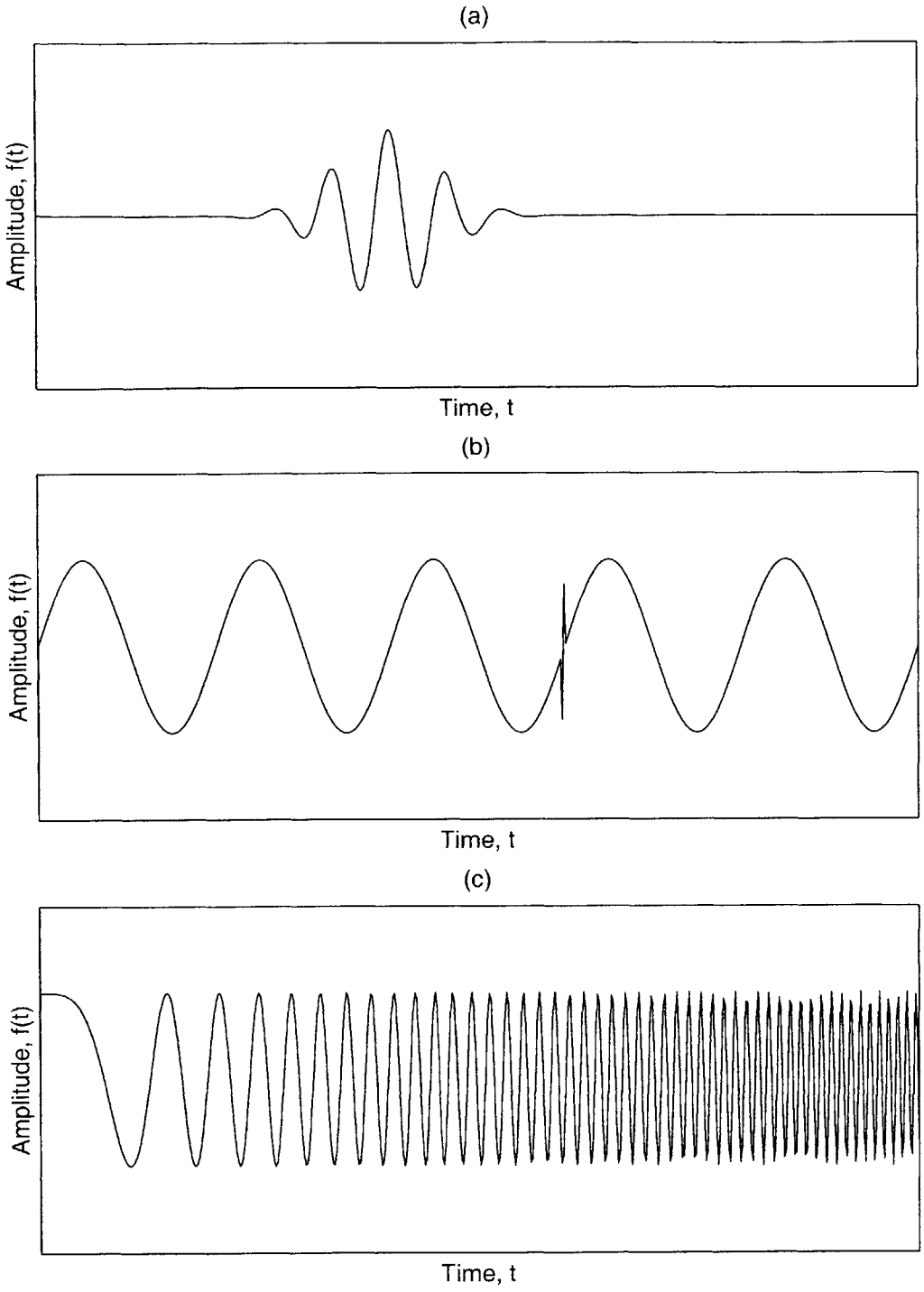

Figure 3-2: Nonstationary signals with (a) compact support, (b) local features and (c) time-varying frequency content.

short-time Fourier transform (STFT). The STFT of a function $f(t)$ is defined as

$$F(\omega, b) = \int_{-\infty}^{\infty} \left[f(t) e^{-i\omega t} \right] w(t-b) dt \tag{3.2}$$

where $w(t)$ is a window function and the parameter b is varied so as to cover the whole time axis. A function qualifies as a window function if it is in $L^2(R)$ where R is the set of real numbers. This requires that

$$\int_{-\infty}^{\infty} |tw(t)|^2 dt < \infty. \tag{3.3}$$

The center of a window function, t_0 is defined as

$$t_o = \frac{1}{\|w\|_2^2} \int_{-\infty}^{\infty} t|w(t)|^2 dt, \tag{3.4}$$

where $\|w\|_2$ is the L^2 norm, defined as

$$\|w\|_2 = \left\{ \int_{-\infty}^{\infty} |w(t)|^2 dt \right\}^{\frac{1}{2}}. \tag{3.5}$$

The radius Δ_w, or half the width of the window, is defined as the standard deviation or root mean squared duration of w,

$$\Delta_w = \frac{1}{\|w\|_2} \left\{ \int_{-\infty}^{\infty} (t-t_o)^2 |w(t)|^2 dt \right\}^{1/2}. \tag{3.6}$$

If w is to be used as a window function for time-frequency analysis, then it must also provide localization in the frequency domain, i.e., its Fourier transform $\hat{w}$ must also satisfy Eqn. (3.3). Although the smallest possible time-frequency window is generally desired, the widths of the window functions w and $\hat{w}$ satisfy the Heisenberg Uncertainty Principle [36, 37]

$$(2\Delta_w)(2\Delta_{\hat{w}}) \geq 2. \tag{3.7}$$

This principle states that there is a lower limit to the size of the time-frequency window, and therefore to the degree of accuracy with which we can analyze a signal in both time

and frequency. Equality in Eqn. (3.7) holds if and only if w is a Gaussian function, i.e.,

$$w_g(t) = e^{-\left(\frac{t}{\alpha}\right)^2}. \tag{3.8}$$

The Fourier transform or $\hat{\omega}_g$ is also a Gaussian and is given by

$$\hat{w}_g(\omega) = \sqrt{\pi}\alpha e^{-\left(\frac{\alpha\omega}{2}\right)^2}. \tag{3.9}$$

The widths of w_g and $\hat{w}_g$ are

$$2\Delta_{w_g} = \alpha, \tag{3.10}$$

$$2\Delta_{\hat{w}_g} = \frac{2}{\alpha}. \tag{3.11}$$

Once the widths of the window functions are selected, the shape and size of the time-frequency window does not change as ω or t changes. However, when low frequencies are to be analyzed, a wide window in time is desired while windows that are sharper in time are preferred when dealing with high frequencies. The rigidity of the STFT time-frequency window becomes a disadvantage when the signal to be analyzed contains both high and low frequencies. When dealing with such broadband signals, a flexible time-frequency window which widens and narrows with changing frequency is more advantageous. With wavelets, this flexibility comes automatically.

3.3 The Wavelet Transform

The most basic wavelet, the Haar wavelet, was invented in 1910 [38, 39]. The development of wavelet analysis was led by Meyer, Morlet and Grossman, but it wasn't until the innovations of Daubechies and Mallat when an explosion of interest and activity in wavelet theory and applications occurred [36]. Since then, wavelets have found applications in signal processing, image analysis data compression, and many other fields.

3.3.1 The Continuous Wavelet Transform

In the early 1980s, Morlet introduced a 'wavelet' which was dilated and translated to form a family of analyzing functions. These functions are normalized as [38]

$$\psi_{a,b}(t) = \frac{1}{\sqrt{a}}\psi\left(\frac{t-b}{a}\right). \tag{3.12}$$

which is a dilation (denoted by a) and translation (denoted by b) of the mother wavelet[2] $\psi(t)$. The continuous wavelet transform (CWT) is defined as

$$W(a,b) = \int f(t)\overline{\psi}_{a,b}dt, \tag{3.13}$$

where the bar denotes complex conjugation. The wavelet transform computes the correlation between the signal and the dilation and translation of the wavelet $\psi(t)$. The coefficients are therefore a measure of the similarity between the wavelet and the function $f(t)$.

3.3.2 Admissibility Condition

If the wavelet $\psi(t)$ satisfies the admissibility condition

$$C_\psi = 2\pi\int_{-\infty}^{\infty}\frac{|\hat{\psi}(\omega)|^2}{|\omega|}d\omega < \infty, \tag{3.14}$$

then the inverse transform can be computed with the reconstruction formula

$$f(t) = \frac{1}{C_\psi}\int\int W(a,b)\psi_{a,b}(t)\frac{da\ db}{a^2}. \tag{3.15}$$

The admissibility condition requires [38, 39]

$$\hat{\psi}(0) = \int_{-\infty}^{\infty}\psi(t)dt = 0. \tag{3.16}$$

[2]The *mother wavelet* "gives birth" to a family of wavelets through the operations of dyadic dilation and integer translation [36].

3.3.3 Fast Wavelet Transform

In the late 1980s Mallat proposed a fast algorithm for the computation of wavelet coefficients based on the concept of multiresolution analysis. This multiresolution analysis is generated by the scaling function $\phi(t)$, sometimes called the *father wavelet*, which satisfies the two-scale relation [38]

$$\phi(t) = 2\sum h_n \phi(2t - n) \tag{3.17}$$

for given coefficients h_n. The associated wavelet is then generated by

$$\psi(t) = 2\sum (-1)^n \overline{h_{1-n}} \phi(2t - n). \tag{3.18}$$

The concept of multiresolution states that lower level scaling function and wavelet coefficients can be computed from given scaling function coefficients at a higher level [36], leading to a Fast Wavelet Transform (FWT) [3].

3.3.4 The Morlet Wavelet

The wavelet used in this study is the Morlet wavelet, defined as [3]

$$\psi_M(t) = e^{i\omega_0 t} e^{-\left(\frac{t}{\alpha}\right)^2}. \tag{3.19}$$

Traditionally, the parameters α and ω_0 are defined as [39]

$$\alpha = \sqrt{2} \tag{3.20}$$

$$\omega_o = \pi\sqrt{\frac{2}{\ln 2}}. \tag{3.21}$$

The corresponding wavelet is plotted in Fig. 3-3. But these parameters may be varied in order to get more accurate results, as will be shown in Chapter 5.

The Morlet wavelet is simply a Gaussian modulated harmonic function whose Fourier

[3] For a detailed discussion, see for instance Cohen (1995) or Strang (1997).

transform, $\hat{\psi}_M$, can be deduced from using Eqns. (3.8)-(3.9),

$$\hat{\psi}_M(\omega) = \sqrt{\pi}\alpha e^{-\left[\frac{\alpha(\omega-\omega_0)}{2}\right]^2}. \tag{3.22}$$

The Morlet wavelet qualifies as a window function in both time and frequency, but it does not satisfy Eqn. (3.16) exactly. However, the actual value is very small and is negligible. Despite this, the Morlet wavelet has some very good characteristics. Since the Morlet is essentially a Gaussian, the area of the time-frequency window is at the minimum possible value allowed by the Heisenberg Uncertainty Principle [Eqn. (3.7)]. In particular, the widths of ψ_M and $\hat{\psi}_M$ are the same as in Eqns. (3.10)-(3.11).

$$2\Delta_{\psi_M} = \alpha, \tag{3.23}$$

$$2\Delta_{\hat{\psi}_M} = \frac{2}{\alpha}. \tag{3.24}$$

The disadvantage of using the Morlet wavelet is that it does not have a scaling function associated with it [40]. It cannot, therefore, be implemented by a Fast Wavelet Transform.

3.3.5 Remarks

There are many other wavelets aside from the Morlet that one may choose from, and many more that are being designed. Some of the more well known are the Meyer and Daubechies wavelets [39]. The optimality of a particular wavelet largely depends on the particular application and the objectives of the analysis. Generally, the Morlet wavelet transform is computationally more expensive compared to other wavelet transforms in that there is no fast algorithm that can implement it. Using other wavelets may be more attractive computationally, but there is a necessary compromise in resolution.

3.4 Comparison between the Wavelet and Fourier Transform

The key distinction between the wavelet and the short-time Fourier transform lies in the dimensions of the time-frequency window. While the widths of the time-frequency window in the STFT is constant or rigid, those in the WT vary with the scaling parameter a. In

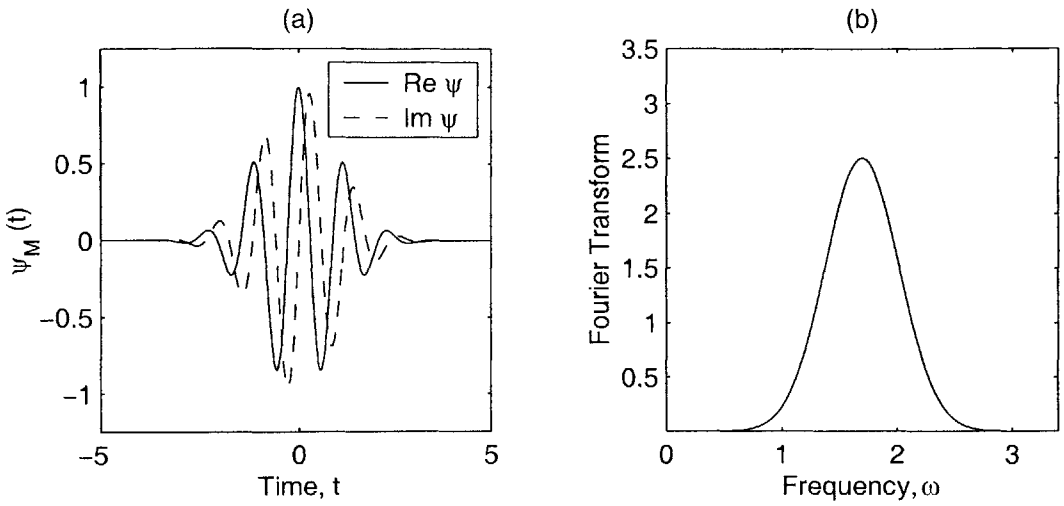

Figure 3-3: (a) The Morlet wavelet, $\psi_M(t)$ and (b) the magnitude of its Fourier transform, $|\hat{\psi}_M(t)|$.

particular, the time window width at scale a is

$$\Delta_{\psi_{a,b}} = a\Delta_{\psi_M}, \tag{3.25}$$

and the frequency window width is

$$\Delta_{\hat{\psi}_{a,b}} = \frac{\Delta_{\hat{\psi}_M}}{a}, \tag{3.26}$$

At high frequencies (low a), the width of the time window decreases, giving better resolution in the time domain. At low frequencies (high a), the width increases adapting to longer periods. In other words, the size of the time-frequency window in STFT is rigid, whereas in the WT, the widths change according to frequency variations. Since the periods at high frequencies is smaller and vice versa, this characteristic makes the wavelet transform more suitable for analyzing signals containing a wide range of frequencies. Furthermore, a comparison between the Morlet wavelet transform and the Fourier transform reveals that the Morlet WT is equivalent to a Gaussian-windowed Fourier transform with varying window widths.

3.5 Wavelet Transform and Dispersion

To illustrate the use of the wavelet transform in the analysis of dispersion, we consider once again the sum of two propagating harmonic waves with equal and unit amplitudes but slightly different angular frequencies,

$$f(x,t) = e^{i(k_1 x - \omega_1 t)} + e^{i(k_2 x - \omega_2 t)}. \tag{3.27}$$

Taking the Morlet wavelet transform of f at scale a and translation b,

$$W(a,b) = \frac{1}{\sqrt{a}} \int_{-\infty}^{\infty} \left[e^{i(k_1 x - \omega_1 t)} + e^{i(k_2 x - \omega_2 t)} \right] e^{-\left(\frac{t-b}{a\alpha}\right)^2} e^{-i\omega_o\left(\frac{t-b}{a}\right)} dt. \tag{3.28}$$

Letting $y = \frac{t-b}{a}$, Eqn. (3.28) can be expressed as

$$W(a,b) = \sqrt{a} e^{i(k_1 x - \omega_1 b)} \int_{-\infty}^{\infty} \left[e^{-\left(\frac{y}{\alpha}\right)^2} e^{i\omega_o y} \right] e^{-i\omega_1 a y} dy + \sqrt{a} e^{i(k_2 x - \omega_2 b)} \int_{-\infty}^{\infty} \left[e^{-\left(\frac{y}{\alpha}\right)^2} e^{i\omega_o y} \right] e^{-i\omega_2 a y} dy \tag{3.29}$$

Simplifying, we obtain

$$W(a,b) = \sqrt{a} \left[e^{i(k_1 x - \omega_1 b)} \hat{\psi}_M(a\omega_1) + e^{i(k_2 x - \omega_2 b)} \hat{\psi}_M(a\omega_2) \right] \tag{3.30}$$

Taking the modulus of $W(a,b)$, we obtain

$$|W(a,b)| = \sqrt{a} \left\{ \left[\hat{\psi}_M(a\omega_1) \right]^2 + \left[\hat{\psi}_M(a\omega_2) \right]^2 + 2\hat{\psi}(a\omega_1)\hat{\psi}(a\omega_2) \cos\left[2\Delta k x - 2\Delta\omega b\right] \right\}^{\frac{1}{2}} \tag{3.31}$$

where

$$\Delta\omega = \frac{1}{2}(\omega_1 - \omega 2) \qquad \Delta k = \frac{1}{2}(k_1 - k_2) \tag{3.32}$$

and $\hat{\psi}_M(\omega)$ is given by Eqn. (3.22). If $\Delta\omega$ is sufficiently small so that

$$\hat{\psi}(a\omega_1) \approx \hat{\psi}(a\omega_2) \approx \hat{\psi}(a\omega), \tag{3.33}$$

then

$$\frac{1}{\sqrt{a}}\left|W(a,b)\right| \approx \sqrt{2\pi}\alpha e^{-\frac{\alpha(a\omega-\omega_o)^2}{2}}\left[1+\cos\left(2\Delta k x - 2\Delta\omega b\right)\right]^{\frac{1}{2}}. \tag{3.34}$$

For fixed x, $\frac{1}{\sqrt{a}}\left|W(a,b)\right|$ has a maximum at

$$a = \frac{\omega_o}{\omega}, \tag{3.35}$$

while for fixed frequency ω, the maximum occurs at

$$b = \frac{x\Delta k}{\Delta\omega} = \frac{x}{c_g}. \tag{3.36}$$

Hence, the wavelet transform coefficients $W(a,b)$ yield a maximum value corresponding to the time of arrival b of a wave of frequency $\omega = \omega_o/a$.

Chapter 4

Numerical Implementation

4.1 Introduction

To evaluate the method proposed in the previous chapters, a numerical study is performed. In the first part of the study, single mode signals are simulated and analyzed. The results are used to determine the optimal values of the parameters in the Morlet wavelet. The second part of the study deals with the refinement of the algorithm for the purpose of analyzing multimode signals. The results show that the wavelet transform is a potentially effective tool in analyzing the time-frequency characteristics of multimode signals.

4.2 General Procedure

The simulations shown in this chapter follow a common procedure shown schematically in Fig. 4-1. First, a magnitude response of unity is assumed and the phase response ϕ is defined as a function of frequency ω. Then, by definition, the group delay $\tau(\omega)$ is also known. The simulated system transfer function is then

$$H(\omega) = A(\omega)e^{i\phi(\omega)} = e^{i\phi(\omega)}. \tag{4.1}$$

The impulse response, $h(t)$ is

$$h(t) = \frac{1}{2\pi}\int_{-\infty}^{\infty} e^{i\phi(\omega)}e^{i\omega t}d\omega. \tag{4.2}$$

The time-frequency characteristics of $h(t)$ are analyzed by calculating the wavelet transform coefficients $W(a,b)$. This yields the group delay $\overline{\tau}$ as a function of frequency. The calculated group delay is be denoted by $\overline{\tau}$ to distinguish it from the actual group delay τ. The results are compared with the actual group delay, and the algorithm is refined as needed.

4.2.1 Implementation of the Wavelet Transform

The following algorithm by Misiti *et al.* [40] was used to implement the Morlet wavelet transform in MATLAB [1] .

The wavelet transform coefficients of a discrete signal $s(t)$ are given by

$$W(a,b) = \frac{1}{\sqrt{a}} \int_{-\infty}^{+\infty} s(t)\psi\left(\frac{t-b}{a}\right) dt. \tag{4.3}$$

Since $s(t)$ is a discrete signal, a piecewise constant interpolation is used,

$$s(t) = s(k) \qquad \text{for} \qquad t \in [k, k+1]. \tag{4.4}$$

Equation (4.3) can then be written as

$$W(a,b) = \frac{1}{\sqrt{a}} \sum_{k=0}^{M-1} s(k) \int_{k}^{k+1} \psi\left(\frac{t-b}{a}\right) dt \tag{4.5}$$

where M is the total number of samples in the discrete signal. Rewriting,

$$W(a,b) = \frac{1}{\sqrt{a}} \sum_{k=0}^{M-1} s(k) \left[\int_{-\infty}^{k+1} \psi\left(\frac{t-b}{a}\right) dt - \int_{-\infty}^{k} \psi\left(\frac{t-b}{a}\right) dt\right]. \tag{4.6}$$

At any scale a, $W(a,b)$ can be obtained by convolving s with a dilated and translated version of the integral

$$\int_{-\infty}^{k} \psi(t)dt. \tag{4.7}$$

Whereas MATLAB defines the Morlet wavelet as

$$\psi_M(t) = e^{-\frac{t^2}{2}} \cos 5t, \tag{4.8}$$

[1] MATLAB is a trademark of The Mathworks Inc. MATLAB v. 5.2 was used in this study.

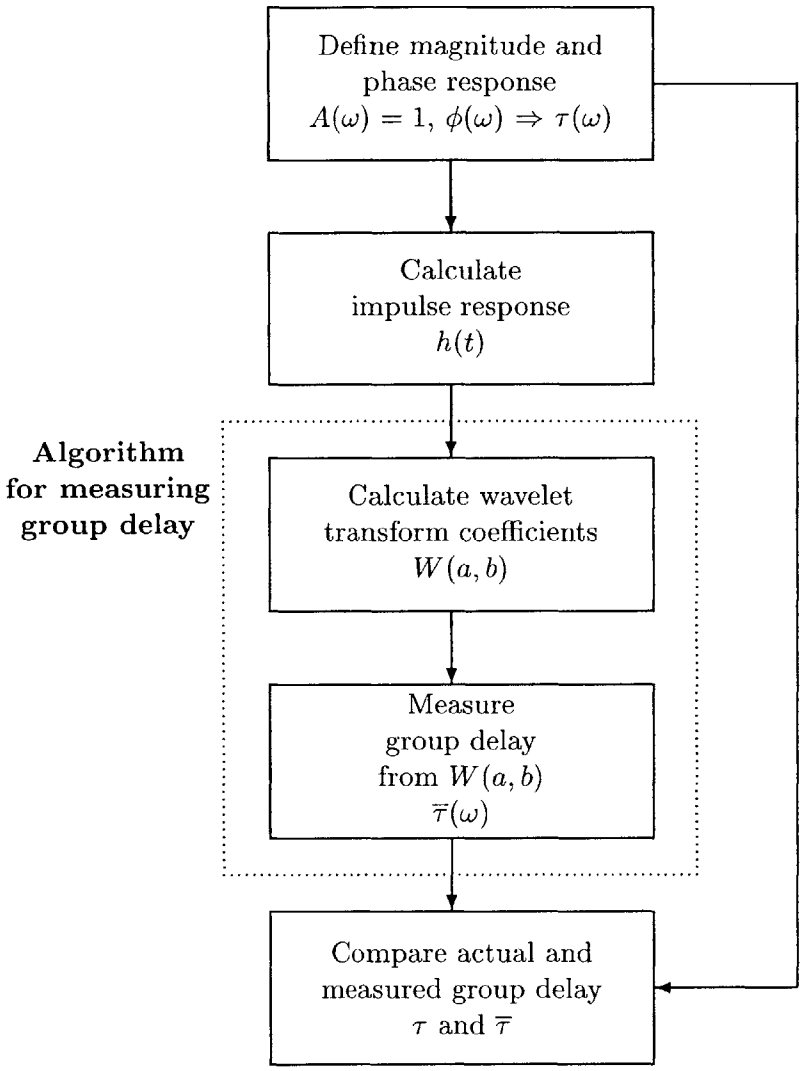

Figure 4-1: General procedure used in numerical simulations. Measurement of the group delay, $\overline{\tau}(\omega)$, are determined from the wavelet transform coefficients and compared with the actual group delay $\tau(\omega)$.

the definition in Eqn. (3.19) is used in this study. Using the complex valued function preserves the Gaussian shape of the wavelet amplitude, making it easier to locate the peaks in the coefficients. As mentioned in Section 3.3.4, using this definition allows us to vary the parameters α and ω_o in order to get more accurate results. The group delay may then be calculated from the wavelet coefficients (see Section 3.5).

The accuracy of the calculated group delay depends partly on how the parameters of the Morlet wavelet are defined. The Morlet wavelet transform as defined in Section 3.3.4 exhibits two degrees of freedom: α and ω_o. Theoretically, the wavelet transform coefficients (times a factor $\frac{1}{\sqrt{a}}$) exhibit maxima corresponding to the time of arrival and frequency of the wave packet. The results of Section 3.5 were arrived upon without regard to the values of α and ω_o. However, the values of these two parameters affect the detectability of these maxima. If the wavelet bandwidth is too wide or too narrow, the group delay will not be detected accurately. For instance, if the bandwidth is much too narrow, then the WT becomes very similar to the Fourier transform, and local time information cannot be obtained. For the purposes of time-frequency analysis, a good balance between the time and frequency widths must be achieved.

All of the signals considered in this thesis will be analyzed from frequencies of approximately 0 to the Nyquist frequency which, for a sampling period of 1, is π. Although a more thorough parametric study may be performed, the center frequency ω_o is arbitrarily chosen to be half the Nyquist frequency or $\pi/2$. The value of α will then be varied to obtain the most accurate results.

4.3 Single Mode Signals

4.3.1 Test Signals

Table 4.1 summarizes the characteristics of the responses $h(t)$ considered in the simulations. A sampling period of 1 was assumed to facilitate the application of the method to signals with arbitrary sampling periods, for which the time axis only needs to be rescaled by Δt. The value for N, the number of samples, was chosen to match with the actual length of the experimental signals to be analyzed in Chapter 6.

The phase response and corresponding group delay of each test signal are given in Table 4.2. Signals 1 and 2 have group delays varying linearly with frequency, while signals

3 and 4 have sinusoidally varying group delays. The group delay $\tau(\omega)$ and the resulting impulse response $h(t)$ for Signals 1 and 3 are shown in Figs. 4-2 and 4-3, respectively.

N	2500	Number of samples
Δt	1	Sampling period
f_n	$\frac{1}{2}$	Nyquist frequency
ω_n	π	Nyquist frequency (angular)

Table 4.1: Characteristics of the simulated response functions.

	Delay Shape	Symbol	Phase response, $\phi(\omega)$	Group delay, $\tau(\omega)$
Signal 1	Linear	$h_1(t)$	$-\frac{\omega^2}{2\pi}N$	$\frac{\omega}{\pi}N$
Signal 2	Linear	$h_2(t)$	$-\left(\omega - \frac{\omega^2}{2\pi}\right)N$	$\left(1 - \frac{\omega}{\pi}\right)N$
Signal 3	Sinusoidal	$h_3(t)$	$-\frac{1}{2}\left(\omega - \frac{1}{2}\cos 2\omega\right)$	$\frac{1}{2}\left(1 + \sin 2\omega\right)N$
Signal 4	Sinusoidal	$h_4(t)$	$-\frac{1}{2}\left(\omega + \frac{1}{2}\cos 2\omega\right)$	$\frac{1}{2}\left(1 - \sin 2\omega\right)N$

Table 4.2: The phase response and corresponding group delay of each of the four test signals.

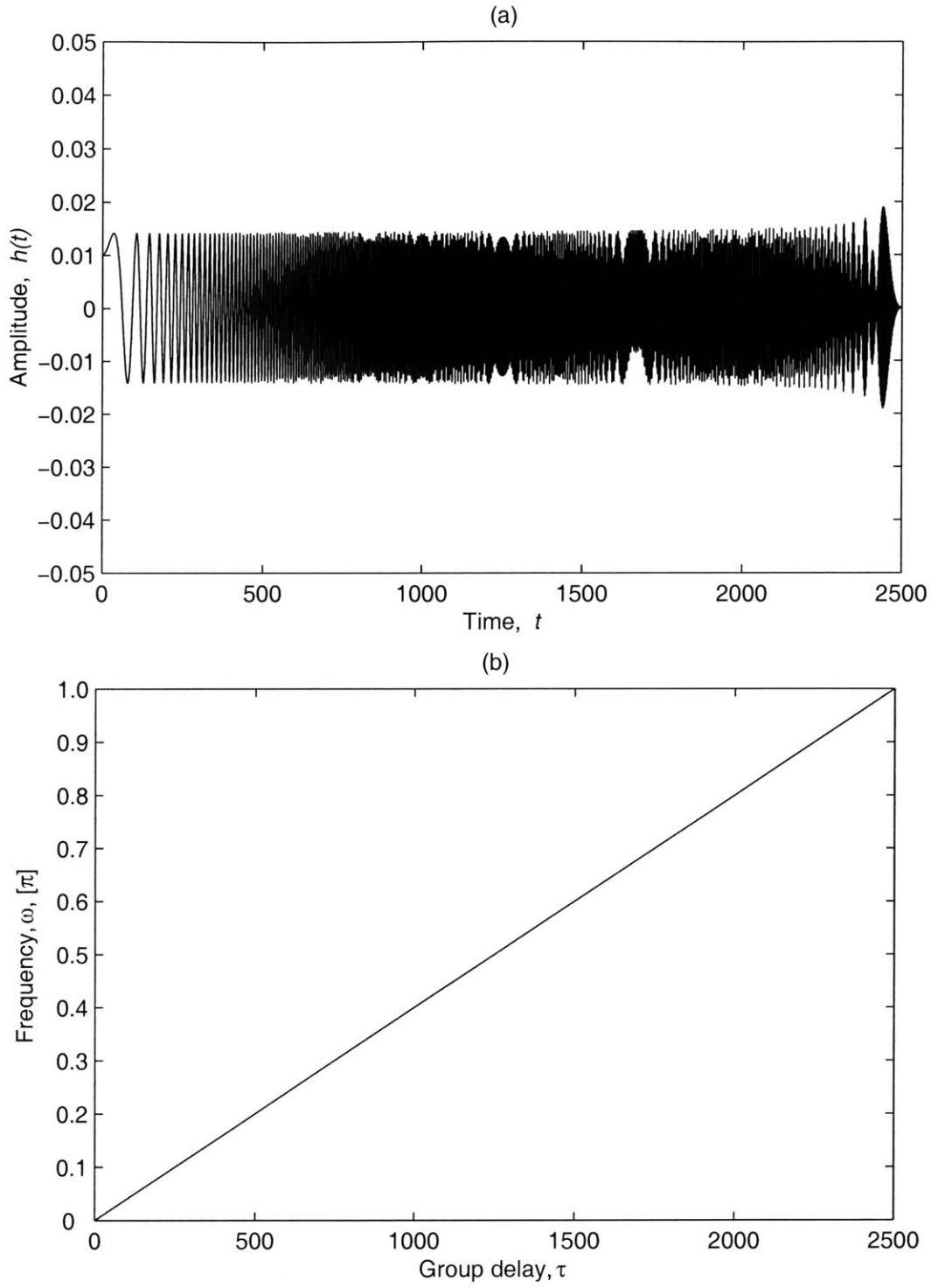

Figure 4-2: Signal 1: (a) Impulse response, $h_1(t)$ and (b) actual group delay, $\tau_1(\omega)$.

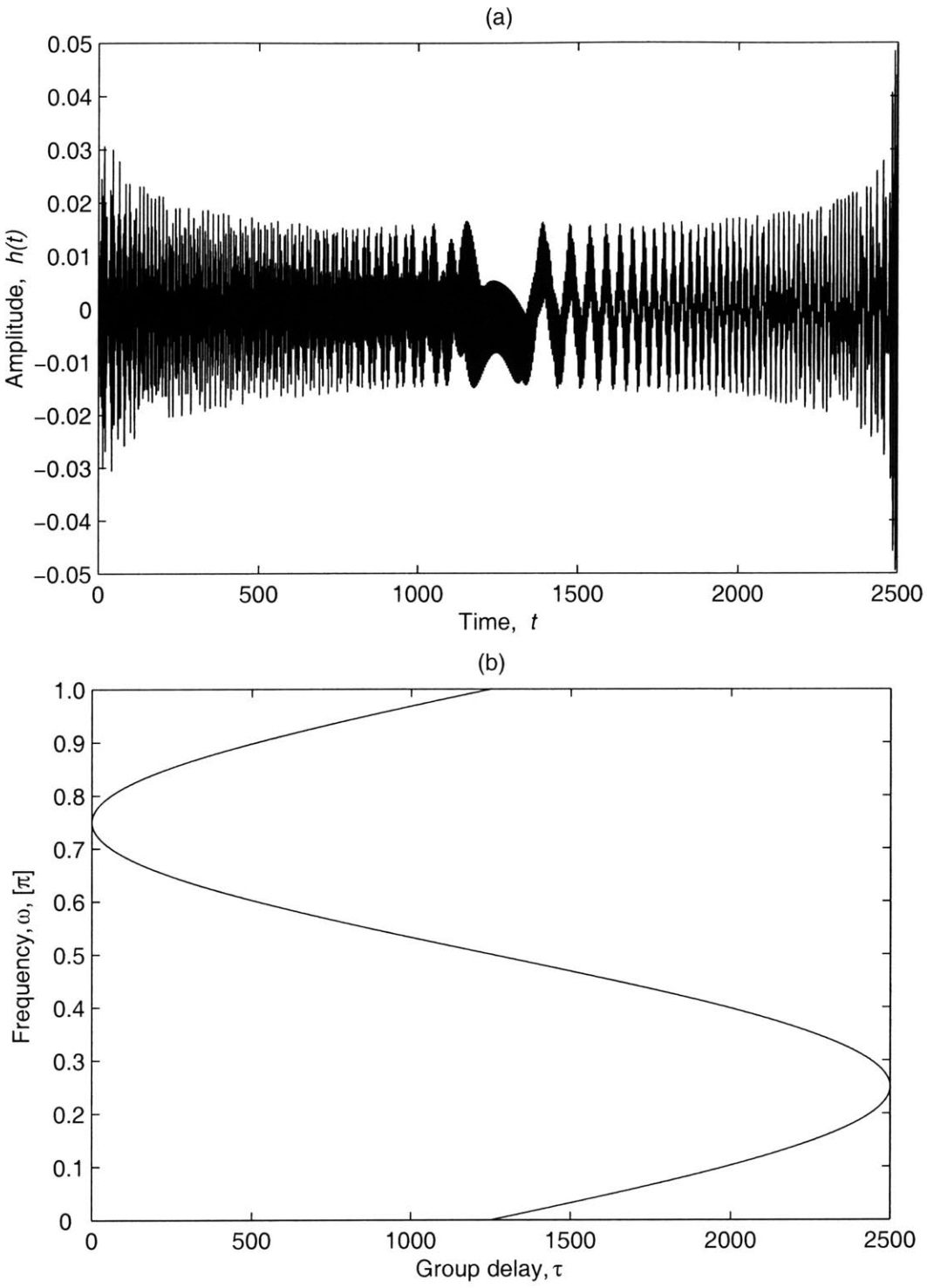

Figure 4-3: Signal 3: (a) Impulse response, $h_2(t)$ and (b) actual group delay, $\tau_2(\omega)$.

4.3.2 Group delay measurement algorithm

Figure 4-4(a) shows the magnitude of the wavelet transform coefficients, $W(a,b)$ evaluated at $\omega = \pi/2$ for Signal 1. The shift or translation parameter b is varied to cover the entire time axis. The actual group delay,

$$\tau\left(\frac{\pi}{2}\right) = \frac{N}{2} = 1250 \tag{4.9}$$

is indicated in the figure. The correspondence between the group delay and peaks in the wavelet transform coefficients (as described in Section 3.5) is evident. In theory, only one mode is present in the signal. However, the calculated coefficients exhibit some noise in the form of ghost peaks. These ghost peaks may cause problems when dealing with multimode signals since they may be mistaken for actual modes. These observations also hold for Fig. 4-4(b), which shows similar results for Signal 3.

Figure 4-5 shows the measurement algorithm used to analyze the single mode signals. The maxima in the coefficients can be found by detecting changes in the slope of the coefficients. For increasing b, a shift from positive slope to negative slope indicates the presence of a local maxima. Once the maxima have been located, the peak with the highest amplitude is chosen and taken to represent the group delay $\overline{\tau}$.

To illustrate, consider the coefficients shown in Fig. 4-6. A single dominant mode is shown, with some low magnitude peaks representing noise. The locations and magnitude of the local maxima are also known and indicated. The values of $\overline{\tau}$ at $\omega = \pi/2$ for the four test signals $h_1(t)$ to $h_4(t)$ are also given in Table (4.3).

4.3.3 Error measures

In comparing the actual and calculated group delays, τ and $\overline{\tau}$, two measures of error are considered. We define the *cumulative error* as

$$E_c(\alpha) = \frac{\|\tau - \overline{\tau}\|_2}{\|\tau\|_2} = \frac{\left\{\sum_{n=1}^{N}[\tau(\omega_n) - \overline{\tau}(\alpha,\omega_n)]^2\right\}^{1/2}}{\left\{\sum_{n=1}^{N}[\tau(\omega_n)]^2\right\}^{1/2}}. \tag{4.10}$$

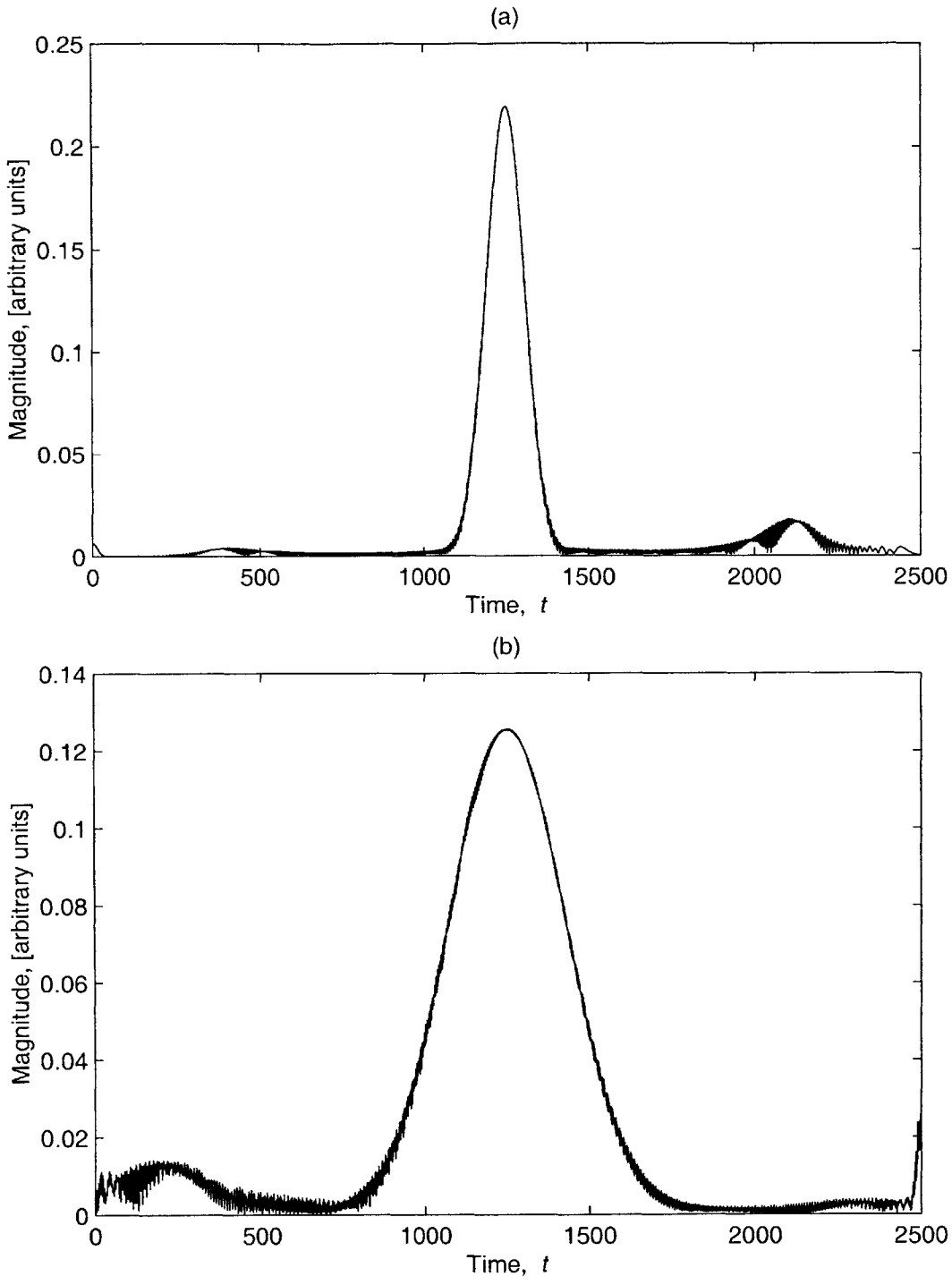

Figure 4-4: Wavelet transform coefficients evaluated at $\omega = \pi/2$ for (a) Signal 1 and (b) Signal 3.

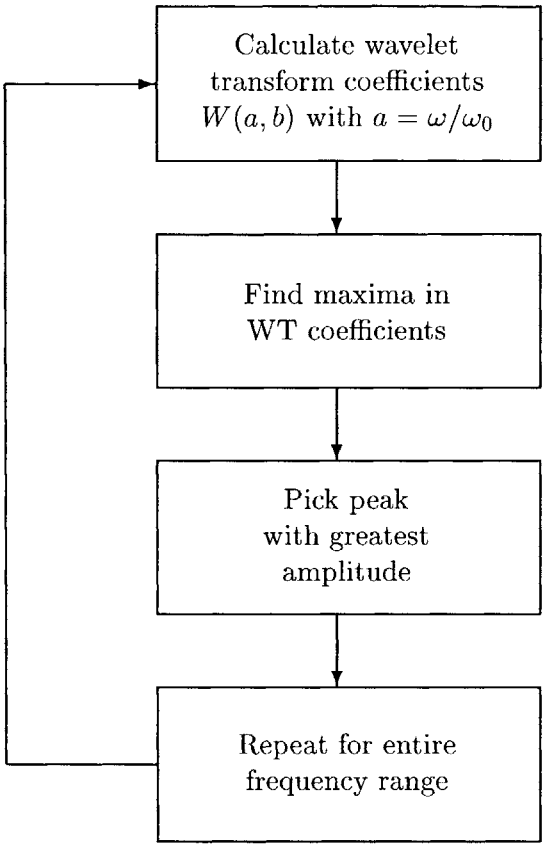

Figure 4-5: Group delay measurement algorithm used in analyzing single-mode signals.

	Actual group delay, τ	Calculated group delay, $\overline{\tau}$
Signal 1	1250	1252
Signal 2	1250	1252
Signal 3	1250	1254
Signal 4	1250	1251

Table 4.3: The actual and calculated group delays for Signals 1 to 4 at $\omega = \frac{\pi}{2}$.

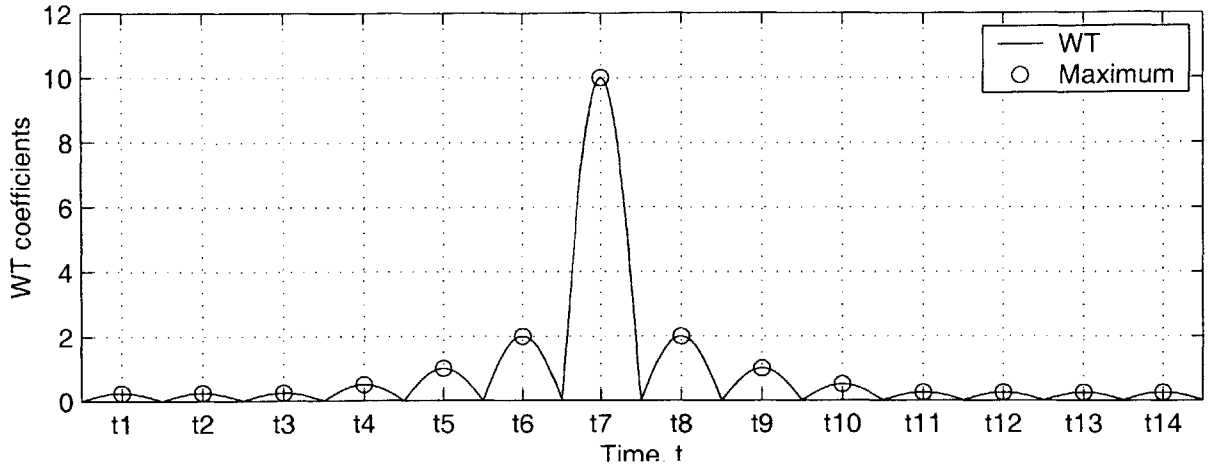

Location	t_7	t_6	t_5	t_9	...
Magnitude	10	2	2	1	...

Figure 4-6: Measuring the group delay for a single mode signal. The locations of the maxima are sorted according to the magnitude of the WT coefficients.

This error measure will be used to evaluate the overall error for a given value of α. We define the *absolute error* as

$$E_a(\alpha, \omega) = |\tau(\omega) - \overline{\tau}(\alpha, \omega)| \tag{4.11}$$

This error measure is useful in determining the dependence of error on frequency.

4.3.4 Results: Cumulative error

The cumulative error in the measured group delay for each test signal is plotted in Figs. 4-7 to 4-8. These results reveal a consistent pattern in the dependence of the error on α.

One common feature is the rapid increase in E_c as α is decreased from approximately $\alpha = 4$. This is expected since, by the definition of window width in Eqn. (3.6), the Morlet wavelet spans approximately one period at $\alpha = 4$. Choosing a smaller value would cause problems in time resolution and therefore yield greater errors. To illustrate, the Morlet mother wavelet is plotted in Fig. 4-9 for several values of α. The corresponding frequency transform is plotted next to the wavelet.

To understand the significance of the plots, it is important to note that the relevant frequency range – from 0 to the Nyquist frequency – corresponds to the region from 0 to 1 on the x-axis of the Fourier transform plots. For $\alpha = 1$, the bandwidth of the wavelet is much too large. The frequency bandwidth decreases for $\alpha = 4$, and becomes even sharper for $\alpha = 8$.

For $\alpha > 4$, the cumulative error tends to oscillate while slightly rising as α is increased. In this region, it is best to evaluate the error in terms of its variation with respect to frequency.

4.3.5 Results: Absolute Error

The results for $\alpha = 4, 20$ and 50 are shown in Figs. 4-10 to 4-15 to illustrate the dependence of error on frequency for a given value of α. To avoid repetition, only the results for Signals 1 (linear group delay) and 3 (sinusoidal group delay) are shown.

First, the images of the wavelet coefficients are presented. These images are formed by mapping the amplitude of the WT coefficients at each frequency to the corresponding darkness of the image pixels. Hence, pixel values along a vertical line in the images correspond to WT coefficient plots such as those in Fig. 4-4.

Next, the results of the group delay measurement algorithm – the dispersion curves – are given. Finally, the absolute error averaged over all four test signals is shown.

Results for $\alpha = 4$

The magnitude of the wavelet coefficients for $\alpha = 4$ are shown in Fig. 4-10. The resulting dispersion curves are in Fig. 4-11. For low frequencies this choice of α yields good results. However, the accuracy deteriorates greatly for high frequencies. This is more evident in Fig. 4-11(b), which shows the results for Signal 3.

Results for $\alpha = 20$

The magnitude of the WT coefficients for $\alpha = 20$ are shown in Fig. 4-12 and the dispersion curves are in Fig. 4-13. These results show a great improvement in accuracy. The dispersion pattern is very evident from the images, and the calculated group delays display excellent accuracy except for the extreme low and high frequencies.

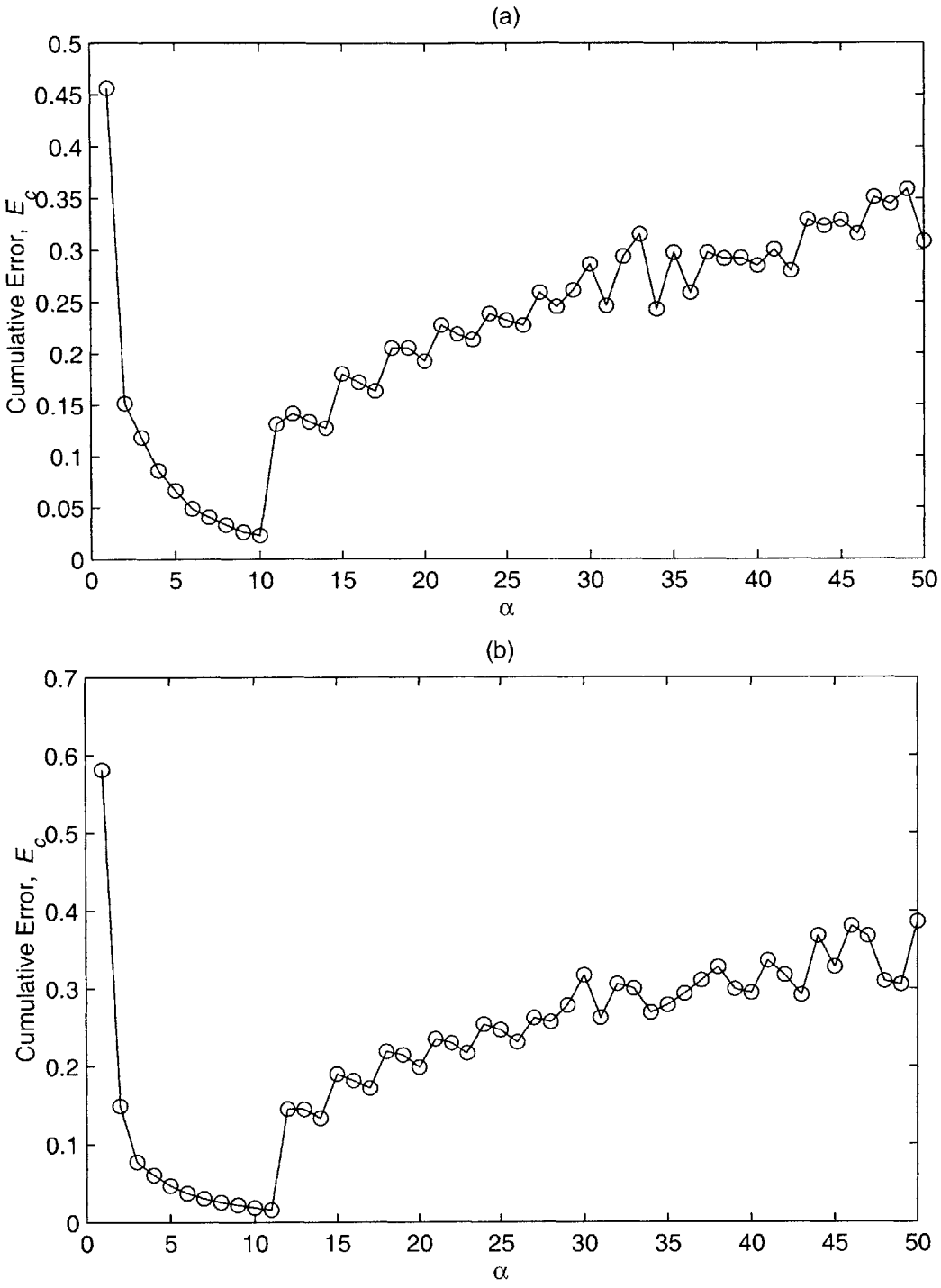

Figure 4-7: Cumulative error as a function of α with $\omega_0 = \pi/2$ for (a) Signal 1 and (b) Signal 2.

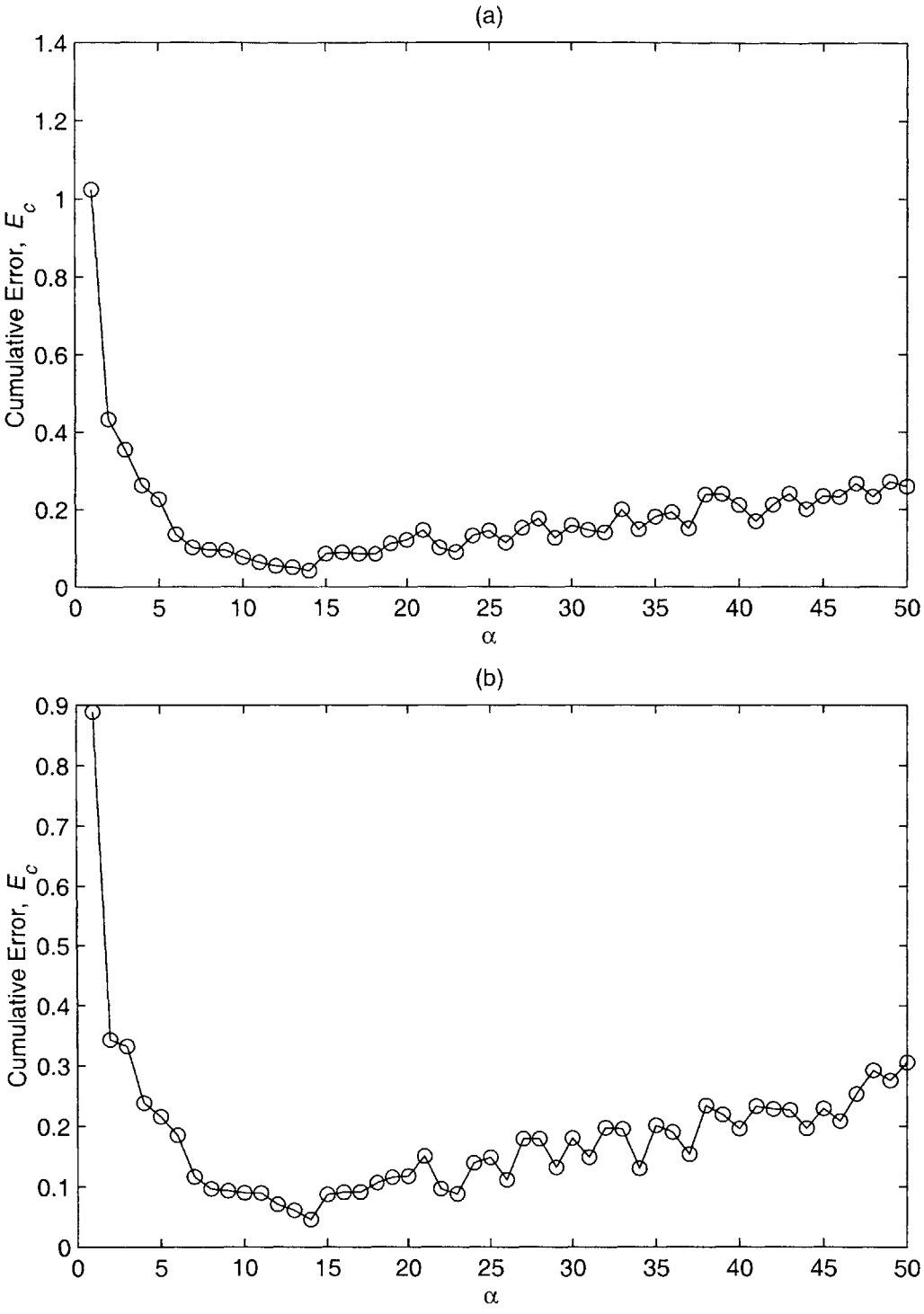

Figure 4-8: Cumulative error as a function of α with $\omega_0 = \pi/2$ for (a) Signal 3 and (b) Signal 4.

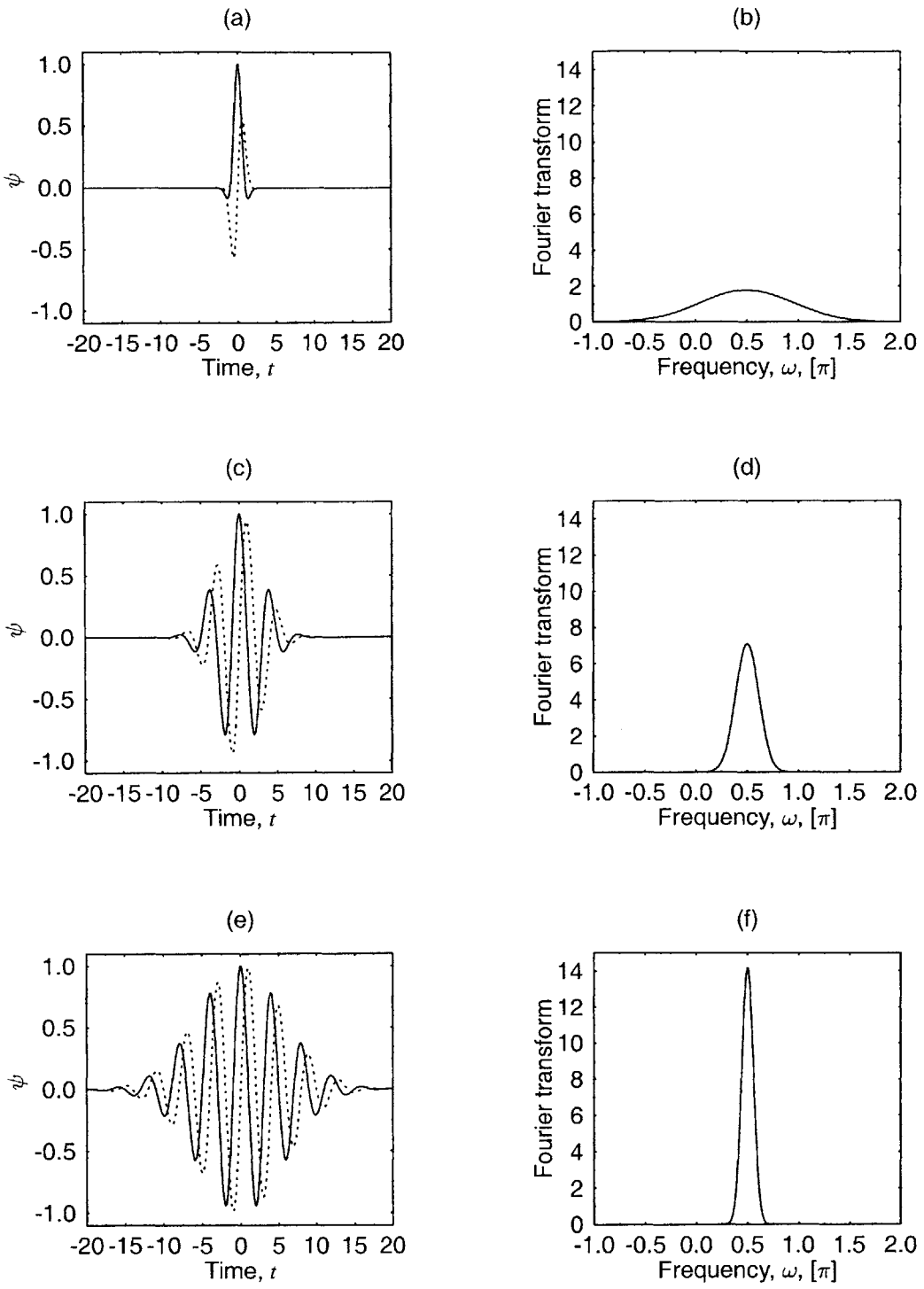

Figure 4-9: Morlet mother wavelet for ψ and its Fourier transform $\hat{\psi}$ for (a)-(b) $\alpha = 1$, (c)-(d) $\alpha = 4$, and (e)-(f) $\alpha = 8$.

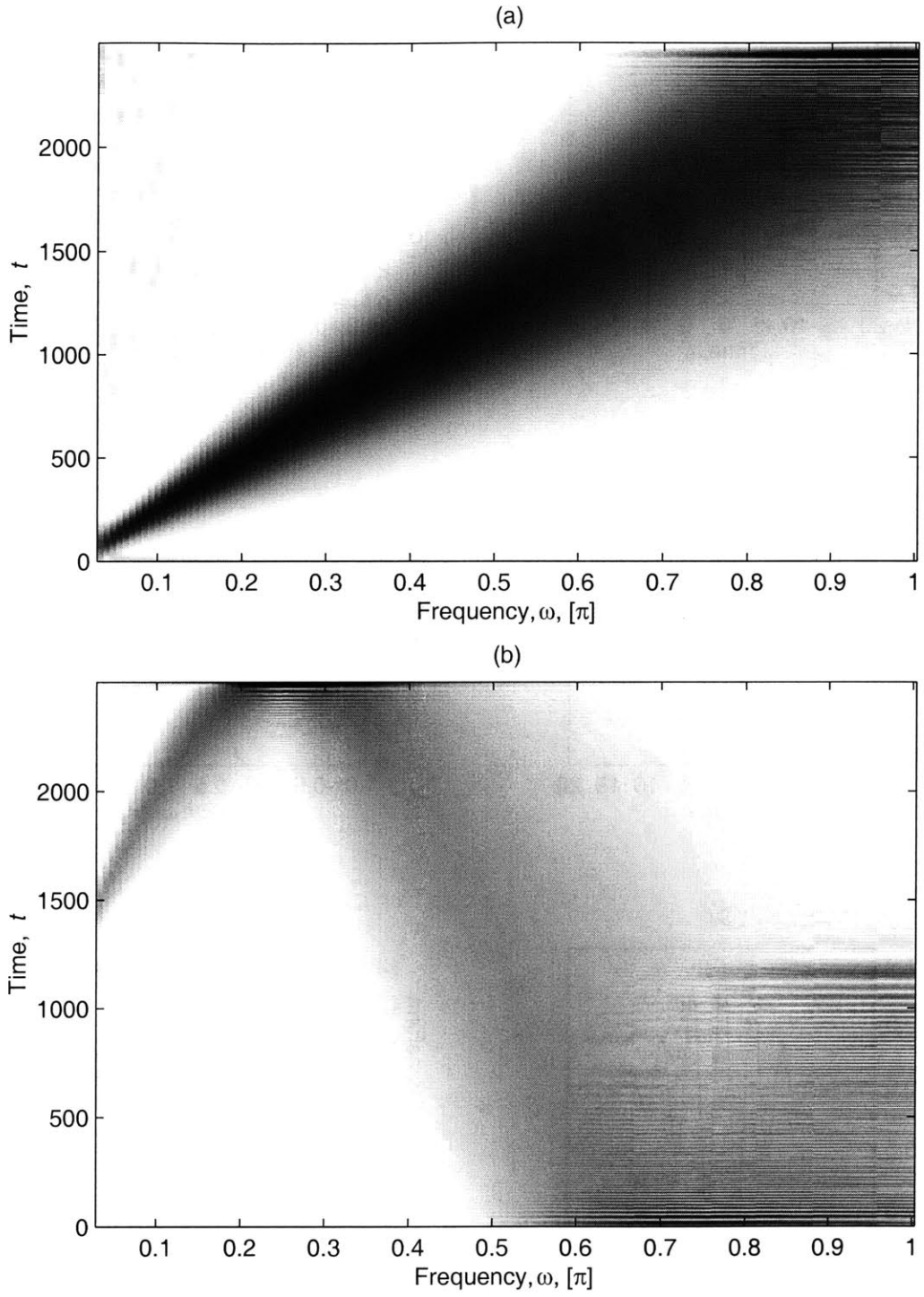

Figure 4-10: Image of wavelet coefficients for (a) Signal 1, $\alpha = 4$ and (b) Signal 3, $\alpha = 4$.

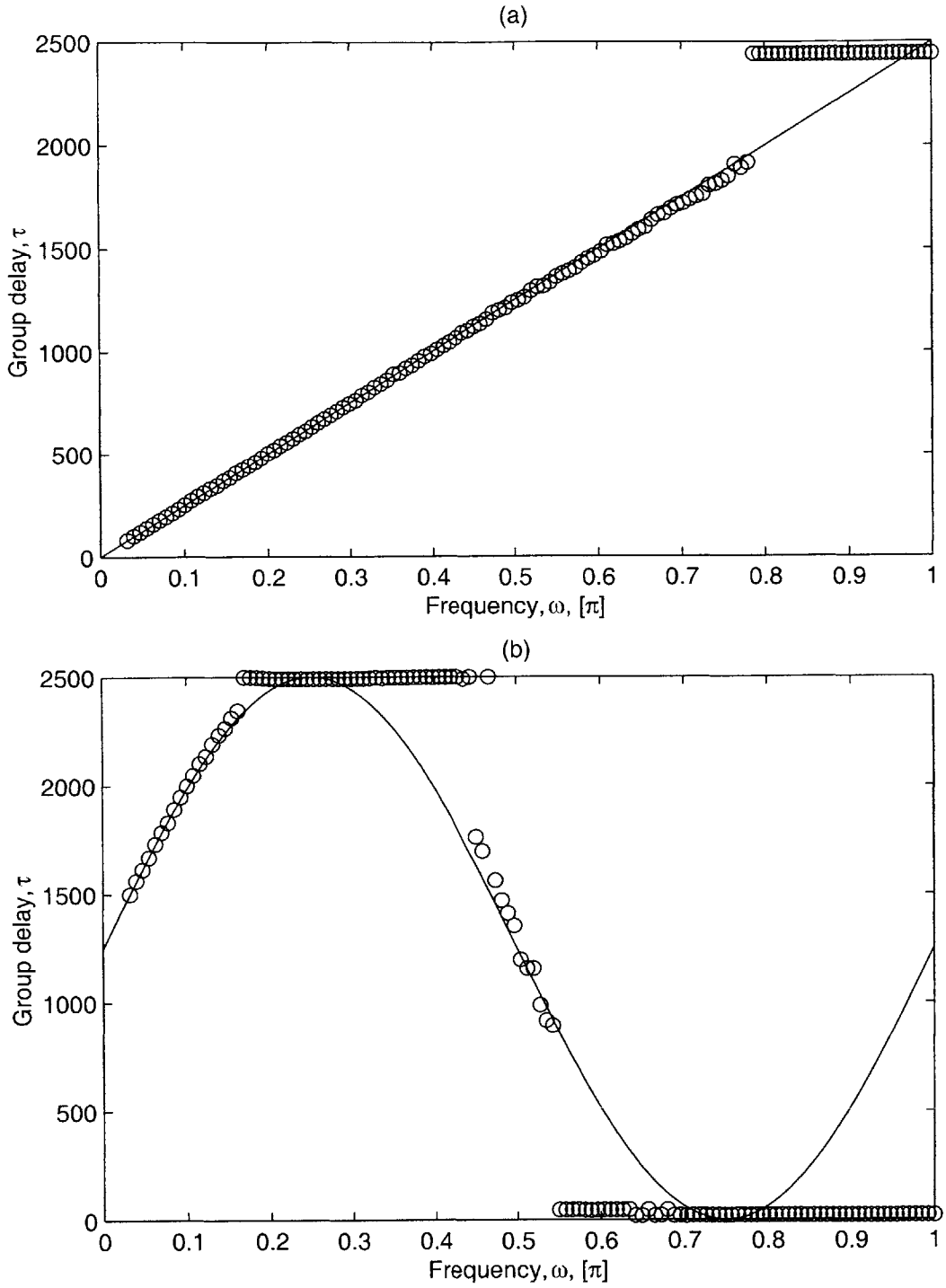

Figure 4-11: Comparison between the actual and calculated group delay for (a) Signal 1, $\alpha = 4$ and (b) Signal 3, $\alpha = 4$.

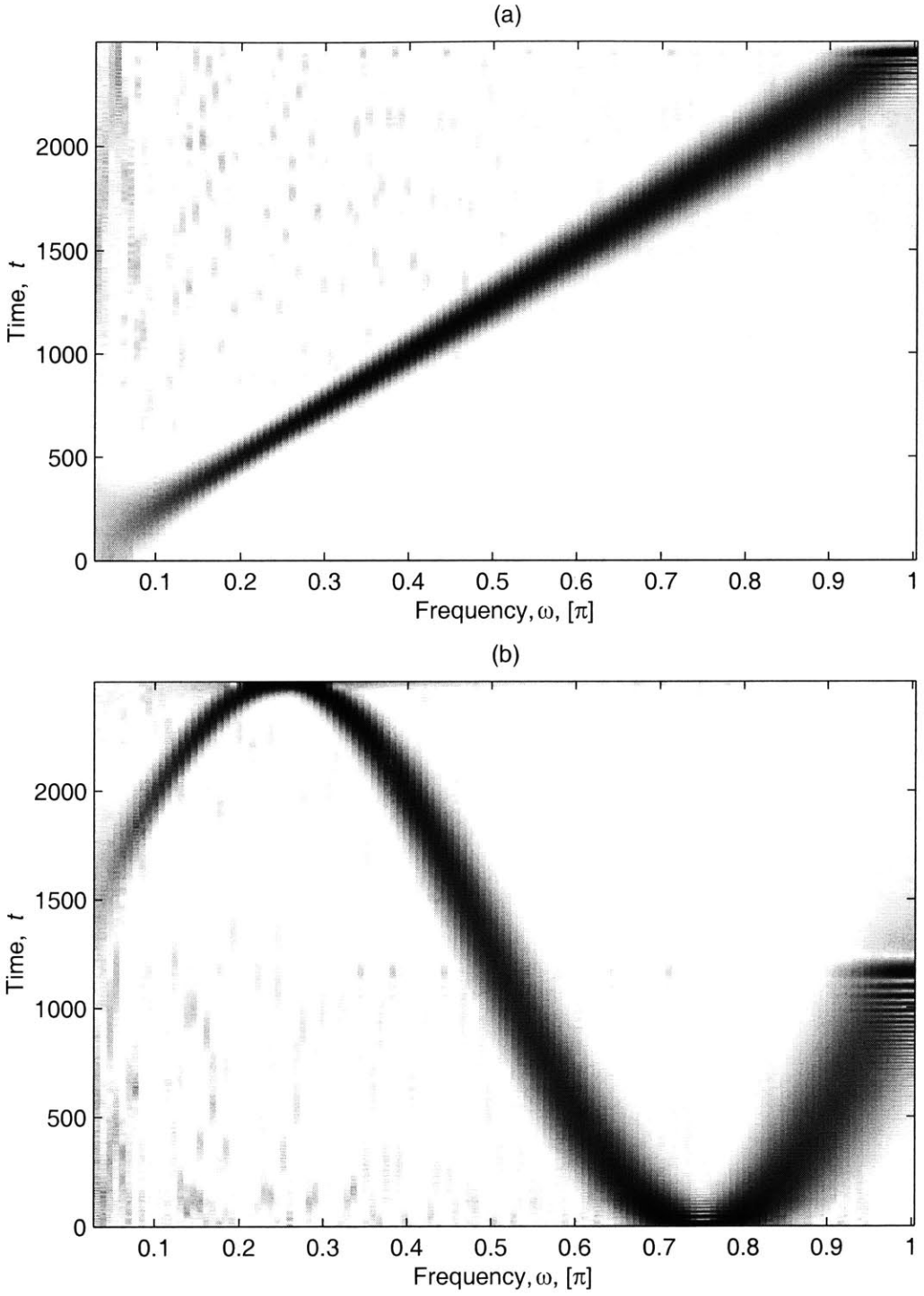

Figure 4-12: Image of wavelet coefficients for (a) Signal 1, $\alpha = 20$ and (b) Signal 3, $\alpha = 20$.

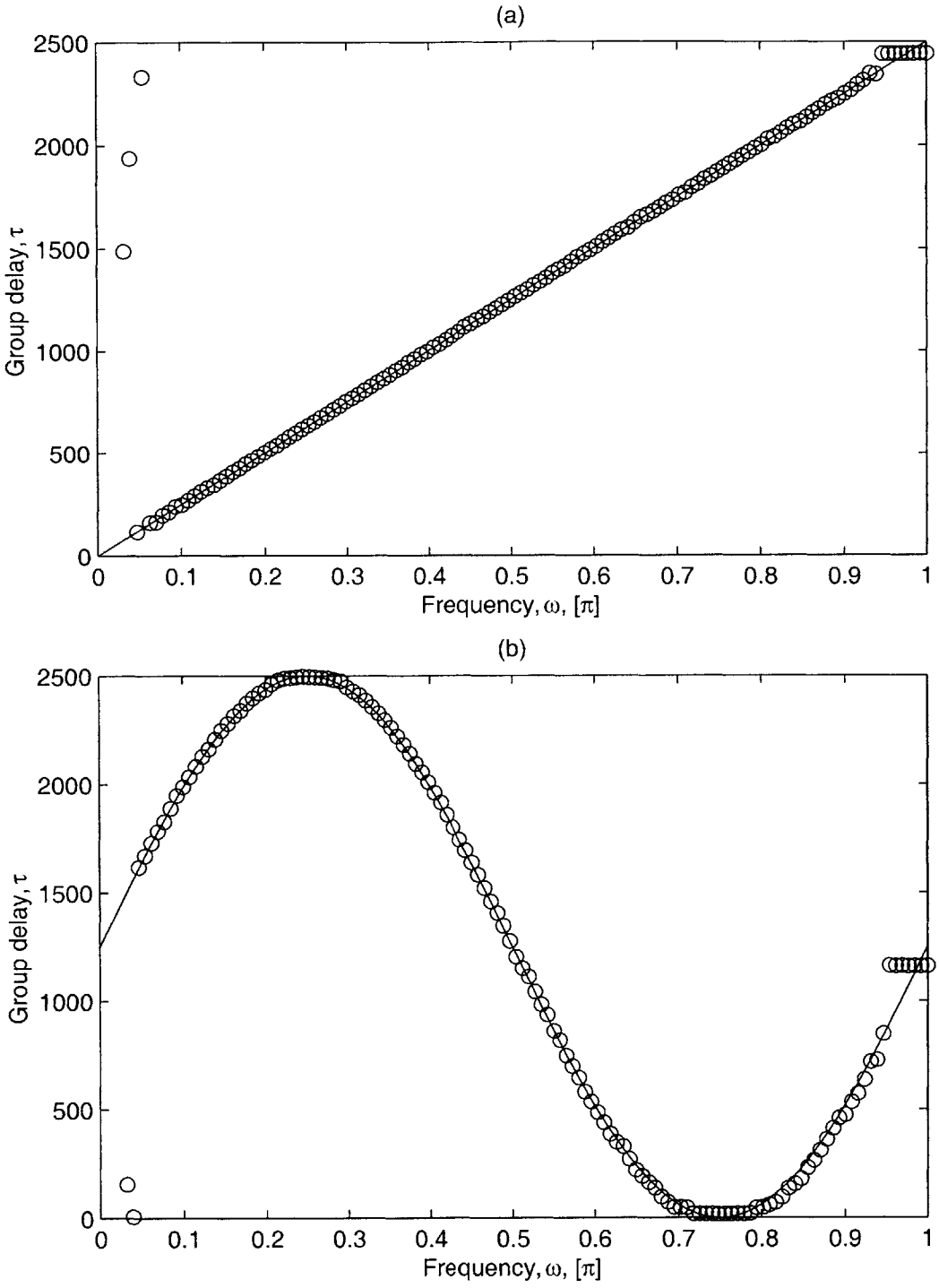

Figure 4-13: Comparison between the actual and calculated group delay for (a) Signal 1, $\alpha = 20$ and (b) Signal 3, $\alpha = 20$.

Results for $\alpha = 50$

As α is increased further, the results exhibit better accuracy in the high frequency range but deteriorates for lower frequencies. The images of the WT coefficients in Fig. 4-14 show sharper patterns, but a greater amount of noise is also present. The decrease in accuracy for lower frequencies is more evident in the group delay plots in Fig. 4-15.

Average error vs. frequency

To further illustrate the dependence of errors on frequency, the absolute error for each test is calculated and averaged over all four test signals. The results for $\alpha = 4, 20$ and 50 are shown in Fig. 4-16.

4.3.6 Remarks

In this section, the overall or cumulative error was investigated for a wide range of values of α with ω_o held constant at $\pi/2$. The results seem to reveal that there is only a certain range of α for which the group delay can be calculated with an acceptable degree of accuracy. Extremely low values of α lead to wavelets whose bandwidth is much too wide and to results with very poor accuracy. Although higher values of α yield sharper peaks in the WT coefficients, they also incur a greater computational expense.

Furthermore, plots of the calculated group delay for a certain value of α show that the errors are not uniformly distributed over frequency. It seems that for a certain value of α, there is a finite frequency band in which the wavelet yields accurate results. It was also found that at approximately $\alpha = 20$, the accuracy is poor only for extreme low and extreme high frequencies, and is very good otherwise. Since, for most experimental signals, the extremely low ($f \approx 0$) and extremely high ($f \approx$ Nyquist frequency) are of little significance, the value of α to be used in the following simulations as well as in analyzing the experimental results is 20.

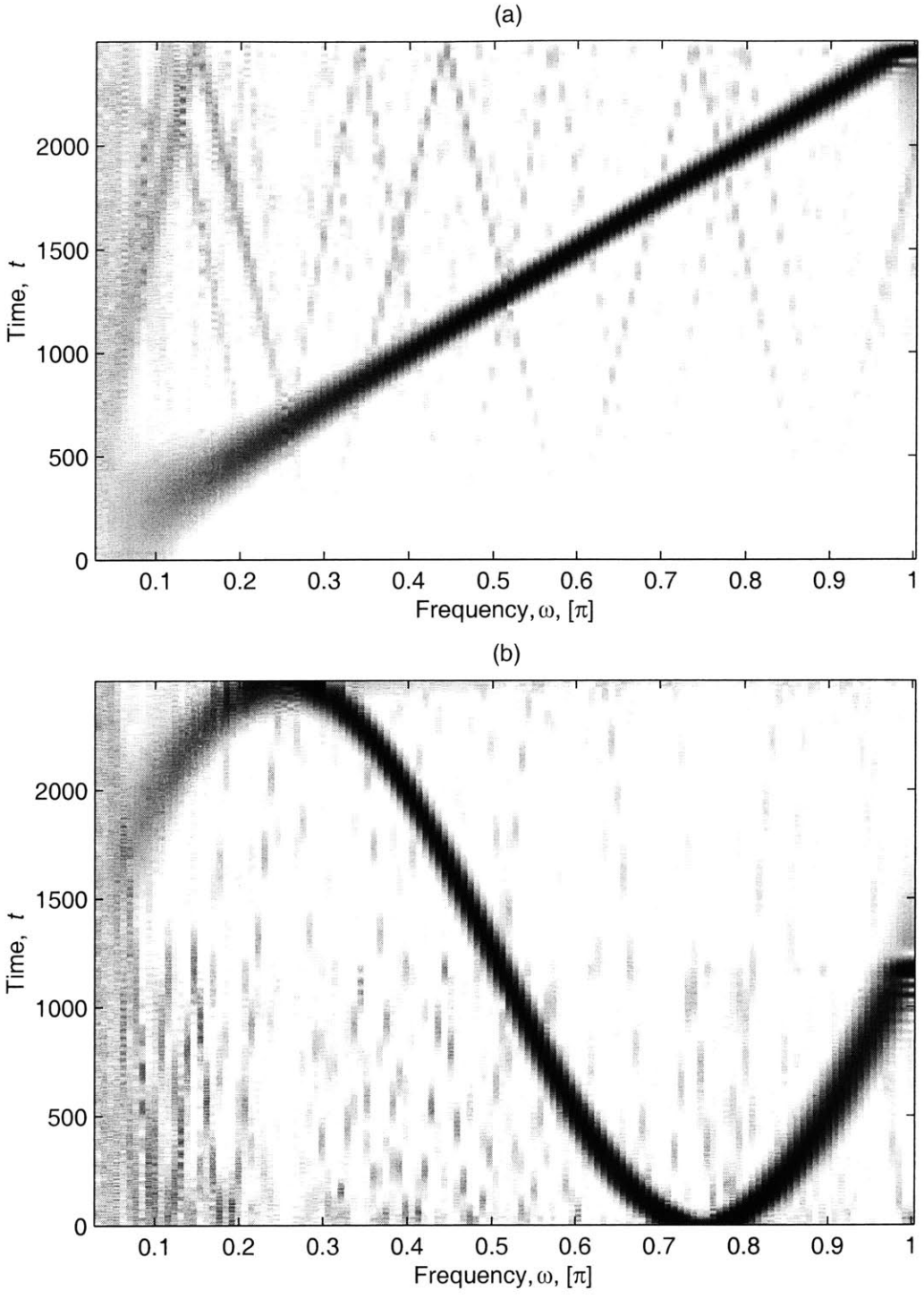

Figure 4-14: Image of wavelet coefficients for (a) Signal 1, $\alpha = 50$ and (b) Signal 3, $\alpha = 50$.

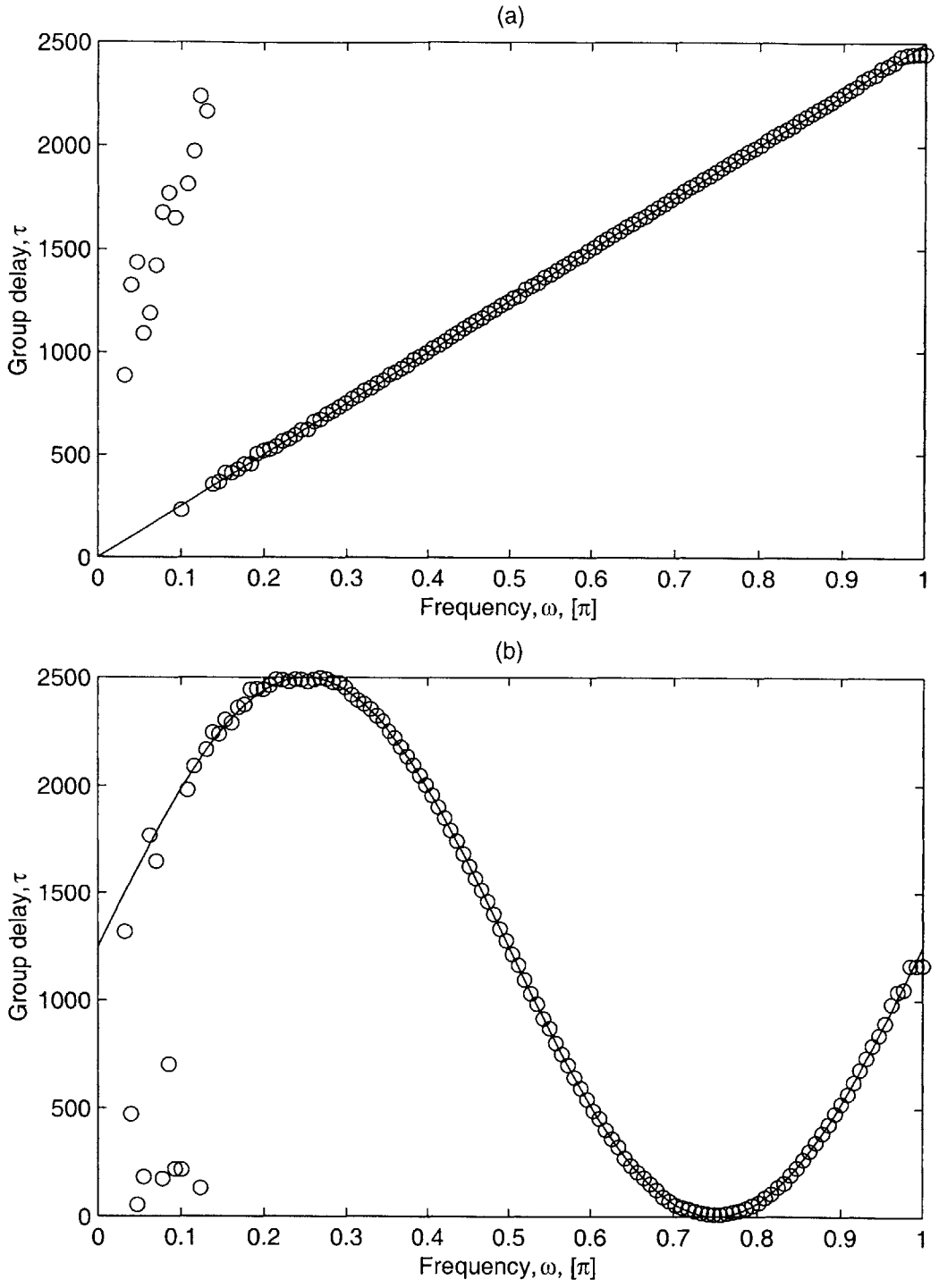

Figure 4-15: Comparison between the actual and calculated group delay for (a) Signal 1, $\alpha = 50$ and (b) Signal 3, $\alpha = 50$.

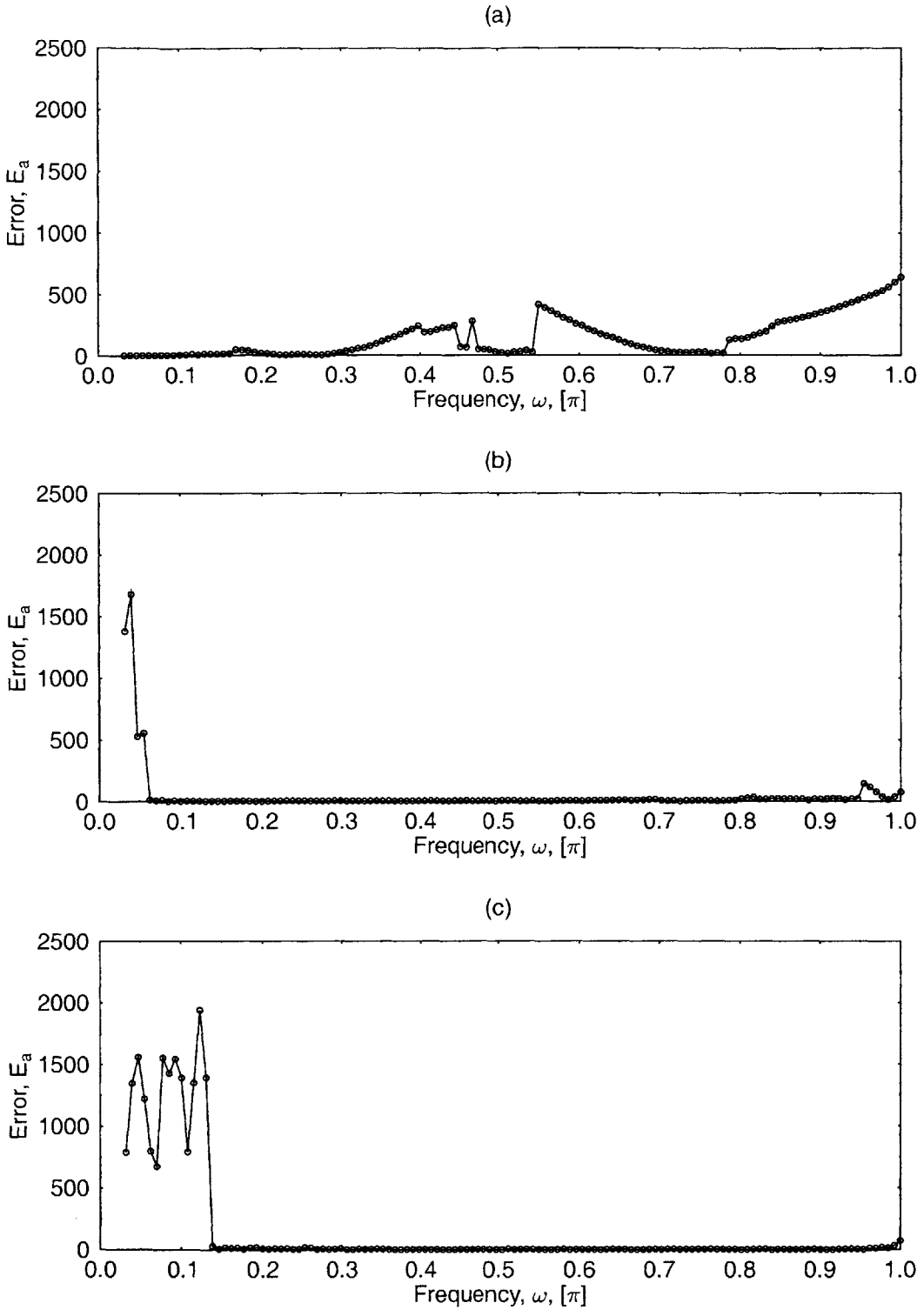

Figure 4-16: Average absolute error in the calculated group delay plotted as a function of frequency ω for (a) $\alpha = 4$, (b) $\alpha = 20$ and (c) $\alpha = 50$.

4.4 Multimode Signals

4.4.1 Test Signals

As stated previously, only the results for $\alpha = 20$ will be presented. Just as for the single mode signals, the multimode signals to be considered in the following simulations have the characteristics put forth in Table (4.1). The two multimode signals are obtained from the four test signals used previously. In particular, Signals 5 and 6, both containing two modes, are defined as

$$h_5(t) = h_1(t) + h_2(t) \tag{4.12}$$

$$h_6(t) = h_3(t) + h_4(t) \tag{4.13}$$

where $h_n(t)$ denotes the impulse response corresponding to Signal n. Hence, Signal 5 is the superposition of two signals with linear group delay, while Signal 6 is the superposition of two signals with sinusoidal group delay. The phase response and group delay for $h_n(t)$, with $n = 1 \ldots 4$ were given previously in Table (4.2). Signals 5, 6 and their corresponding two-mode dispersion curves are shown in Figs. 4-17 and 4-18 respectively.

4.4.2 Group Delay Measurement Algorithm

Figure 4-19(a) and Fig. 4-19(b) show the magnitude of the wavelet transform coefficients $W(a, b)$ evaluated at $\omega = \pi/3$ for Signals 5 and 6 respectively. The presence of two dominant modes is evident, but the ghost peaks observed in previous simulations still occur. It is also important to note the presence of local oscillations in the coefficients. Since the algorithm searches for the maxima in the coefficients, these local maxima may also be interpreted erroneously as modes.

An obvious extension of the extraction algorithm in Fig. 4-5 is to take the M highest peaks when M modes are being sought. However, a way must be found so as not to mistake the local peaks for actual modes. One option would be to de-noise the WT coefficients in order to be rid of the local oscillations. Another option, and one which will be explored further in this study, is to use a thresholding scheme.

This thresholding scheme is based on the observation that there exists a minimum separation between two modes that the algorithm can detect. As an example, the wavelet

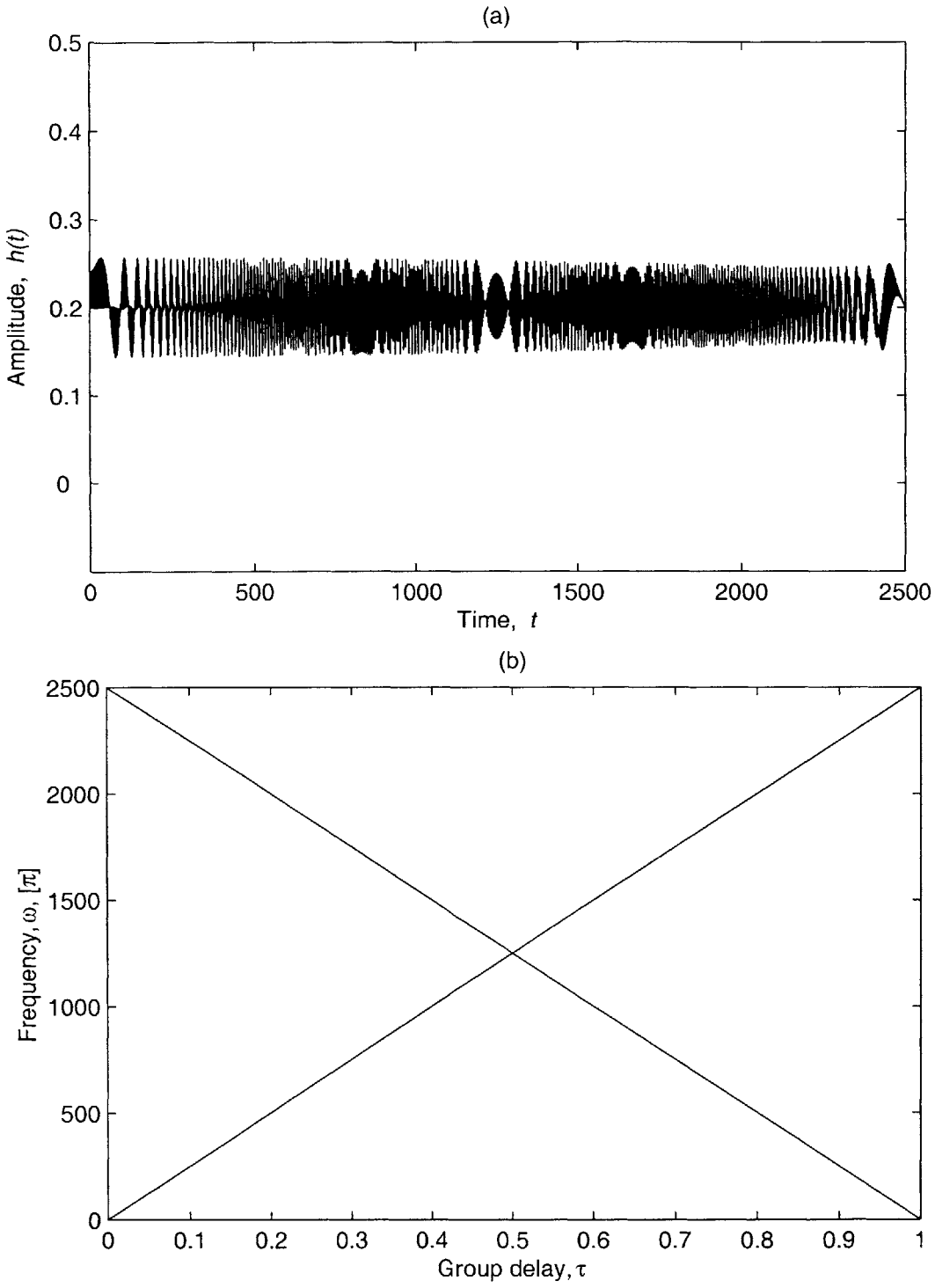

Figure 4-17: Signal 5: (a) Impulse response and (b) actual group delays, $\tau(\omega)$.

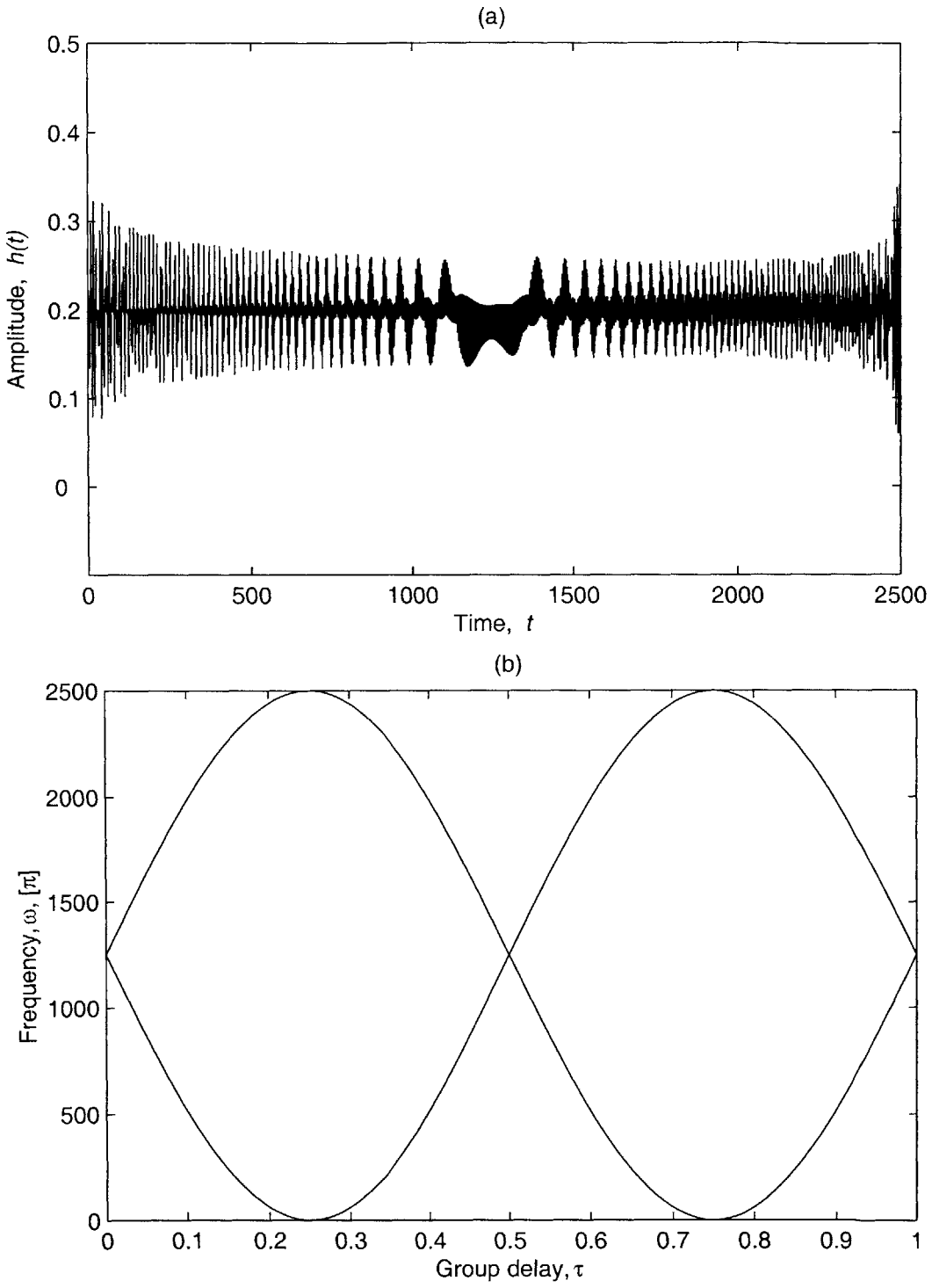

Figure 4-18: Signal 6: (a) Impulse response and (b) actual group delays, $\tau(\omega)$.

coefficients at $\omega = 0.47\pi$ for Signals 5 and 6 are shown in Fig. 4-20. This frequency was chosen for its close proximity to $\omega = \pi/2$, which corresponds to the crossing point in the dispersion curves (Figs. 4-17 and 4-18).

Consider for instance the sample coefficients shown in Fig. 4-21. The local maxima have been detected and are also shown . The coefficients exhibit one dominant mode at t_3 and another lower magnitude mode at t_9 with some noise around each one. An obvious extension of the method for single mode signals would simply be to choose the highest M peaks to correspond to M modes (in this case 2). We could sort the array according to the magnitude of the coefficients, also shown in Fig. 4-21. The group delay for M modes can then be determined by choosing the first M maxima. In this example we would choose t_4 and t_{11}.

Generally however, the calculated coefficients will not be as smooth as those shown in the previous examples and may exhibit some high frequency, low magnitude oscillations. These oscillations may result in erroneous measurements. One option in addressing the problem is to use thresholding, i.e. requiring that the distance between 2 modes must be greater than a certain value. This is equivalent to assuming that there is a minimum separation which the algorithm can detect.

4.4.3 Results

The images of the WT coefficients for Signals 5 and 6 are shown in Fig. 4-22. The dispersion patterns of the two modes can be clearly seen in these images. Next, the results of the extraction algorithm without thresholding are shown in Figs. 4-23(a) and 4-24(a). The large errors resulting from the presence of local maxima may be seen in these plots, and are even more evident in Figs. 4-25 and 4-26. In the region of $\omega = \pi/2$, the minimum separation T_{min} that the algorithm is able to detect is also evident. The average values of T_{min} for the two signals are summarized in Table (4.4).

Using the average minimum separation T_{min} as the threshold in the algorithm, leads to a large improvement in accuracy. Figs. 4-23(b) and 4-24(b) show the results of the extraction algorithm with thresholding. The absolute error plots in Figs. 4-25 and 4-26 exhibit a great decrease in the error compared to the results without thresholding.

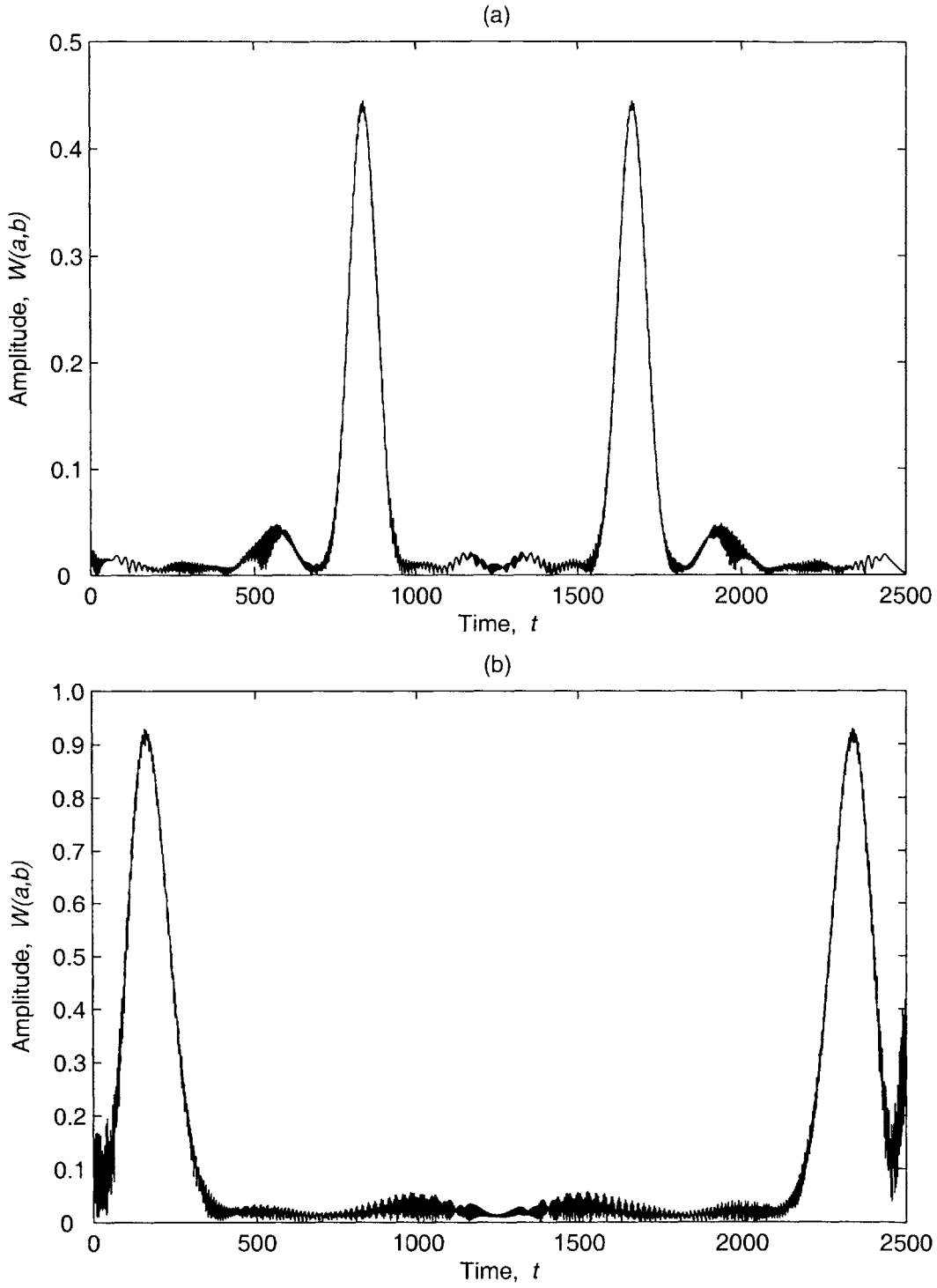

Figure 4-19: Sample coefficients at $\omega = \pi/3$ showing two distinct peaks for (a) Signal 5 and (b) Signal 6.

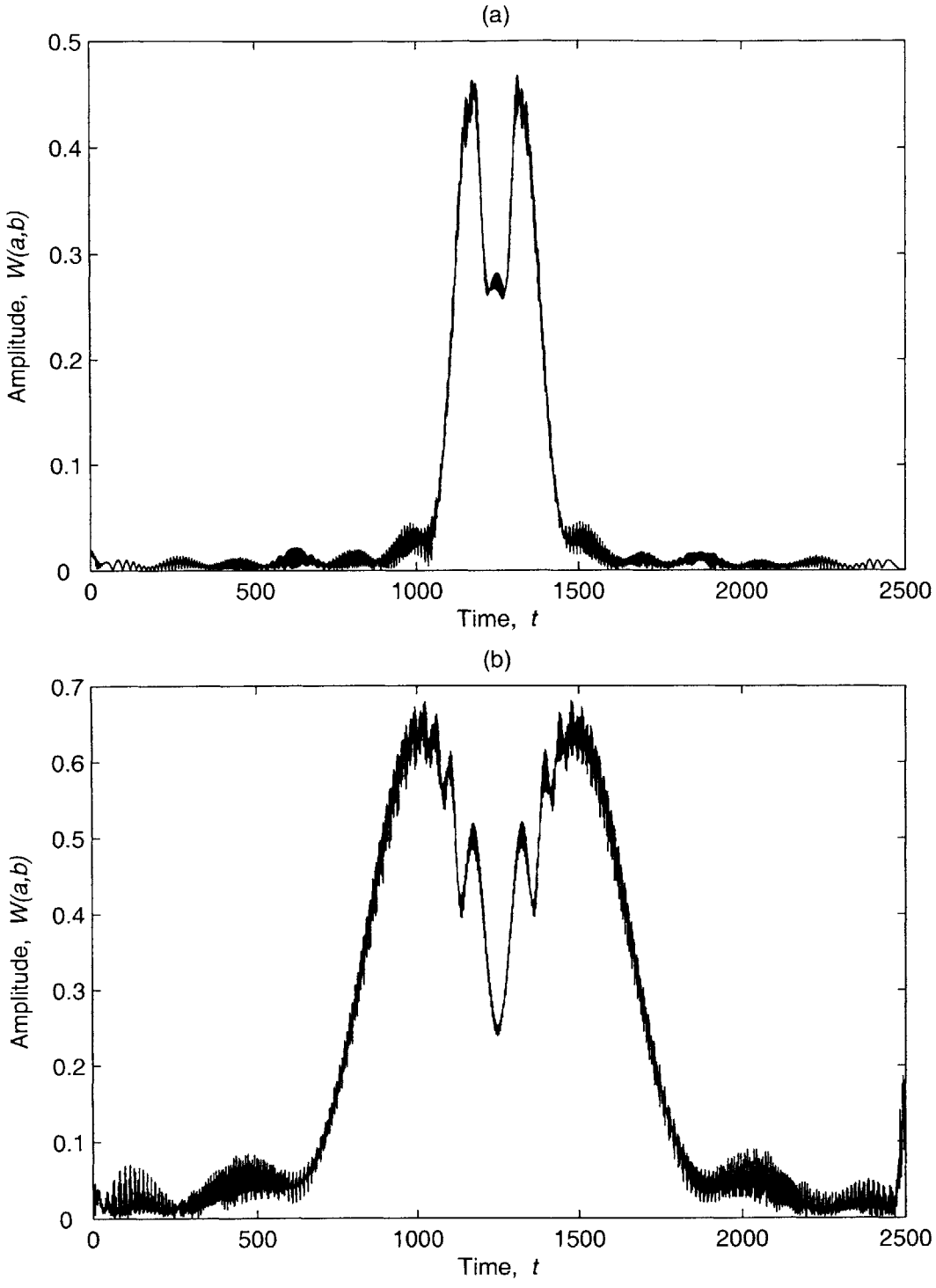

Figure 4-20: Sample coefficients at $\omega = 0.47\pi$ showing the merging of the two peaks corresponding to the two modes for (a) Signal 5 and (b) Signal 6.

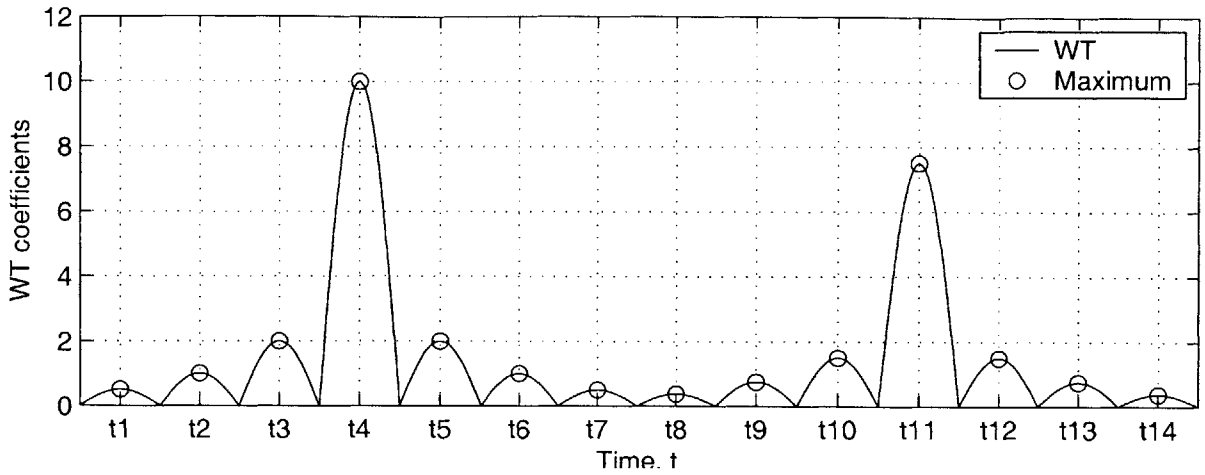

Location	t_4	t_{11}	t_3	t_5	t_{10}	...
Magnitude	10	7.5	2	2	1.5	...

Figure 4-21: Measuring the group delay for a two-mode signal. The locations of the maxima are sorted according to the magnitude of the WT coefficients.

	Minimum separation, T_{min}
Signal 5	118
Signal 6	133

Table 4.4: Minimum separation detectable by the algorithm.

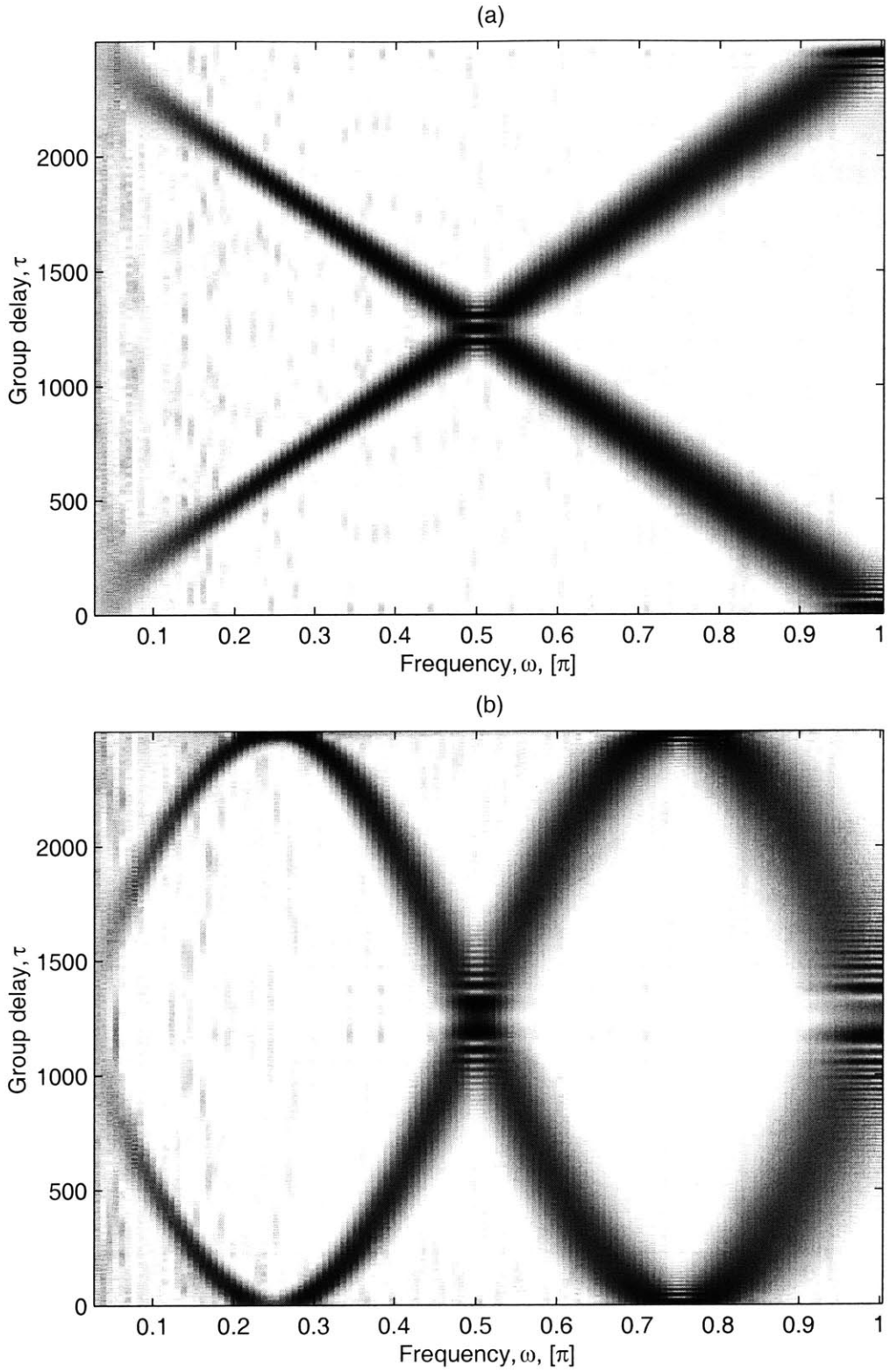

Figure 4-22: Image of wavelet coefficients for (a) Signal 5, $\alpha = 20$ and (b) Signal 6, $\alpha = 20$.

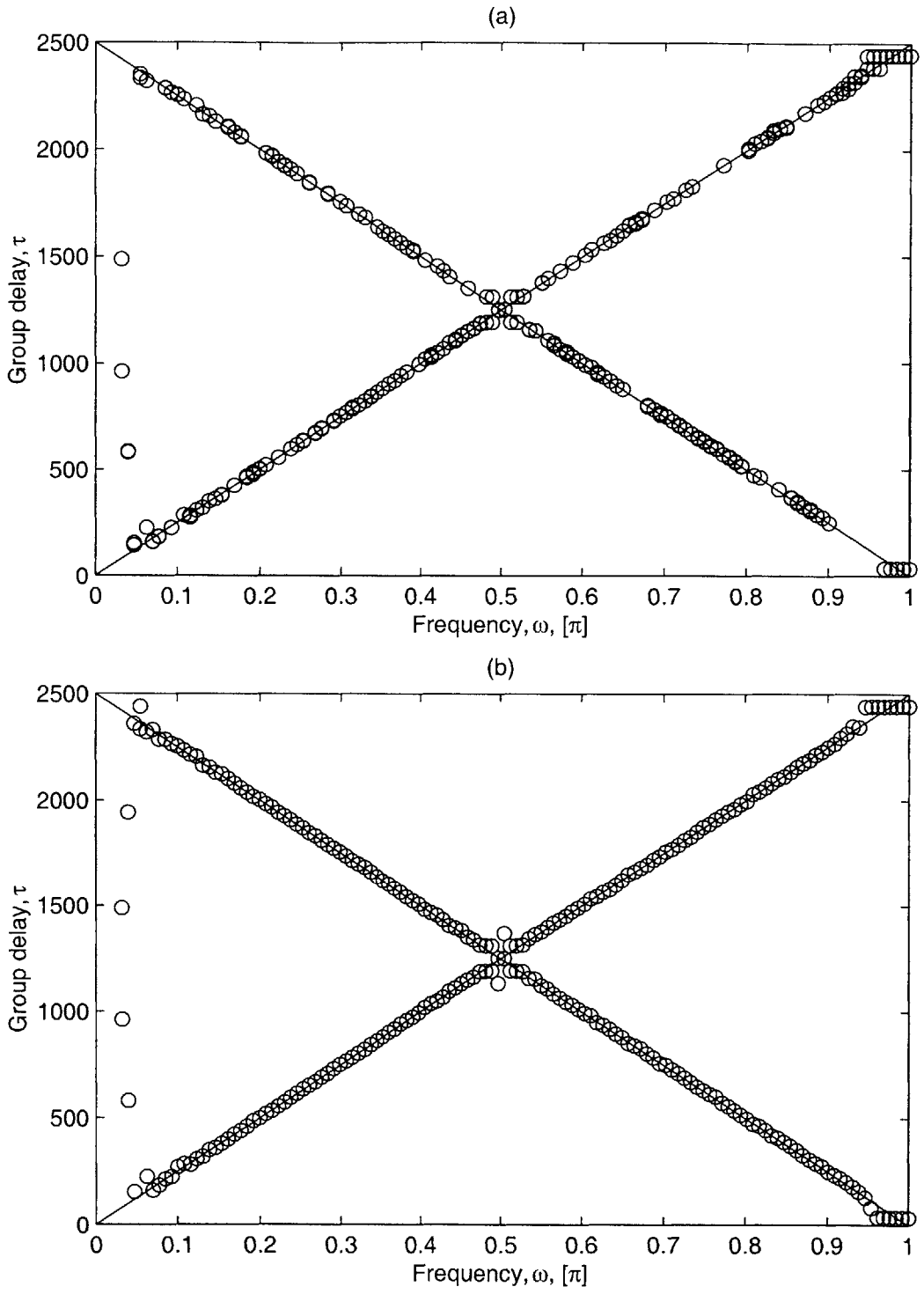

Figure 4-23: Comparison between the actual and calculated group delay for Signal 5 (a) without thresholding and (b) with thresholding.

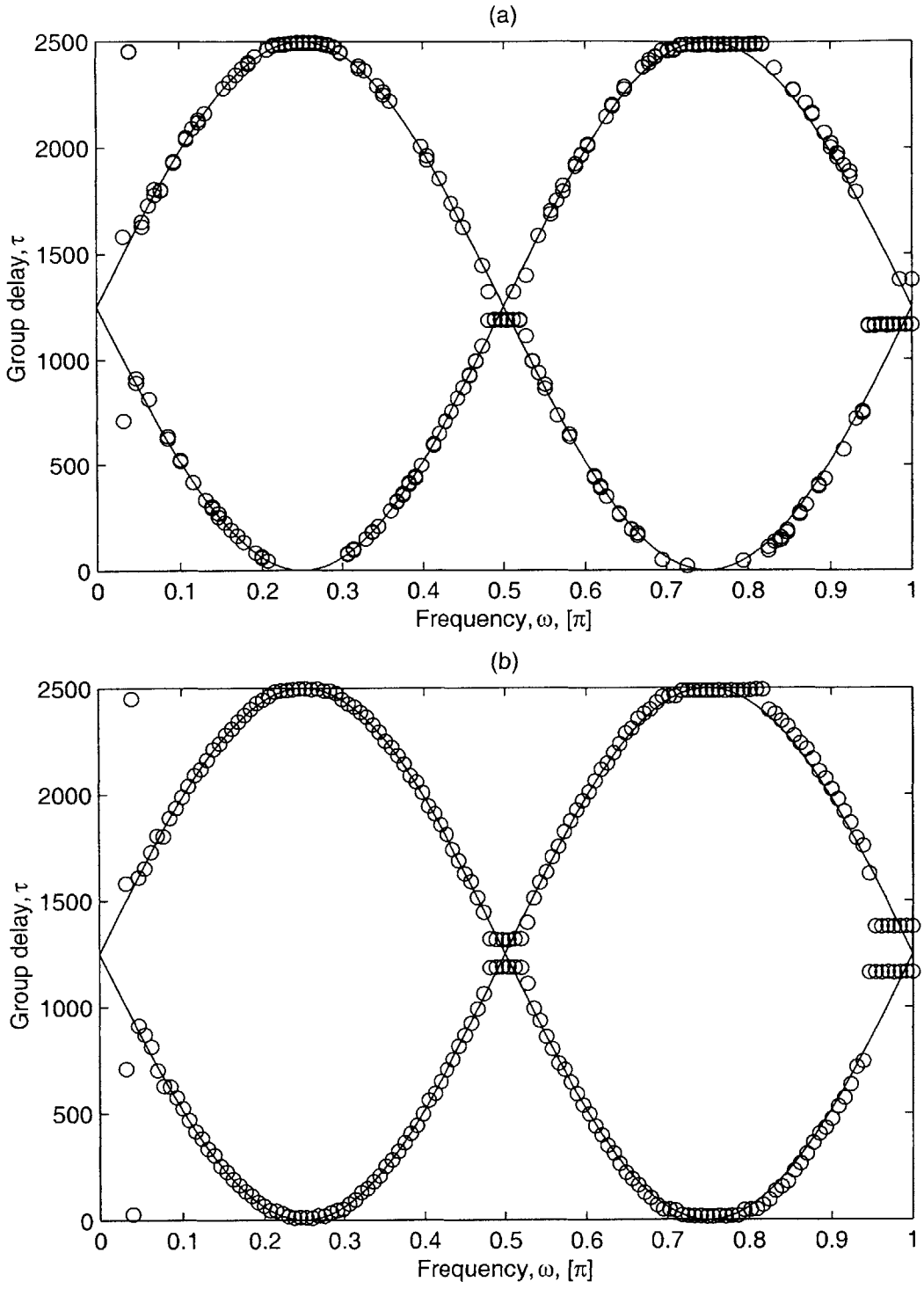

Figure 4-24: Comparison between the actual and calculated group delay for Signal 6 (a) without thresholding and (b) with thresholding.

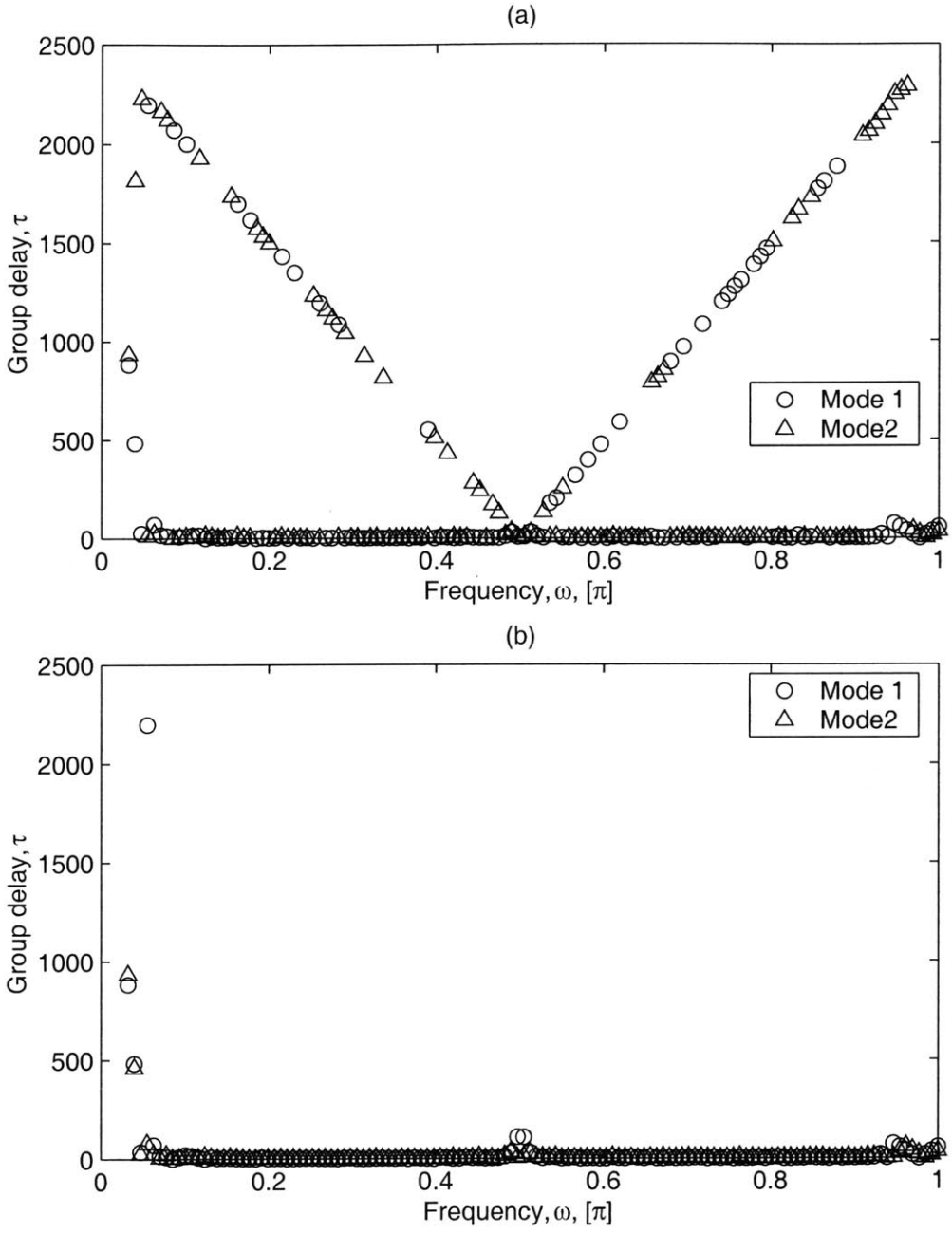

Figure 4-25: Absolute error, E_a, for Signal 5 (a) without thresholding and (b) with thresholding.

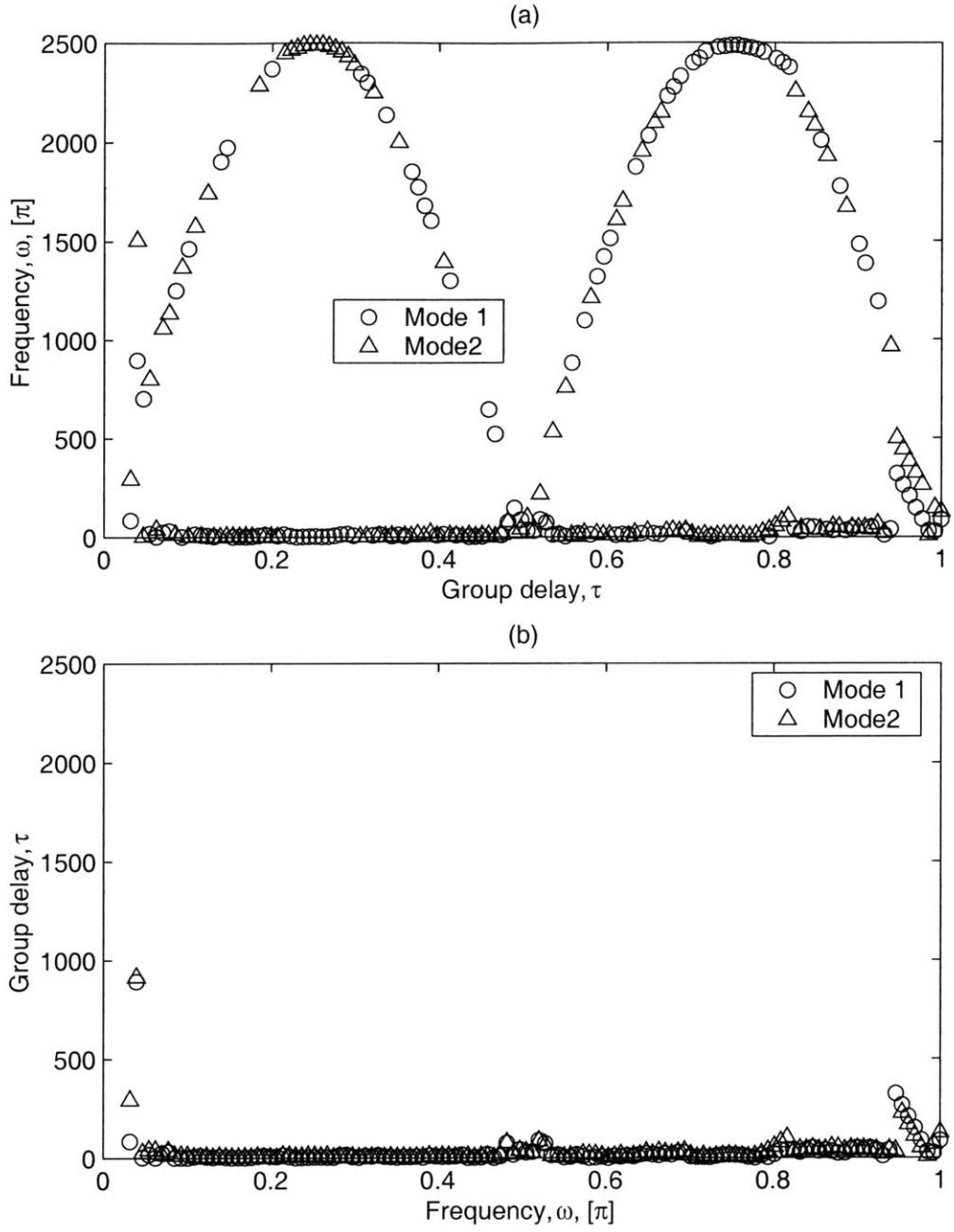

Figure 4-26: Absolute error, E_a, for Signal 6 (a) without thresholding and (b) with thresholding.

4.4.4 Remarks

Several problems were encountered in attempting to measure the group delay of several modes from the WT coefficients. One problem is the presence of local peaks, especially those in the vicinity of a main peak corresponding to an actual mode arrival. These local peaks may be erroneously interpreted as mode arrivals. Another problem is the existence of crossing points in the dispersion curves. These crossing points represent modes which arrive at the same time. It was very difficult to separate two modes in the vicinity of a crossing point.

It was observed that there is a minimum separation, i.e., a minimum time interval between the arrival of any two modes, that the method is able to detect. Using this fact, a revised algorithm was made which addresses the problem of the presence of local peaks. This algorithm detected the two modes in the simulated signals with good accuracy except for the extremely low and high frequencies.

In the next chapter, this algorithm will be applied to experimental signals.

Chapter 5

Experimental Results

5.1 Introduction

In Chapter 4, the method was applied to simulated signals. An algorithm was developed which analyzes multimode signals and constructs the dispersion curves with good accuracy. In this chapter, the method will be used to analyze experimental signals.

5.2 Experimental Set-up

The actual experimental set-up used to generate and measure Lamb waves is shown in Fig. 5-1. A pulsed Nd:YAG laser was used to generate ultrasound in an aluminum plate at a distance d_L from the receiver (Fig. 5-2). To increase the intensity of the laser generated source, a focusing lens was placed in the beam path and the plate was positioned at the focal point of the lens. Transducers made of polyvinylidene fluoride (PVDF) were coupled to the plate to receive the Lamb wave signals. The elastic properties and dimensions of the aluminum plate are summarized in Table (5.1). The received signals were amplified and then recorded for analysis. More detailed specifications for the laser, PVDF transducer, amplifier, and data acquisition equipment may be found in Appendix A.

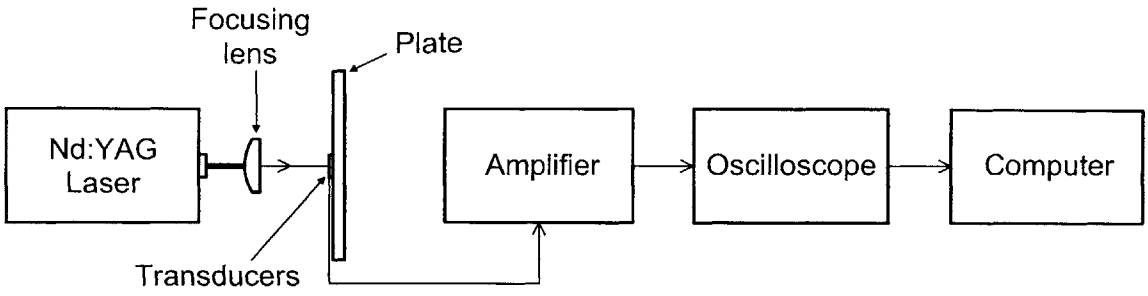

Figure 5-1: Diagram of the experimental set-up.

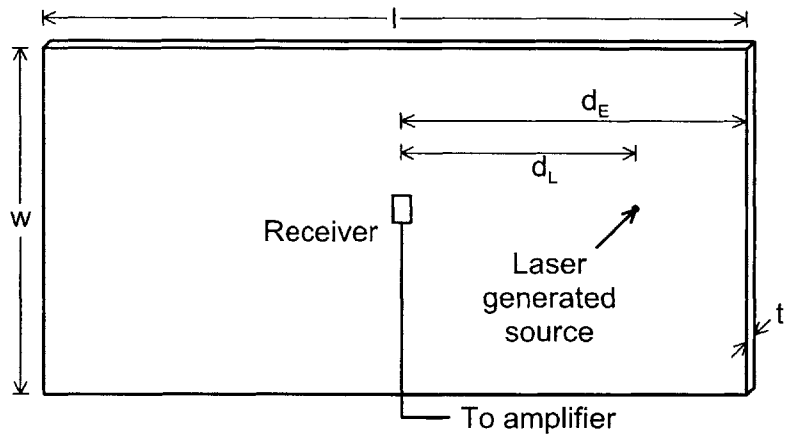

Figure 5-2: Dimensions of the aluminum plate and positioning of the transducers.

Property	Value	Units
Young's Modulus	70	GPa
Density	2700	kg/m^3
Poisson's ratio	0.35	-
d_E	39	cm
w	46	cm
l	92	cm
t	0.065	mm

Table 5.1: Dimensions of the aluminum plate used in experiments, and the elastic properties used in making theoretical predictions.

5.3 Data and Analysis

5.3.1 Results for $d_L = 25$ cm

The laser beam was first directed at a point on the aluminum plate a distance $d_L = 25$ cm from the receiving transducer. The received signal (Fig. 5-3) was sampled at a frequency of 10MHz, averaged 64 times, amplified, then recorded for analysis. Fig. 5-4 shows the wavelet coefficients for the frequency range 0.1 MHz to the Nyquist rate of 5 MHz. The image of wavelet coefficients reveal the presence of approximately six dispersion curves present in the signal. The upper three curves are shifted versions of the lower three, indicating that they may correspond to secondary arrivals of the same Lamb modes. The low frequency, nondispersive components in the frequency range $0.5-2$ MHz are dominant, i.e., the wavelet coefficients are highest in this range.

The group delay determined from the wavelet transform coefficients are plotted in Fig. 5-5 and show very good agreement with the theoretical predictions. For $f = 0.1-1.0$ MHz, the A_0 is dominant. For $f = 1.0-2.5$ MHz, both the A_0 and S_0 are easily distinguishable, and the dispersion curves constructed from the calculated group delay agree very well with the theoretical values. The results for $f = 2.5-3.5$ MHz illustrate the difficulties encountered

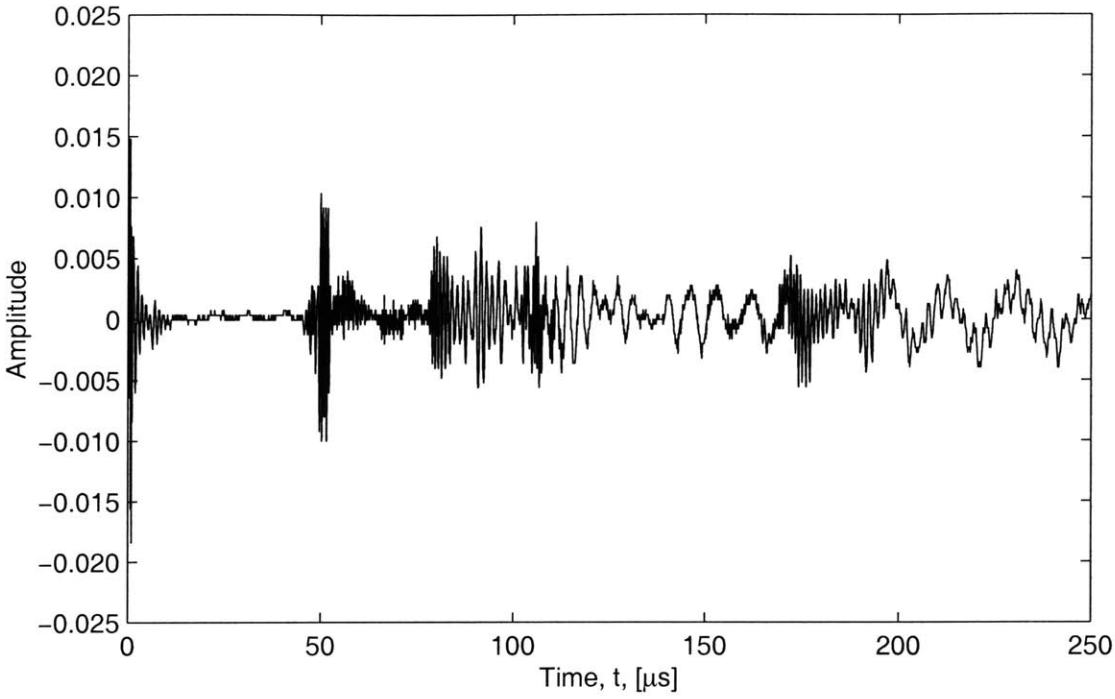

Figure 5-3: Received signal with the laser generated source located at a distance $d_L = 25$ cm from the receiving transducer.

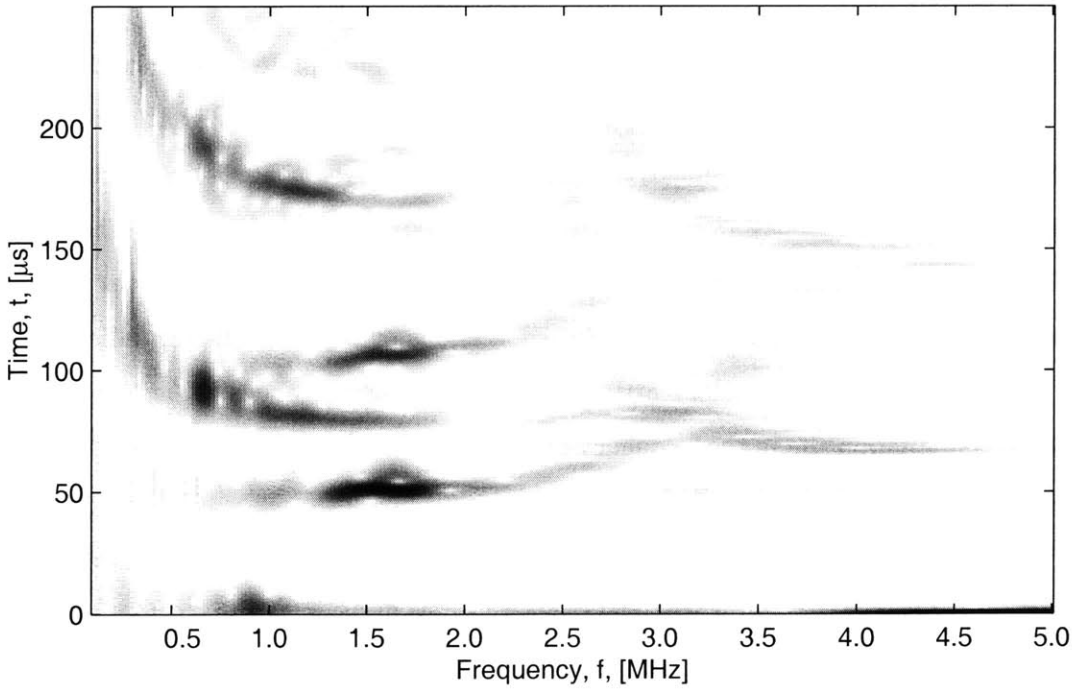

Figure 5-4: Wavelet coefficients of the received signal for 0.1 to 5 MHz.

when the dispersion curves intersect. Finally, for $f = 3.5-5$ MHz, the A_1 and A_1' modes were constructed with reasonably good accuracy. The A_0 mode, although not easily observable in the image of wavelet coefficients (Fig. 5-4), was also determined to good accuracy. A pattern which vaguely resembles that of the S_0 mode may also be observed, however it is not entirely distinct.

To further illustrate how the data in Fig. 5-5 was obtained, the wavelet transform coefficients at several frequencies is plotted. Figure 5-6 shows the coefficients at $f = 1.25$ MHz. The first two arrivals marked S_0 and A_0 correspond to the direct arrival from the laser generated source. The second two arrivals marked S_0' and A_0' correspond to the waves reflected from the edge of the plate. Note that although the S_0' mode has a lower magnitude than the direct arrival, the A_0' mode has a slightly higher magnitude than the A_0 mode. This seems to go against the expectation that the reflected waves would have attenuated much more than the direct waves. However, it is likely that this phenomenon is due to the mode conversion which occurred when the waves were reflected from the edge [24]. The mode conversion would result in the exchange of energies between the symmetric and antisymmetric mode, making the magnitude of the A_0' mode greater.

The wavelet transform coefficients at $f = 4.0$ MHz are also plotted in Fig. 5-7. Although much weaker than the fundamental antisymmetric and symmetric modes, the direct and reflected antisymmetric modes (A_1 and A_1' respectively) are also observable.

Using the group delay of the direct and reflected waves, the distance between the receiving transducer and the plate edge may be determined. The distance traveled by the reflected waves is

$$x = 2d_E - d_L. \tag{5.1}$$

Denoting the group delay corresponding to the direct and reflected waves by $\tau_L(\omega)$ and $\tau_E(\omega)$ respectively, the distance between the receiver and the plate edge is given by

$$d_E = \frac{1}{2} d_L \left[\frac{\tau_E(\omega)}{\tau_L(\omega)} + 1 \right]. \tag{5.2}$$

Using the results for $1.0 - 1.5$ MHz for which the dispersion curves are well defined, the distance d_E was calculated and plotted in Fig. 5-8. The values plotted are the average between the results for the symmetric and antisymmetric modes.

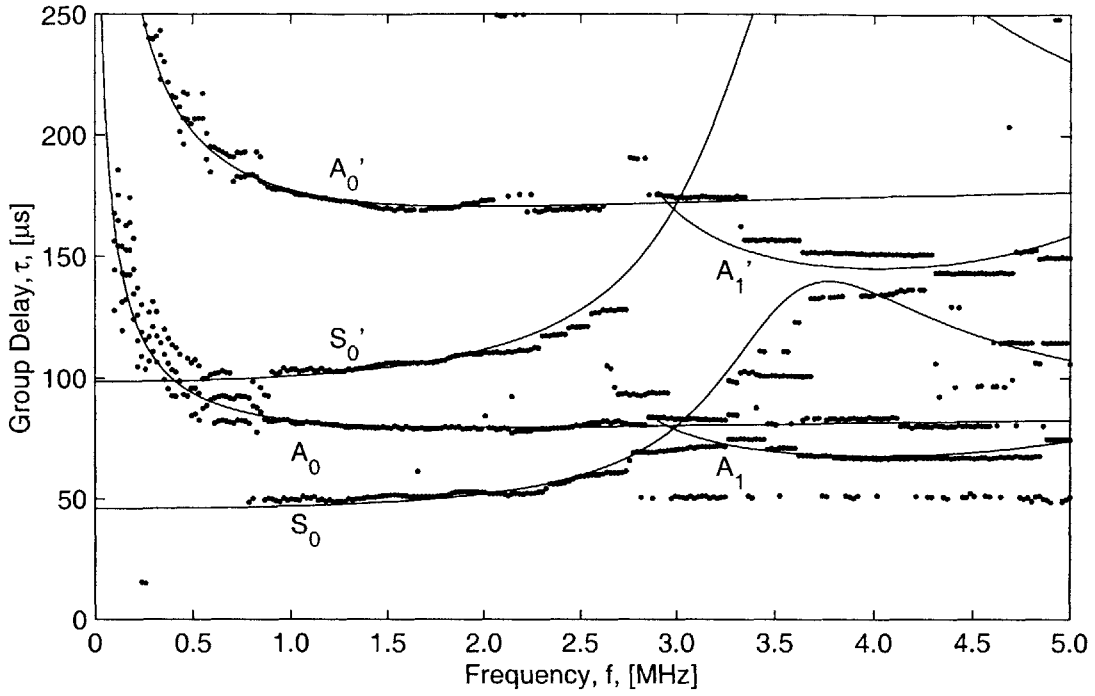

Figure 5-5: Group delay determined from the wavelet transform coefficients.

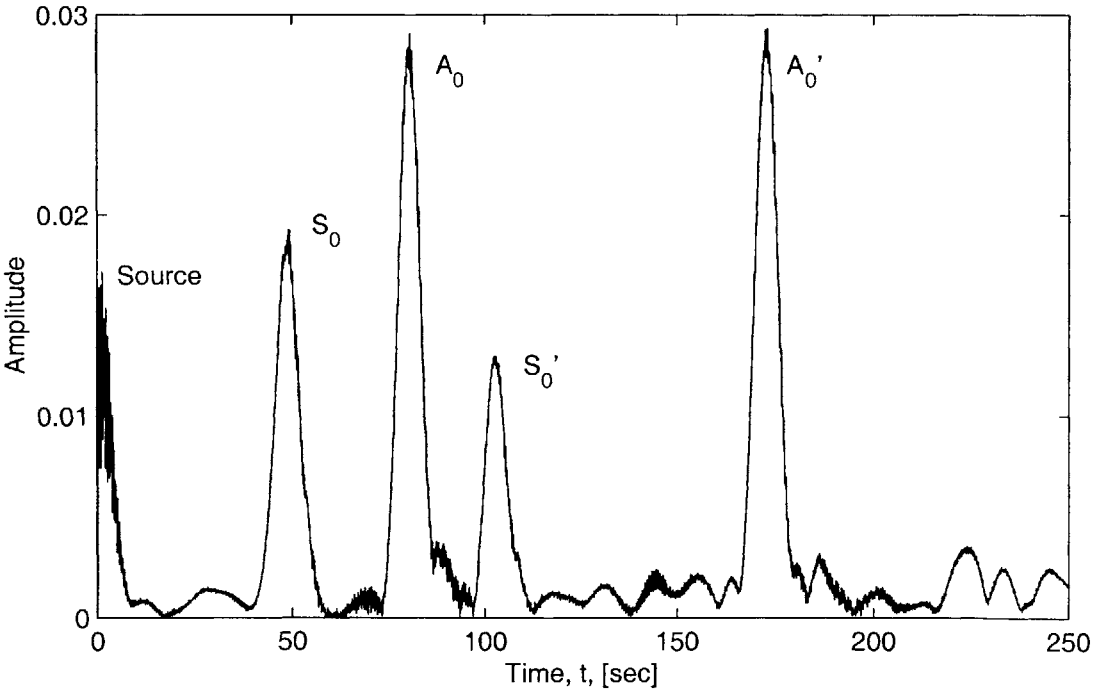

Figure 5-6: Wavelet coefficients of the received signal for $f = 1.25$ MHz.

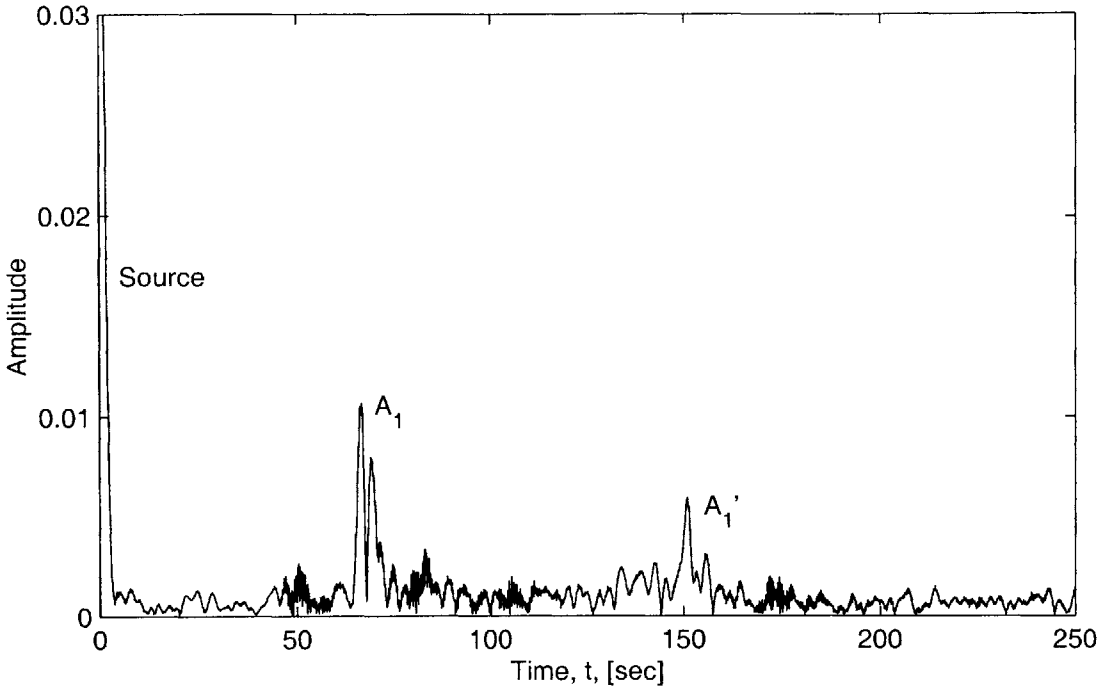

Figure 5-7: Wavelet coefficients of the received signal for $f = 4$ MHz.

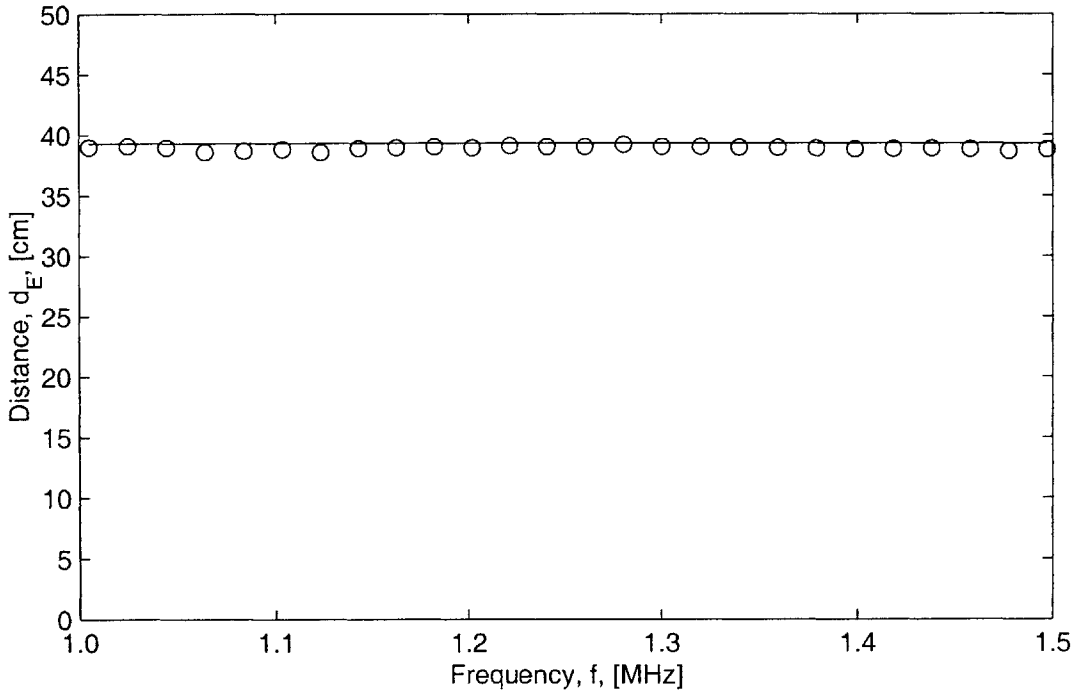

Figure 5-8: Measured distance between the receiving transducer and plate edge, compared with the actual distance (indicated by the solid line).

5.3.2 Other Results

Figures Fig. 5-9 to Fig. 5-18 show the results for $d_L = 15 - 24$ cm. These results are consistent with those for $d_L = 25$ cm, and the distance between the transducer and the edge is determined with good accuracy in all trials.

5.4 Remarks

The results presented in this chapter confirm the difficulties in dealing with crossing points in the dispersion curves. Furthermore, the algorithm used still required a subjective decision as to how many modes are to be measured from the signal. Nevertheless, the method is relatively good in that the dispersion curves were constructed by measuring the group delay for a wide range of frequencies from a *single* signal. This characteristic makes this method particularly suitable for quick tests, where some reduction in accuracy may be tolerated.

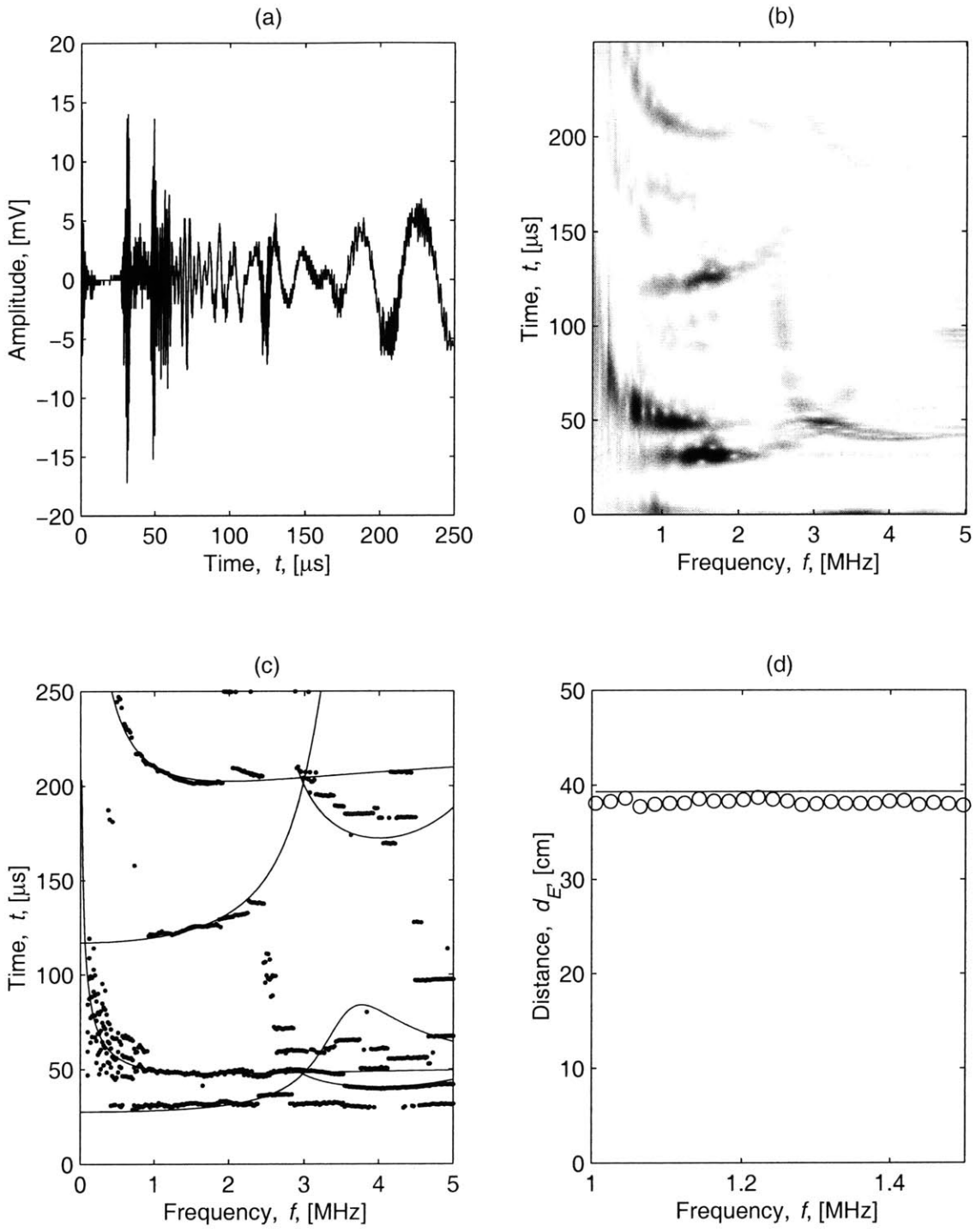

Figure 5-9: Experimental results for $d_L = 15$ cm.

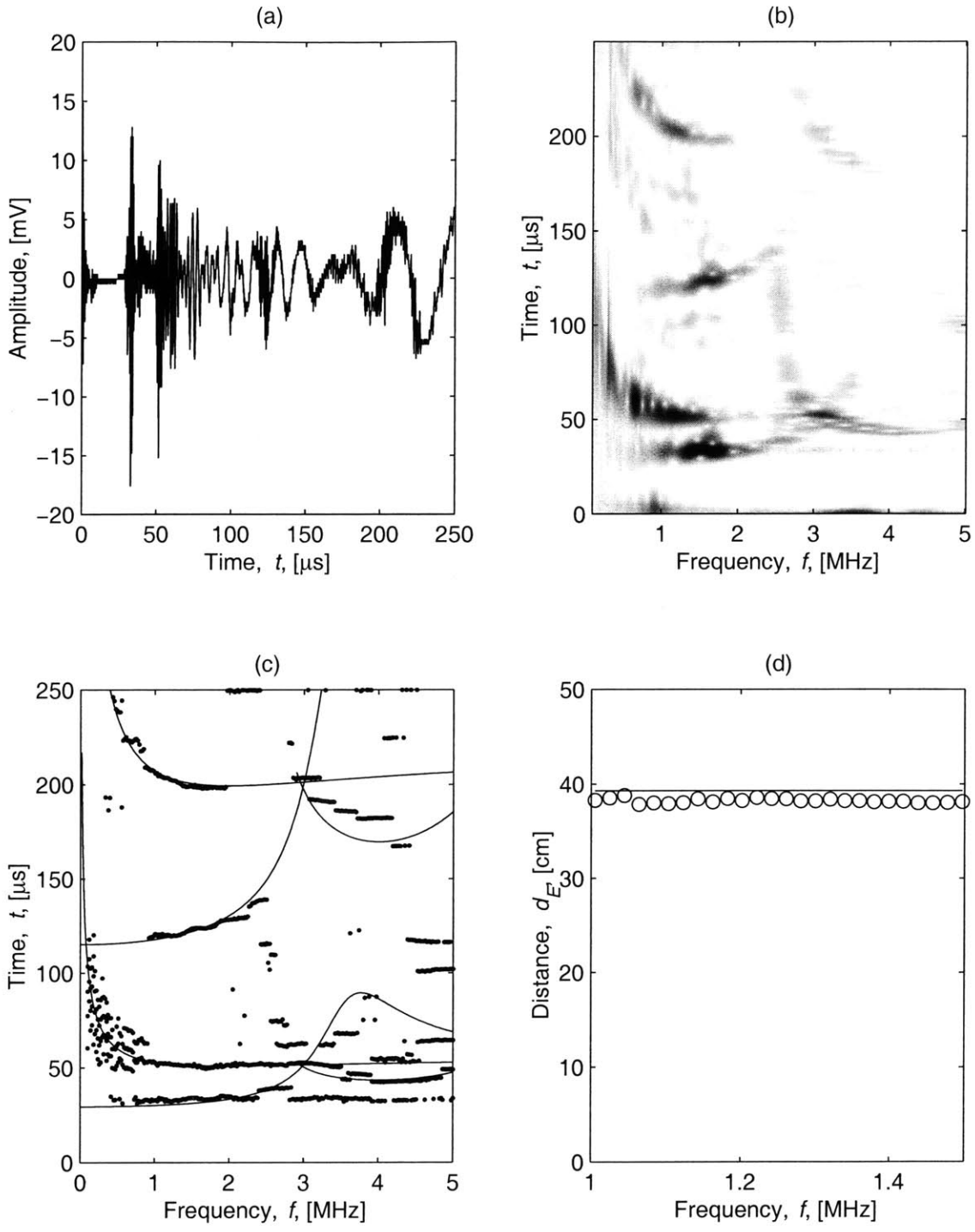

Figure 5-10: Experimental results for $d_L = 16$ cm.

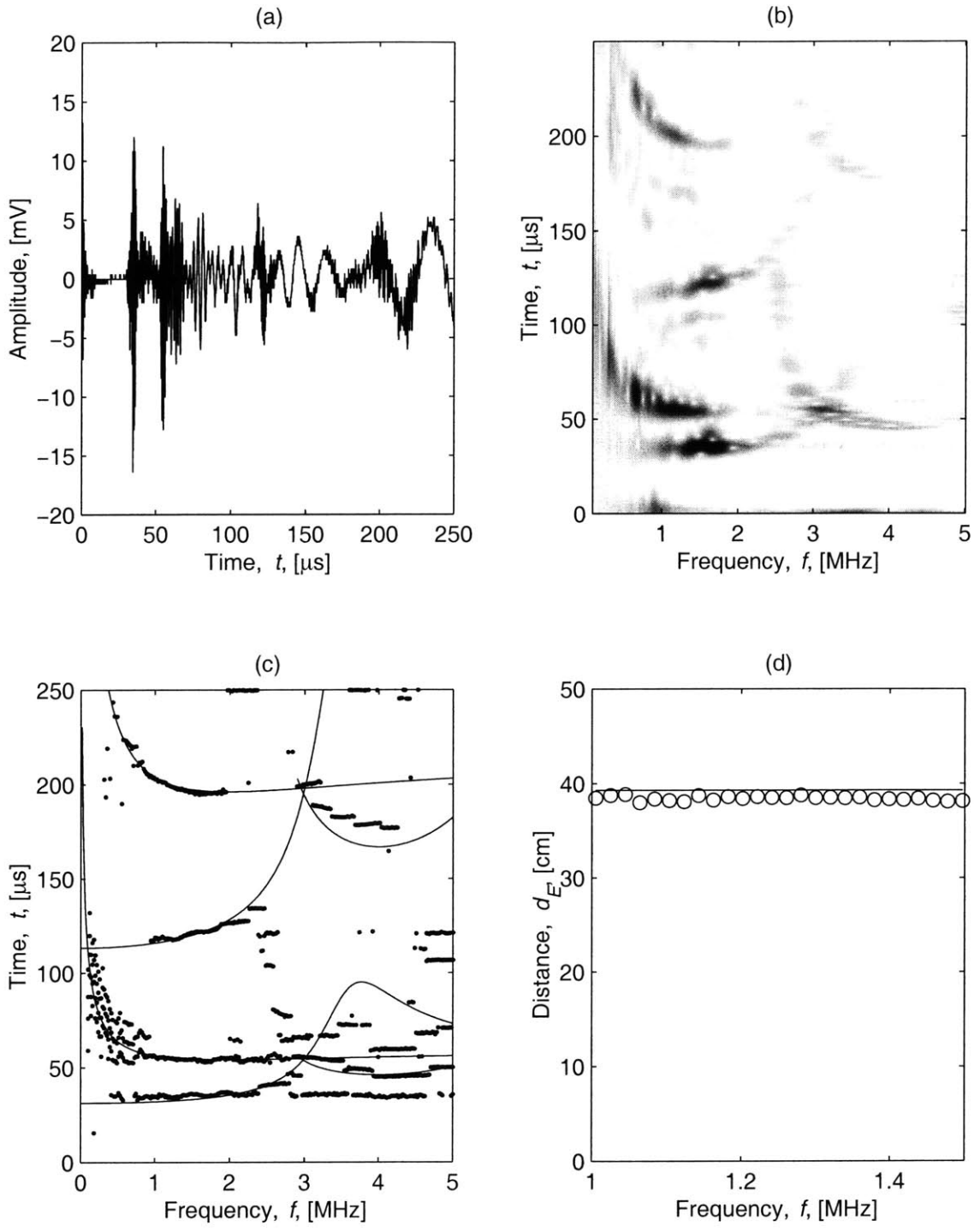

Figure 5-11: Experimental results for $d_L = 17$ cm.

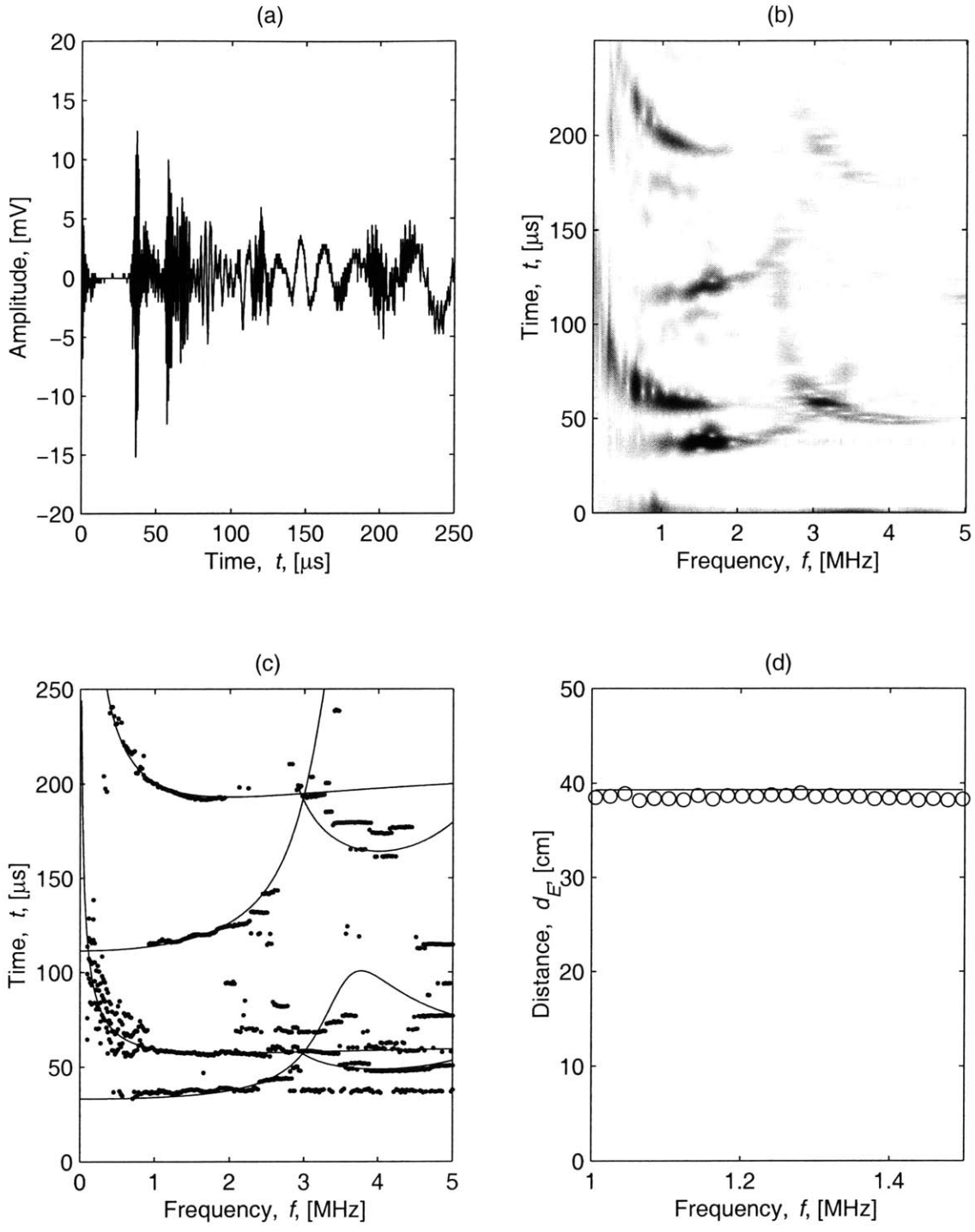

Figure 5-12: Experimental results for $d_L = 18$ cm.

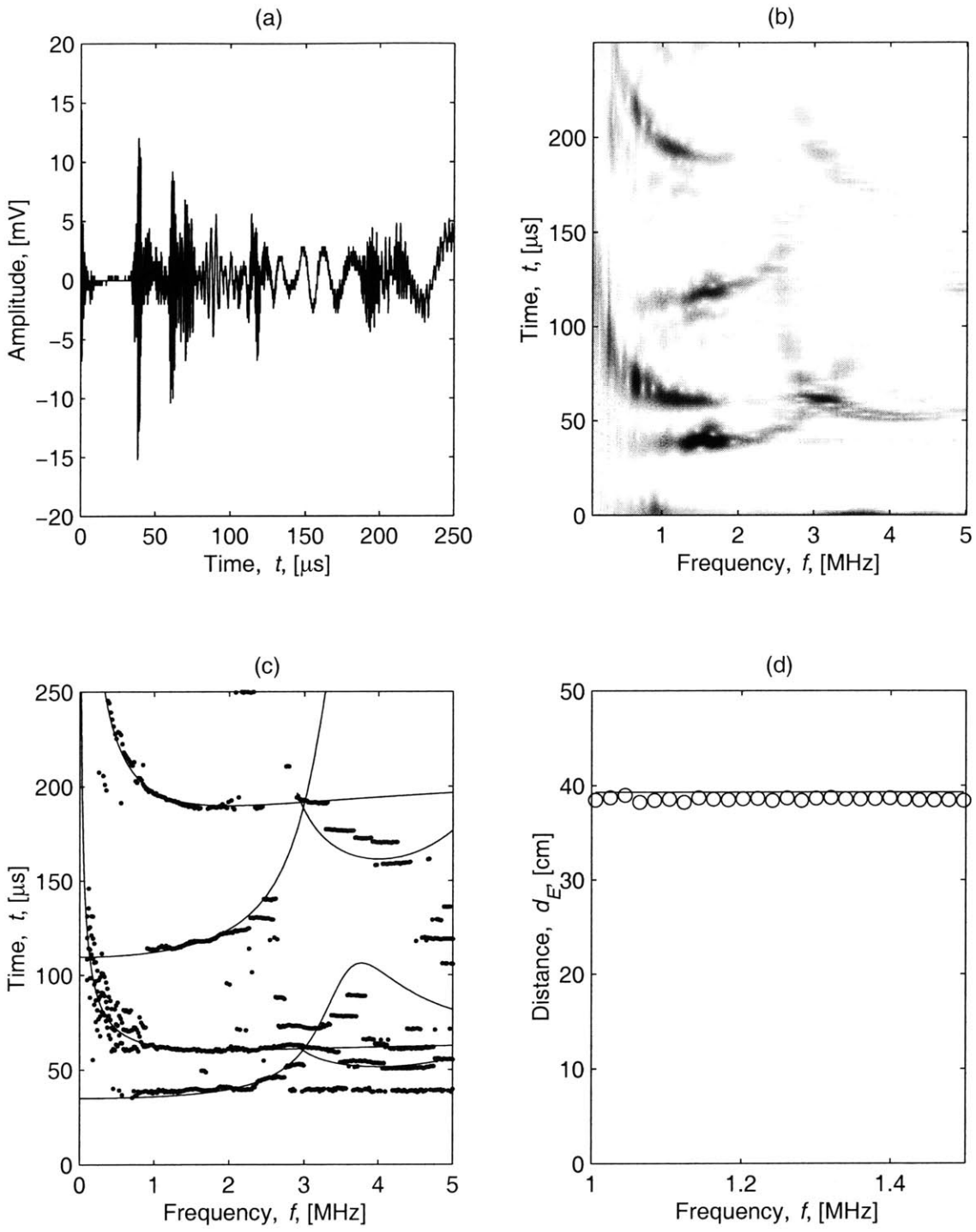

Figure 5-13: Experimental results for $d_L = 19$ cm.

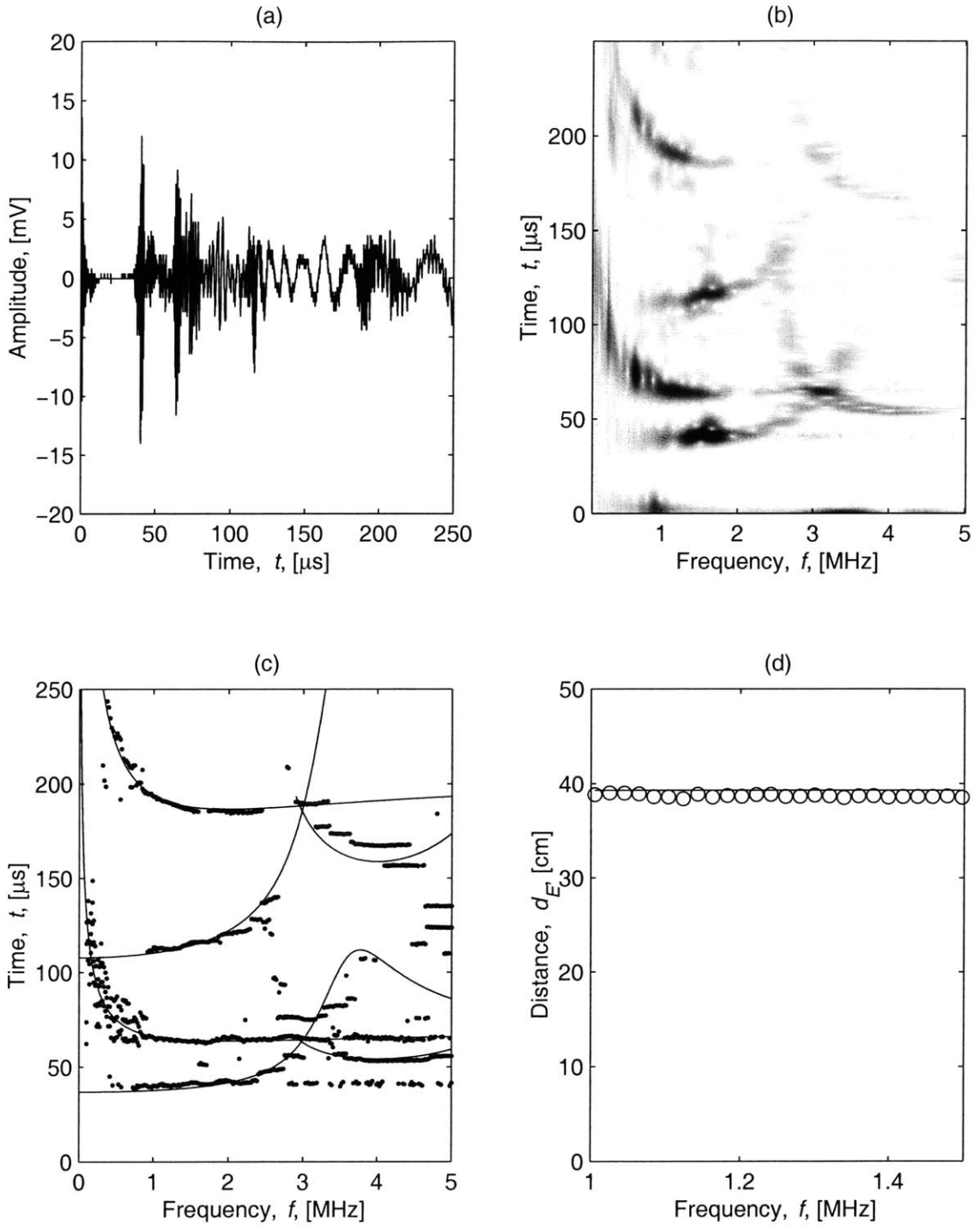

Figure 5-14: Experimental results for $d_L = 20$ cm.

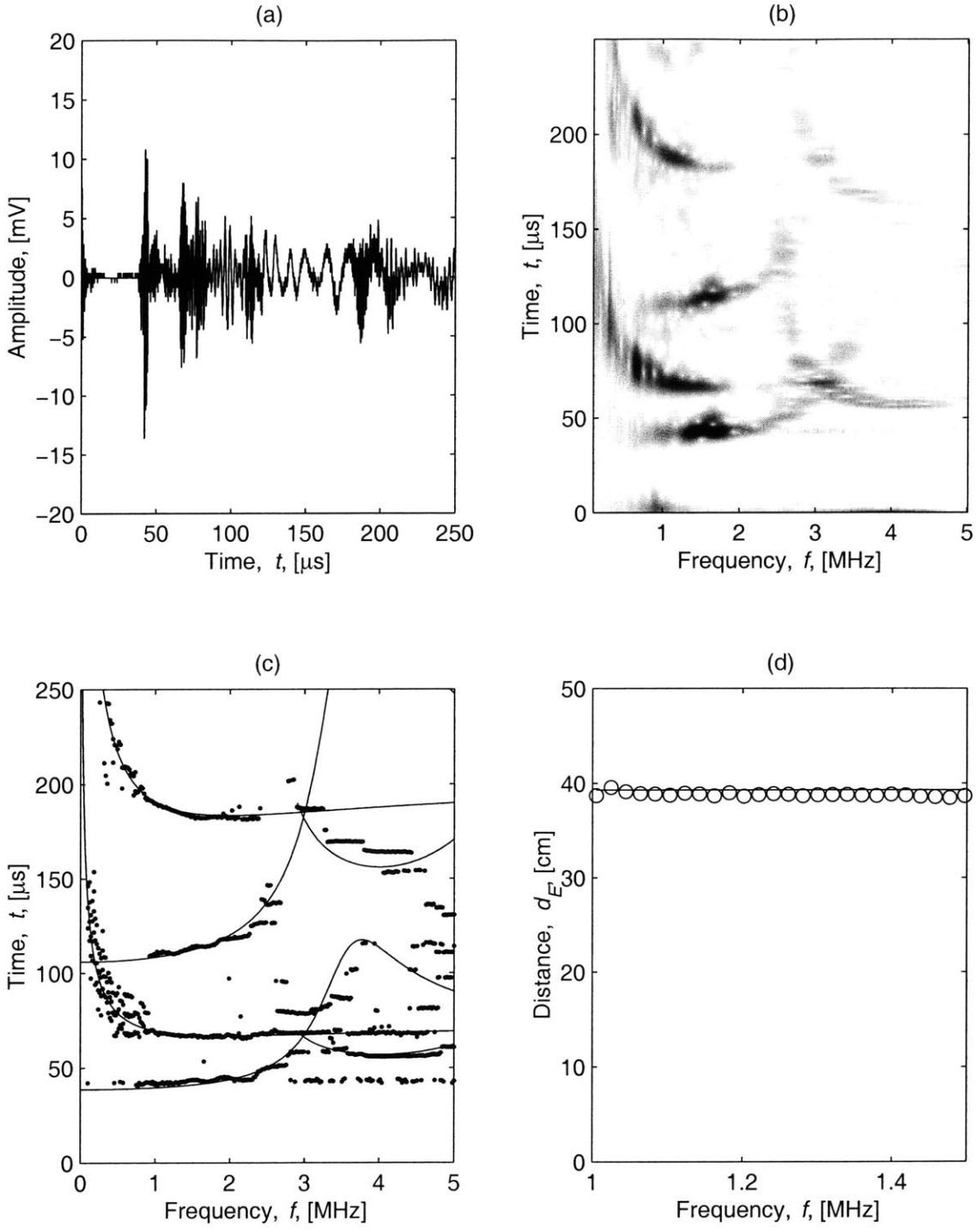

Figure 5-15: Experimental results for $d_L = 21$ cm.

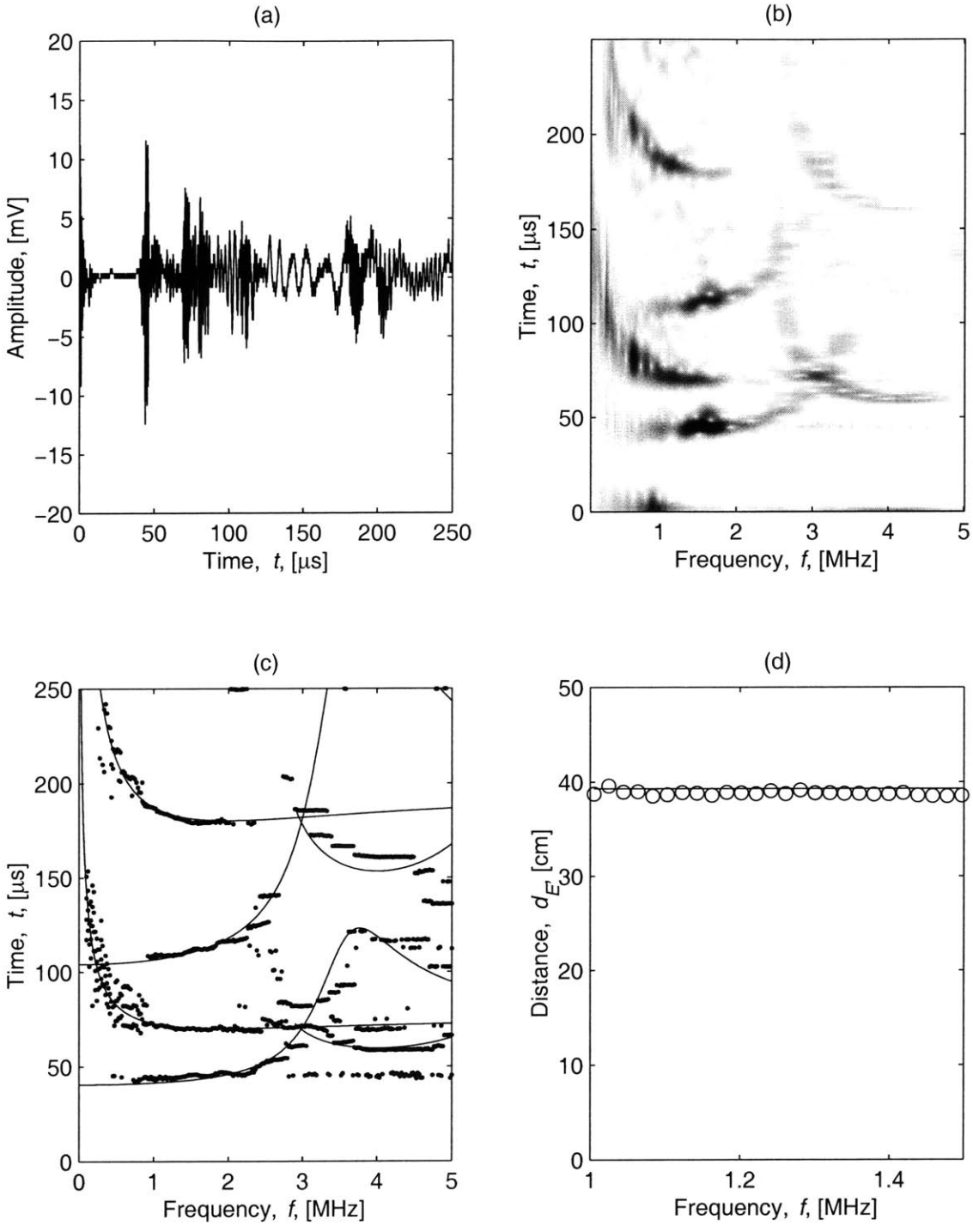

Figure 5-16: Experimental results for $d_L = 22$ cm.

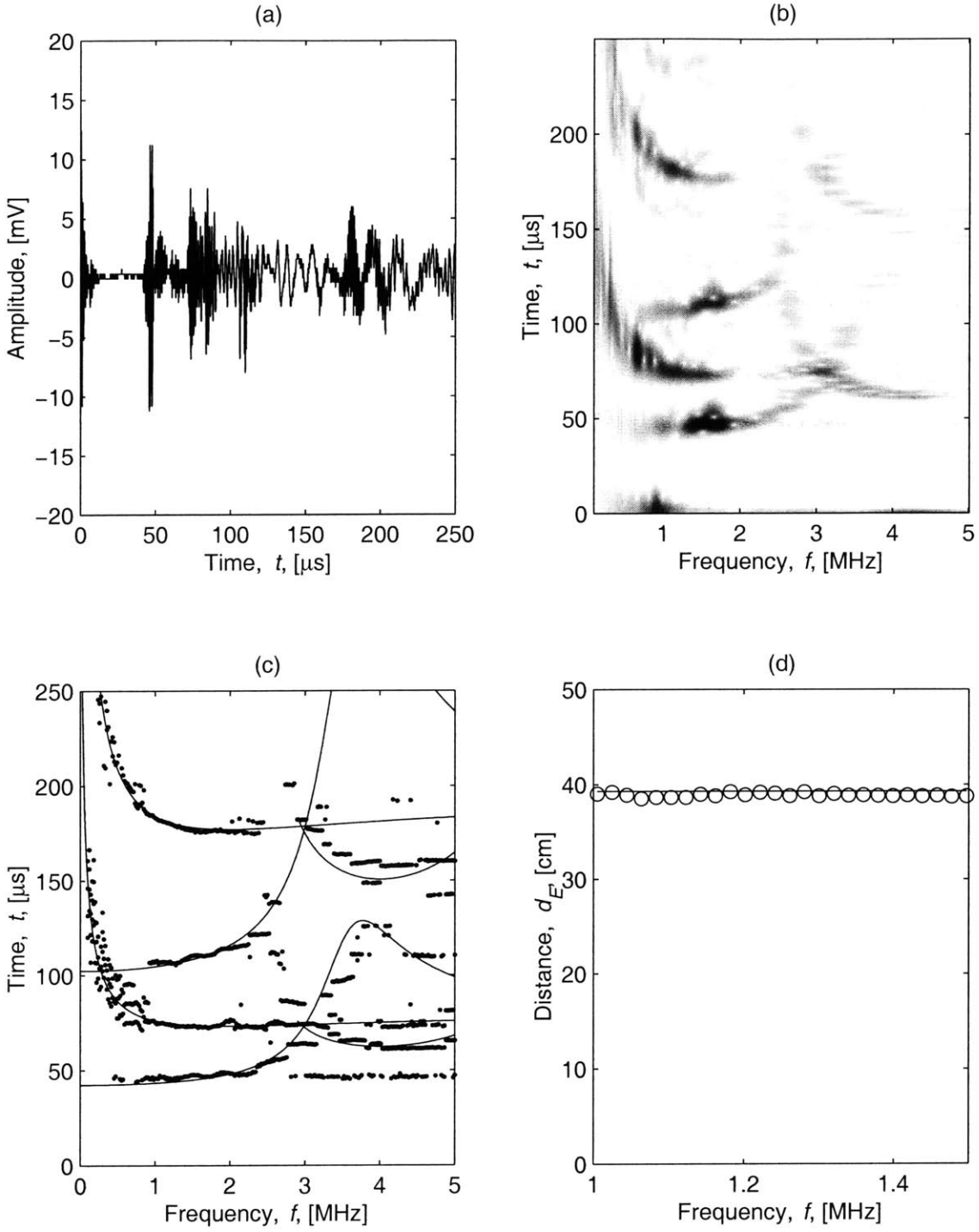

Figure 5-17: Experimental results for $d_L = 23$ cm.

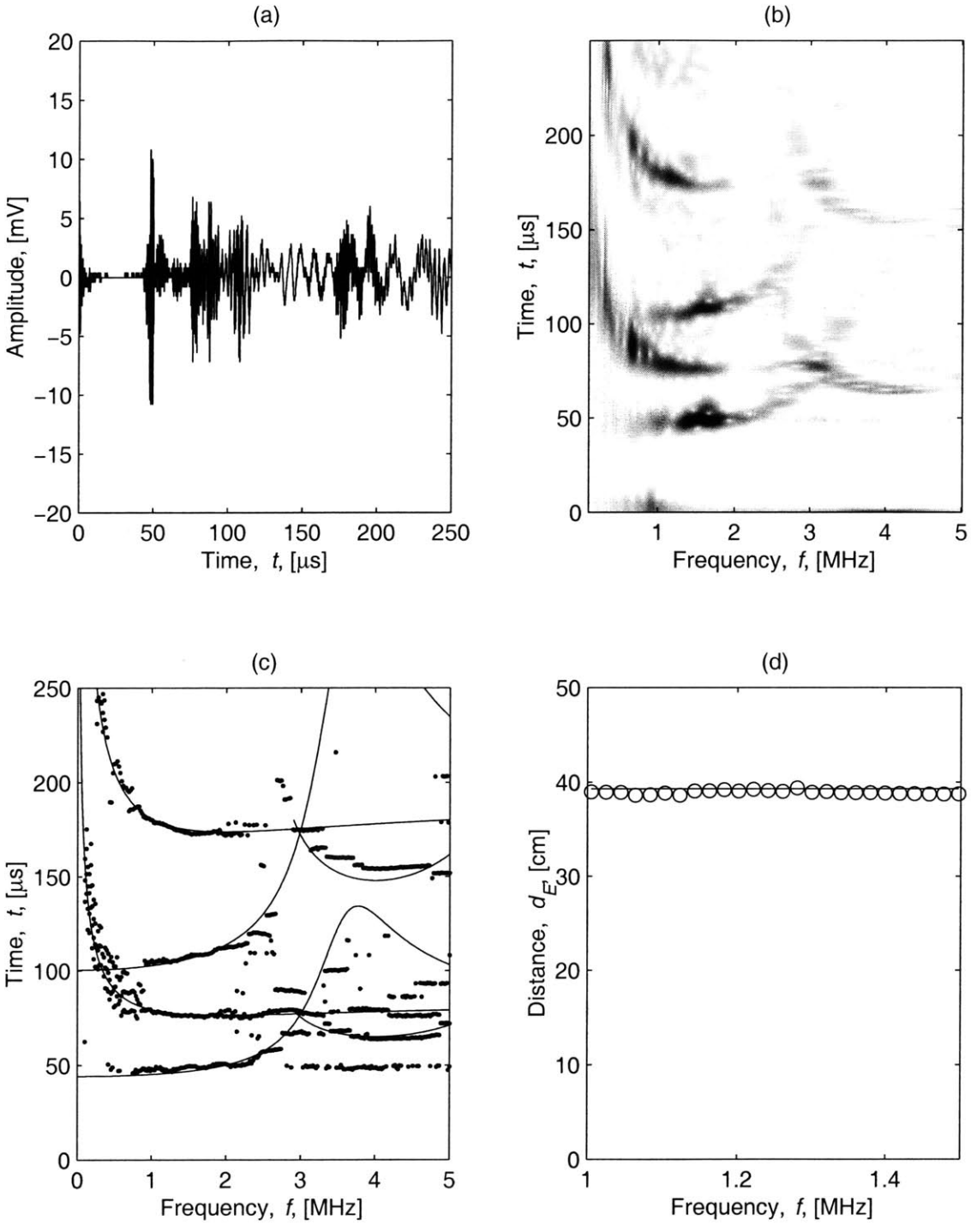

Figure 5-18: Experimental results for $d_L = 24$ cm.

Chapter 6

Conclusion

6.1 Summary

In this study, we sought to construct Rayleigh-Lamb wave dispersion curves from a single multimode, broadband signal using time-frequency analysis. The dispersion characteristics were measured using the Morlet wavelet transform, which yielded the group delay as a function of frequency. Both numerical and experimental investigations were performed.

In the numerical investigation, the method was applied to several simulated signals. Both single mode and two-mode signals were considered. The signals were created by arbitrarily defining dispersion characteristics, and then calculating the corresponding impulse response. The wavelet transform coefficients of each signal were then calculated from approximately zero to the Nyquist frequency. The group delays were then measured from the transform coefficients and compared with the known dispersion characteristics. The results were promising, but also indicated that the accuracy significantly depended on the chosen parameters of the Morlet wavelet.

In the experimental investigation, Lamb waves were measured using a pulsed Nd:YAG laser and PVDF transducers for generation and reception, respectively. The S_0, A_0 and A_1 modes of the direct arrivals as well as the reflections from the edge of the plate were observed from the wavelet transform coefficients of the signals. An analysis of the coefficients revealed that the A_0 and S_0 modes, particularly in the nondispersive regions, are dominant under the setup conditions. The group delay of these modes were therefore measured most accurately.

6.2 Conclusion

The greatest advantage of broadband excitation and detection of Lamb waves is the ease and speed with which the structure can be evaluated. The use of Lamb waves in itself has advantages over conventional methods (such as C-scanning) in terms of the time required to perform tests. The capability to excite, measure and analyze a wide range of frequencies at one time further increases that advantage.

Narrowband methods, in which a single mode at a narrow range of frequency is excited, provide greater ease and accuracy in the interpretation of the measured signals. However they are at times prohibitive in the level of accuracy and amount of effort required in the experimental setup. In this sense, broadband methods such as that explored in this study are more advantageous; the ease with which they may be implemented experimentally is surely something to be considered.

The greatest drawback of the method seems to be a lower level of accuracy as compared with narrowband methods. For highly accurate measurements of group or phase velocity, narrowband methods would still seem to be most attractive.

The level of computation required in the method might also be viewed as a weak point. Nevertheless, the savings in time spent for experimentation far outweighs the increase in computation, especially in this age of sky-rocketing computing power. Furthermore, the use of other wavelets for which a fast transform exists will also significantly decrease the amount of computation required.

In conclusion, we hold that the broadband generation and detection of Lamb waves, along with methods for time-frequency analysis of the signals are most suitable for situations requiring fast testing where a lower level of accuracy may be tolerated.

6.3 Future Work

Further work on this topic would most certainly involve the use of other wavelets. Types of wavelets exist which would significantly decrease the amount of computation required, making them more suitable for real time applications. There is also a great possibility that other wavelets would lead to more accurate group delay measurements.

This method also has yet to be applied to other specimens with different thicknesses and containing other types of defects. In this work only the detection of plate edges was

explored, and other defects such as notches and cracks should also be considered.

Appendix A

Equipment Specifications

A.1 PVDF Transducers

A.1.1 PVDF Film

The polyvinylidene fluoride (PVDF) or piezo film used in the experiments is 122 μm thick. It has silver ink metallization, which is best when mechanical stress is applied to the film [41].

A.1.2 Transducer Assembly

The PVDF film was cut into strips 37 mm long and 14 mm wide. To make sure the electrodes are not shorted, a ferric chloride etchant solution was applied to the sides of the transducer. A strip of Ni-clad copper flat ribbon[1] is attached to both sides of the piezo film using silver filled epoxy. A copper electrode is used to connect the other 2 ends of the flat ribbon to a BNC cable. The PVDF film and electrodes are then placed betweem two sheets of glass scrim cloth, and the assembly is laminated using clear epoxy.

A.2 Nd:YAG Laser

The laser used to generate ultrasound is a Q-switched, pulsed, Nd:YAG laser. Its characteristics are summarized in Table (A.1)

[1]From Measurements Group, Inc. P.O. Box 27777, Rayleigh, NC 27611

Wavelength	1064	nm
Pulse Width	$6-8$	ns
Energy	>90	mJ
Beam Diameter	3.75	mm
Beam Divergence	<4	mrad

Table A.1: Specifications of the Nd:YAG laser.

A.3 Focusing Lens

The laser beam was focused using a plano-convex lens which has one flat and one curved surface as shown in Fig. A-1. Its specifications are summarized in Table (A.2).

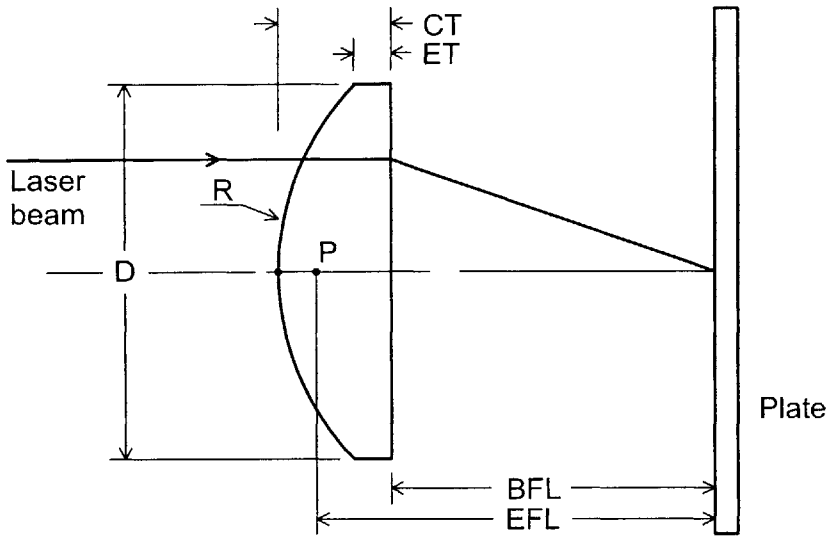

Figure A-1: Optical apparatus.

Property	Symbol	Value (mm)
Diameter	D	50
Effective focal length	EFL	100
Back focal length	BFL	93.41
Center thickness	CT	10
Edge thickness	ET	3.55
Radius of curvature	R	51.68

Table A.2: Dimensions and properties of the focusing lens.

Bibliography

[1] R.S.C. Monkhouse, P.D. Wilcox, and P. Cawley. Flexible interdigital PVDF transducers for the generation of Lamb waves in structures. *Ultrasonics*, 35(7):489–498, Nov. 1997.

[2] D.N. Alleyne and P. Cawley. Optimization of Lamb wave inspection techniques. *NDT & E International*, 25(1):11–22, 1992.

[3] A. Abbate, J. Frankel, and P. Das. Wavelet transform signal processing for dispersion analysis of ultrasonic signals. In *Proceedings - IEEE Ultrasonics Symposium*, pages 751–755, New York, 1995.

[4] K.L. Veroy, S.C. Wooh, and Y. Shi. Analysis of dispersive waves using the wavelet transform. In D.O. Thompson and D.E. Chimenti, editors, *Review of Progress in Quantitative Nondestructive Evaluation*, pages 687–694, New York, NY, 1999. Plenum Press.

[5] K.L. Veroy and S.C. Wooh. Time-frequency analysis of broadband dispersive waves using the wavelet transform. Review of Progress in Quantitative Nondestructive Evaluation (in press).

[6] A. Abbate, J. Koay, J. Frankel, S.C. Schroeder, and Das P. Application of wavelet transform signal processor to ultrasound. In *Proceedings - IEEE Ultrasonics Symposium*, pages 1147–1152, New York, 1994.

[7] H. Inoue, K. Kishimoto, and T. Shibuya. Experimental wavelet analysis of flexural waves in beams. *Experimental Mechanics*, 36(3), Sep. 1996.

[8] K.F. Graff. *Wave Motion in Elastic Solids*. Dover Publications, Inc., New York, 1975.

[9] R.D. Mindlin. Waves and vibrations in isotropic, elastic plates. *Structural Mechanics*, pages 199–232, 1960.

[10] I.A. Viktorov. *Rayleigh and Lamb waves: physical theory and applications.* Plenum Press, New York, 1967. Translation of *Fizicheskie osnovy primeneniia ul'trazvukovykh voln Releia i Lemba v tekhnike.*

[11] Y. Bar-Cohen, A.K. Mal, and Chang Z. Composite material defect characterization using leaky Lamb wave dispersion data. In *Proceedings of the SPIE - The International Society for Optical Engineering*, volume 3396, pages 180–6. SPIE, 1998.

[12] Y. Bar-Cohen, Shyh-Shiuh Lih, and A. Mal. Rapid characterization of the degradation of composites using plate waves dispersion data. In D.O. Thompson and D.E. Chimenti, editors, *Review of Progress in Quantitative Nondestructive Evaluation*, volume 2, pages 1171–6. Plenum, 1998.

[13] P.C. Xu, A.K. Mal, and Y. Bar-Cohen. Inversion of leaky Lamb wave data to determine cohesive properties of bonds. *International Journal of Engineering Science*, 28(4):331–46, 1990.

[14] A.K. Mal, P.C. Xu, and Bar-Cohen Y. Analysis of leaky Lamb waves in bonded plates. *International Journal of Engineering Science*, 27(7):779–91, 1989.

[15] A.K. Mal, P.C. Xu, and Bar-Cohen Y. Leaky Lamb waves for the ultrasonic nondestructive evaluation of adhesive bonds. *Journal of Engineering Materials and Technology-Transactions of the ASME*, 112(3):255–9, Jul. 1990.

[16] D.E. Chimenti and Y. Bar-Cohen. Signal analysis of leaky Lamb wave spectra for nde of composites. In McAvoy B.R., editor, *Ultrasonics Symposium Proceedings*, volume 2, pages 1028–31. IEEE, 1985.

[17] D.E. Chimenti and R.W. Martin. Nondestructive evaluation of composite laminates by leaky Lamb waves. *Ultrasonics*, 29(1):13–21, Jan. 1991.

[18] A. Safaeinili, O.I. Lobkis, and D.E. Chimenti. Quantitative materials characterization using air-coupled leaky Lamb waves. *Ultrasonics*, 34(2-5):393–6, Jun. 1996.

[19] N. Guo and P. Cawley. The interaction of Lamb waves with delaminations in composite laminates. *Journal of the Acoustical Society of America*, 94(4):2240–2246, Oct. 1993.

[20] N. Guo and P. Cawley. Lamb wave reflection for the quick nondestructive evaluation of large composite laminates. *Materials Evaluation*, 52(3):404–11, Mar. 1994.

[21] P. Cawley. The rapid non-destructive inspection of large composite structures. *Composites*, 25(5):351–7, May 1994.

[22] M. Castaings and P. Cawley. The generation, propagation, and detection of Lamb waves in plates using air-coupled ultrasonic transducers. *Journal of the Acoustical Society of America*, 100(5):3070–77, Nov. 1996.

[23] W.P. Rogers. Elastic property measurement using Rayleigh-Lamb waves. *Research in Nondestructive Evaluation*, 6(4):185–208, 1995.

[24] D.N. Alleyne and P. Cawley. The interaction of Lamb waves with defects. *IEEE Transactions on Ultrasonics, Ferroelectrics, and Frequency Control*, 39(3):381–397, May 1992.

[25] P. Cawley and D. Alleyne. The use of Lamb waves for the long range inspection of large structures. *Ultrasonics*, 34(2-5):287–90, Jun. 1996.

[26] F.A. Firestone and D.S. Ling. Method and means for generating and utilizing vibrational waves in plates. Patent 2,536,128, United States Patent Office, 1951.

[27] J.L. Rose, S.P. Pelts, and M.J. Quarry. A comb transducer model for guided wave NDE. *Ultrasonics*, 36(1-5):163–9, Feb. 1998.

[28] J.L. Rose. An ultrasonic comb transducer for smart materials. In *Proceedings of the SPIE - The International Society for Optical Engineering*, volume 3321, pages 636–43, 1998.

[29] S.C. Wooh and Y. Shi. Dynamic tuning of Lamb waves using array transducers. Review of Progress in Quantitative Nondestructive Evaluation (in press).

[30] S.C. Wooh and Y. Shi. Synthetic phase tuning of guided waves. Submitted for review to IEEE UFFC.

[31] S.G. Pierce, B. Culshaw, W.R. Philp, F. Lecuyer, and R. Farlow. Broadband Lamb wave measurements in aluminium and carbon/glass fibre reinforced composite materials using non-contacting laser generation and detection. *Ultrasonics*, 35(2):105–14, Mar. 1997.

[32] D. Alleyne and P. Cawley. A two-dimensional Fourier transform method for the measurement of propagating multimode signals. *Journal of the Acoustical Society of America*, 89(3):1159–68, Mar. 1991.

[33] A.V. Oppenheim and R.W. Schafer. *Discrete-Time Signal Processing.* Prentice Hall, Englewood Cliffs, N.J., 1989.

[34] S. Chandrasekhar. *Hydrodynamic and Hydromagnetic Stability*, chapter 1. Oxford University Press, 1961.

[35] W.H. Press, S.A. Teukolsky, W.T. Vetterling, and B.P. Flannery. *Numerical Recipes in C.* Cambridge University Press, 2nd edition, 1992.

[36] R.T. Ogden. *Essential wavelets for statistical applications and data analysis.* Birkhauser, Boston, 1997.

[37] C.K. Chui. *An introduction to wavelets*, volume 1 of *Wavelet analysis and its applications.* Academic Press, Boston, 1992.

[38] A. Cohen and R.D. Ryan. *Wavelets and Multiscale Signal Processing.* Chapman and Hall, London, 1995.

[39] G. Strang and T. Nguyen. *Wavelets and Filter Banks.* Wellesley-Cambridge Press, 1997.

[40] M. Misiti, Y. Misiti, G. Oppenheim, and J.M. Poggi. *Wavelet Toolbox: For Use with MATLAB.* The MathWorks, Inc., Natick, MA, 1996-1997.

[41] Measurement Specialties, Inc., Valley Forge, PA. *Piezo Film Sensors Technical Manual.*

[42] J.D. Achenbach. *Wave propagation in elastic solids.* North-Holland Pub. Co., Amsterdam, 1975.

[43] C.C. Mei. *Mathematical Analysis in Engineering: How to Use the Basic Tools.* Cambridge University Press, 1997.

[44] A.M. Aindow, R.J. Dewhurst, D.A. Hutchins, and S.B. Palmer. Laser-generated ultrasonic pulses at free metal surfaces. *Journal of the Acoustical Society of America*, 69(2):449–455, Feb. 1981.

[45] D.A. Hutchins, R.J. Dewhurst, and S.B. Palmer. Laser generated ultrasound at modified metal surfaces. *Ultrasonics*, 19(3):103–108, May 1981.

[46] Edmund Scientific Company (Industrial Optics Division), Barrington, NJ. *1998 Optics and Optical Instruments Catalog.*

[47] M.B. Klein and G.D. Bacher. High-sensitivity laser-based detection of Lamb waves using photo-emf sensors. In *Proceedings of ASNT Spring Meeting*, Mar. 1998.

[48] New Wave Research Inc., Sunnyvale, CA. *MiniLaser Nd:YAG Laser Operating Manual*, August 1997.

[49] K. Kishimoto. Wavelet analysis of dispersive stress waves. *JSME International Journal - Series A*, 38(4):416–423, 1995.

[50] M. Nishimoto and H. Ikuno. Time-frequency analysis of scattering data using the wavelet transform. *IEICE Transactions on Electronics*, E80-C(11):1440–7, Nov. 1997.

[51] T. Onsay and A.G. Haddow. Wavelet transform analysis of transient wave propagation. *Journal of the Acoustical Society of America*, 95(3):1441–1449, Mar. 1994.

2976-99